Università degli studi di Padova

DIPARTIMENTO DI FISICA E ASTRONOMIA "GALILEO GALILEI"
Corso di Laurea Magistrale in Fisica

REVIEW OF BLM THRESHOLDS AT TERTIARY LHC COLLIMATORS

Supervisor:
Prof. **Marco Zanetti**

Candidate:
Marco D'Andrea
Matricola 1127722

External supervisor:
Dr. **Alessio Mereghetti**

Anno Accademico 2016-2017

Abstract

The Large Hadron Collider is designed to accelerate protons at the unprecedented energy of 7 TeV. With a total stored energy of 360 MJ, even tiny losses can cause machine downtime or induce damage to sensitive accelerator components. The Beam Loss Monitors (BLMs) are an important component of the complex LHC protection system. They consist of a series of ionisation chambers located all around the ring to detect secondary particle showers induced by beam losses. The monitors are assigned thresholds such that if the radiation generated by the loss is too high, the BLM triggers a beam dump, preventing the loss to grow excessively. BLM signals are recorded for different integration windows, in order to detect losses on very different time scales, ranging from the extremely short ones (taking place over half a turn) to those very close to steady state (i.e. lasting for more than a minute).
The LHC is equipped with a complex collimation system, to provide the machine with passive protection in case of transient losses. Among the different families populating the system, the tertiary collimators (TCTs) are located close to the experiments to protect the magnets needed to squeeze the colliding beams. These collimators are made of tungsten to maximise absorption capabilities at the expenses of robustness, while minimising the background to detectors. Collimator BLMs have thresholds aimed at preventing damage to the jaws. The thresholds have been first set based on simulations and empirical scaling laws, and then optimized based on operational experience as a trade-off between the required protection of the metallic collimators and the rate of spurious beam abort triggers.
This work reviews and proposes further optimisation of the current thresholds of the BLMs at the TCTs. The review is accomplished by means of numerical simulations, where a single TCT collimator is set as aperture bottleneck and the losses concentrate there. Two steps are carried out; in the first one, the population of protons hitting the collimator is evaluated by means of cleaning simulations, where single-particle beam dynamics and particle-matter interactions are taken into account to accurately describe multi-turn effects. The second step consists of the actual energy deposition calculations carried out by means of a Monte Carlo transport code, for the evaluation of the peak energy deposition in the collimator jaw and the corresponding BLM signal. Thanks to these two quantities, and knowing the maximum energy deposition that a TCT can stand before experiencing damage in different time domains, it is then possible to compute the BLM thresholds on the different integration windows. After choosing the collimator to be used for the study, preliminary simulations are setup in order to identify the worst case scenario in terms of ratio of the BLM signal over the peak energy deposition in the jaws. The configuration found in this step is then used to simulated the BLM response for different beam energies and review the BLM thresholds.
The work is complemented by a benchmark of the simulation results against measurements gathered in 2016 and 2017. This allows to verify experimentally the BLM response per hitting proton, for a couple of scenarios of controlled losses on different collimators.

Contents

Chapter 1

Introduction

The Large Hadron Collider (LHC) [1] is designed to accelerate and collide two counter-rotating beams of $3.2 \cdot 10^{14}$ protons at a kinetic energy of up to 7 TeV. In order to guide and focus the beams with such a high kinetic energy, superconducting magnets are deployed.
Each proton beam of the LHC stores total energy of up to 360 MJ. A proper handling of this huge amount of energy is crucial, since the superconducting magnets would quench (i.e. they would lose their superconducting properties) after an energy deposition of 5 mW/cm^3 and a 0.001% of the stored energy can damage metal if deposited instantaneously. Therefore, the LHC needs a sophisticated system of collimators to provide beam cleaning and passive machine protection.
The LHC collimation system consists of a total of 110 collimators, which are set to different openings to implement a multi-stage cleaning and protection system in all operational phases and for all beam energies. Two insertions in the ring are dedicated to momentum and betatron cleaning, while the other collimators protect the most sensitive components of the machine (injection, extraction and interaction regions). While most of the collimators have jaws made of graphite (hence optimised for robustness), some collimators have metallic jaws to enhance absorption capability at the expenses of robustness.
The LHC is also equipped with a monitoring system, to detect the onset of losses. Its main component is ionisation chambers, referred to as *Beam Loss Monitors* (BLMs), placed all around the ring to detect secondary particles originated by beam losses. Based on the estimated energy deposition it is then possible to trigger a beam dump (i.e. the extraction of the beams from the accelerator and their final disposal on an absorbing block) if these losses turn out to be too high in a certain time window and avoid machine downtime or critical damage to devices.
Collimators themselves can be damaged and BLMs are installed in their proximity in order to monitor beam losses on the jaws. In particular, the TCT collimators, which protect the superconductive magnets placed close to the interaction points where the experiments are located, are one of the most sensitive families to energy deposition. To maximise absorption capabilities, they are equipped with metallic jaws made of a tungsten alloy. This means that a large amount of energy is deposited on these devices and therefore they are particularly delicate and the corresponding BLMs must be equipped with carefully set thresholds. The BLM thresholds must be neither too low, not to cause spurious beam dumps and unnecessary machine downtime, nor too high, allowing critical energy deposition on the collimator jaws. Therefore, when setting BLM thresholds, it is essential to find an optimum trade off between the required protection of the metallic collimators and the rate of spurious beam abort triggers, based on operational experience. In the past, simulations and measurements estimating the signal in the BLMs due to impacts on the collimators were used to set

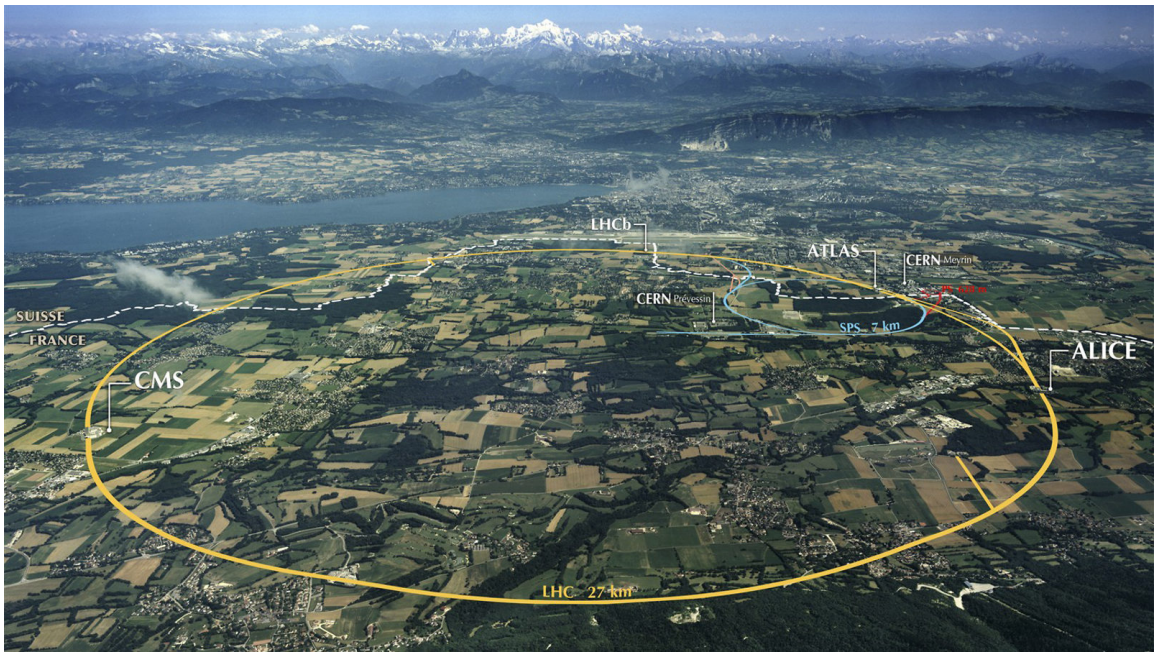

Figure 1.1: Air view of the LHC area. The CERN sites and the main experiments are also shown.

BLM thresholds [2]. Over the years, many corrections were applied based on operational experience [3].
The aim of this work is to review the BLM thresholds at collimators for different beam kinetic energies that range from injection energy (450 GeV) to the expected working point of LHC (7 TeV). Priority was given to TCT collimators, as these are the most sensitive to damage caused by beam losses because of their metallic jaws. The work is carried out by means of simulating the interaction of the beam particles with the collimator jaws with codes such as SixTrack and FLUKA. The simulated scenario, chosen after some preliminary studies, is the direct impact of beam tails on the collimator jaws in case of a constant drift of the beam towards one of the jaws of the vertical collimator placed in IR2. This is taken as most conservative scenario, as it concentrates the energy deposition on a very small volume of jaw material. In order to gain confidence on results, a couple of scenarios of primary beam losses on TCTs have been measured, and used to benchmark simulation results.
The simulations of the BLM response allow to correlate the signal by the monitors per lost proton with the corresponding energy deposition on the collimator jaw. Knowing the energy deposition that can cause damage to the device, it is then possible to extrapolate the corresponding BLM signal, to be considered as new threshold. The actual thresholds are calculated for different integration times (i.e. time windows) in order to take into account different kind of losses (fast or continuous losses), as described in sec. 1.4. The response of a collimator BLM is sensitive to impact conditions, jaw material and the jaw-BLM relative positions [4]; in particular, each BLM is installed in a different position with respect to the corresponding collimator. For this reason, it was decided to focus on the analysis on the collimator with the most concentrated energy deposition and the corresponding BLM in the least favorable position; hence, results can be applied to all TCTs in a conservative was. The comparison of the simulation results with the direct measurements is complementary to this analysis; in fact, the benchmarks takes into account in more details the actual loss-collimator-BLM configuration.

The following sections give an overview of the LHC layout as well as the main components of the machine (e.g. superconducting magnets, cleaning insertions and collimation system), with particular focus on the structure of the collimators and BLMs. The logic behind the BLM thresholds is also briefly explained.

1.1 The LHC

1.1.1 The layout

The LHC is a circular accelerator with a 26.659 km circumference crossing the border between Switzerland and France at an average depth of 100 m underground. More in details, it is a synchrotron and a collider, where two counter-rotating beams (Beam 1 clockwise and Beam 2 counter-clockwise) are accelerated and collided.
The core layout of the LHC, shown in fig. 1.2, is composed of eight arcs, which house the equipment to bend the trajectory of the beams, and eight *Long Straight Sections* (LSSs), where devices with dedicated tasks are installed, also called *Insertion Regions* (IRs). Beam 1 and Beam 2 are injected in IR2 and IR8 respectively and are accelerated up to nominal energy by the RF cavities located in IR4. They are then brought into collisions at the four *Interaction Points* (IPs), which house the main experiments:

- ATLAS (IP1) and CMS (IP5), multi-purpose detectors dedicated to investigation of the broadest range of Physics possible;
- LHCb (IP8), a specialized detector with the main aim of explaining the asymmetry between matter and antimatter in the universe by studying the Physics of the beauty quark;
- ALICE (IP2), a specialized detector dedicated to the studies of the quark-gluon plasma generated by lead-ion collisions.

Three further experiments (TOTEM, LHCf and AFP) are installed upstream and downstream of IP5 and IP1 respectively and have been devised to detect particles coming out from the other experiments with small deviation angles in order to measure the elastic scattering cross section. Finally, IR6 houses the beam dump system.

1.1.2 The LHC machine cycle

The operation of the LHC follows a well-established stages, which together form a machine cycle. A typical LHC machine cycle for 2017 is shown in fig. 1.3. At the injection stage (1), the LHC receives two beams from the Super Proton Synchrotron (SPS) at an energy of 450 GeV per beam in bunch trains. When the filling procedure is completed, both beams are ramped up (2) until the energy reaches the current flat top value, i.e. 6.5 TeV at the time of writing. During this phase, corrector magnets are used to shrink the beam size at the IPs to achieve the desired $\beta^\star$ (i.e. the β function at the IPs) and maximise the luminosity. The squeeze is completed after the flat top energy is reached (3). Up to this point, the beams are separated by several σ in all IPs. Hence, the final step is to collapse the separation orbit bumps and bring the beams into collisions. During the stable beams operational state (4) the experiments take data until the beams are extracted or dumped (5) due to operational requirements, equipment failures, beam instabilities or operator mistakes. When this happens, the machine is ramped down (6) to injection energy in preparation for the next fill [6].

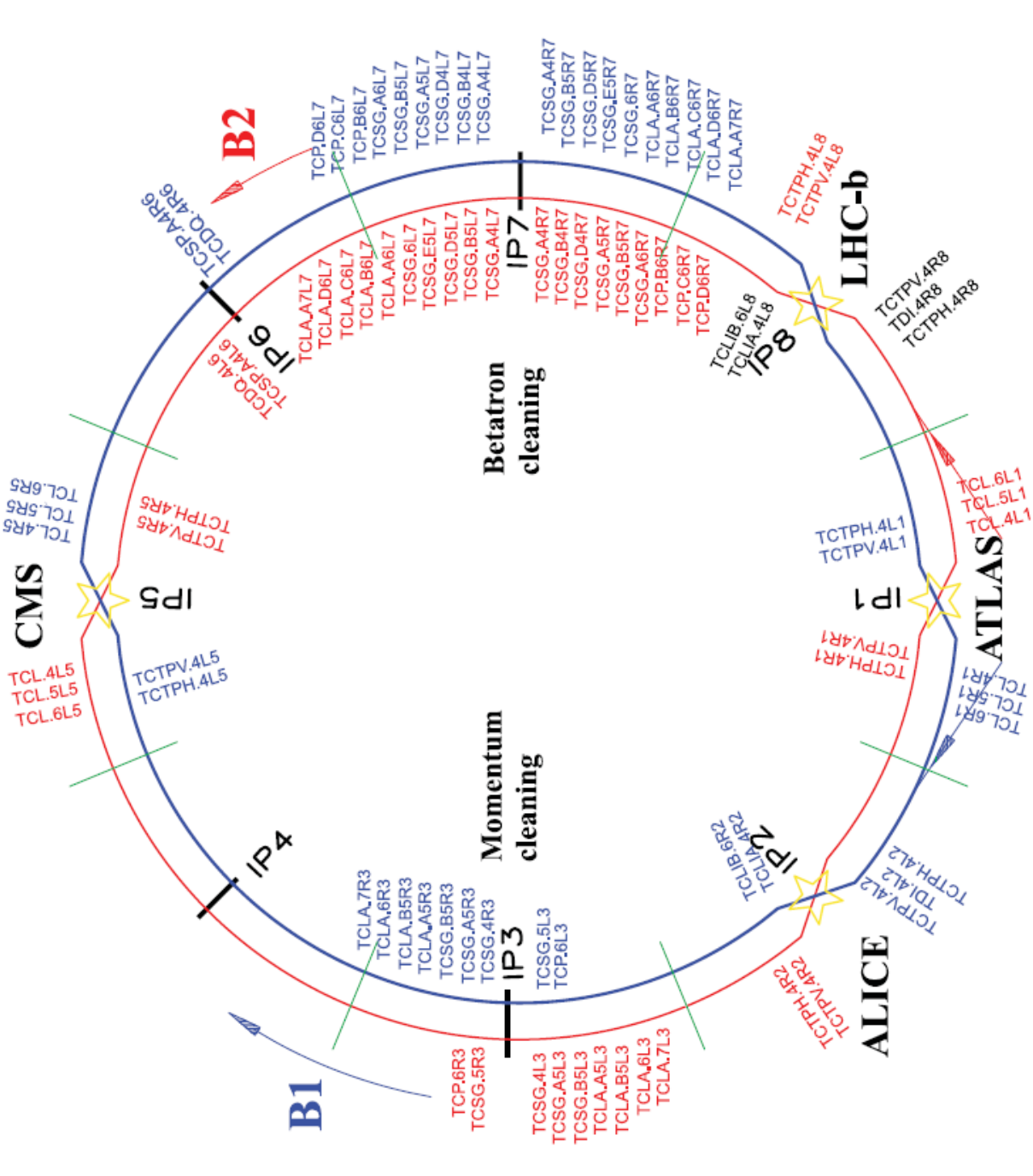

Figure 1.2: Schematic representation of the LHC layout [5], showing the collimator locations around the ring.

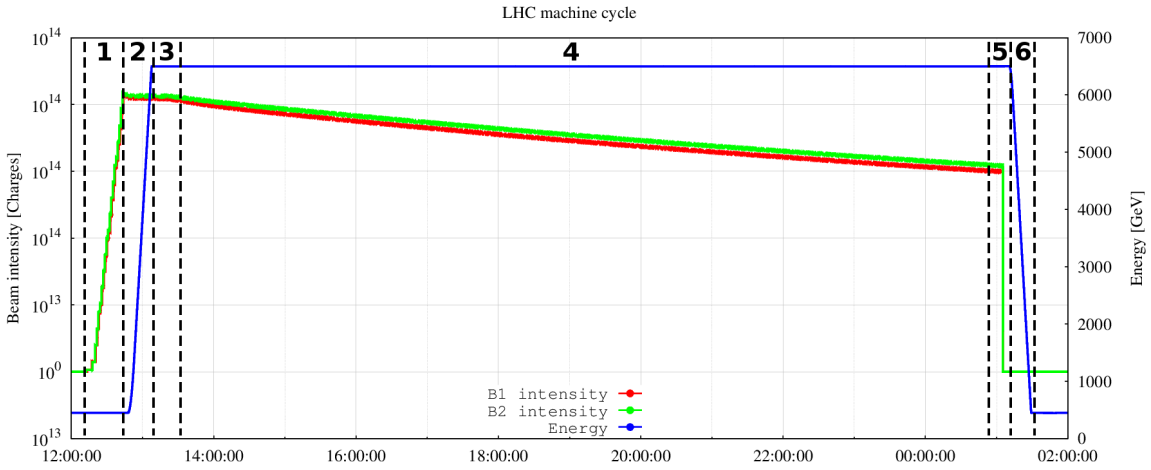

Figure 1.3: The LHC machine cycle, illustrated by the beam energy and beam intensities taken from fill 6175. There are six stages: 1) injection; 2) ramp and squeeze; 3) end of squeeze; 4) stable beams; 5) beam dump; 6) ramp down.

1.1.3 The superconducting magnets

Despite the large circumference, the extremely high top energy of the beams require dipole fields of 8.3 T in order to maintain a circular orbit. This value is much higher than the maximum magnetic field provided by warm dipoles (i.e. $\sim$ 2 T), therefore the arcs (and partially the LSSs) are equipped with superconducting magnets. Superconductivity [7] is a property presented by some materials when cooled to very low temperatures and enables the flow of currents with no dissipation by the Joule effect. It is then possible to let high current densities flow through wound conductors, obtaining high values of magnetic field. These magnets however are sensitive to heating from the beam or other sources and quench (i.e. lose their superconductivity) after an energy deposition of 5 mW cm^{-3} when run at the nominal field at 7 TeV. Quenches are also provoked by transient heating, in which case the required energy depends on the loss duration.

1.1.4 The cleaning insertions

As previously discussed, the stored energy of the beams is about 10 orders of magnitude above the quench limit of the superconducting magnets and even small losses can induce quenches. In a real situation such as that of the LHC, particles of the beam drift far from the core, generating a halo that will eventually be lost on the machine. This is the main reason why a cleaning system against beam-induced losses is needed in order to protect the magnets. Two insertion regions are dedicated to beam cleaning, namely momentum cleaning in IR3 and betatron cleaning in IR7. These are insertions without superconducting magnets, where several collimators are installed to intercept and absorb the beam halo particles before they are lost in the superconducting aperture of the machine. Primary collimators are installed in the dogleg, i.e. a section of the LSS where the beam separation changes. In this way, a large fraction of the secondary particles coming out of inelastic interactions are filtered out and the energy deposition is concentrated in region where there are no superconducting magnets but only room-temperature magnets, which are tolerant to energy deposition.

1.2 The LHC Collimation System

Fig. 1.2 shows the LHC layout and the positions of the collimators around the ring. Including the dump protection devices (e.g. TCDQs, Target Collimators Dump Quadrupole) and the injection protection devices (e.g. TDI, Beam Absorber for Injection), the system includes 110 [5] movable collimators installed in the LHC ring and its transfer lines.
Halo collimation is achieved by a multi-stage cleaning system (as described in sec. 2.2). Collimators are organised in families, based on their functional positions and settings. IR3 and IR7 host the insertions dedicated to momentum cleaning and betatron cleaning respectively. The primary collimators (TCPs, Target Collimators Primary) are the closest to the beam; hence, they represent the aperture bottleneck during regular operation. They intercept beam tails, and the particles scattered out are collected by the secondary collimators (TCSGs, Target Collimators Secondary Graphite); active absorbers (TCLAs, Target Collimator Long Absorber) are installed towards the end of the IRs, to catch secondary particle showers before entering the arcs. Two tertiary collimators (TCTPs, Target Collimators Tertiary with Pick-up) made of a tungsten alloy are installed upstream of the collision points for all experimental IRs, in order to provide local protection of the quadrupole triplets in the final focusing system and minimise the background to experiments. One of the collimators is in the horizontal plane (TCTPH) and the other one in the vertical plane (TCTPV). Downstream of the high-luminosity experiments (ATLAS and CMS) there are three more collimators (TCLs, Target Collimators Long) to intercept the collision debris and minimise the leakage of collision debris to the downstream arc. Additional collimators are installed in the injection and extraction regions in order to provide protection against failures (such as miskicked beams).
The LHC collimators (with the exception of the TCDQs) are composed of two movable jaws that are kept centred with respect to the centre of the beam envelope, such that a symmetric cut of the beam is achieved. The aperture of the jaws is adjusted according to the beam energy, machine optics and operational mode (e.g. squeeze or collision). A stepping motor per jaw corner (i.e. upstream or downstream) is used for aperture and angular adjustments, while a fifth one shifts transversely the whole collimator tank. The jaws are water-cooled through a heat exchanger formed by copper-nickel pipes. A clamping system enhances the thermal contact between the jaws and the heat exchanger. The jaws do not have the same length for all collimator types, but they are always composed of a flat part, which is the one actually in contact with the beam and determines the *active length* of the jaw, and a 10 cm tapering on both ends to avoid geometrical impedance effects. The two jaws of a collimator are kept in vacuum by a metallic tank, and the whole apparatus is mounted on dedicated supports all along the LHC tunnel. More details on the structure of the collimators can be found in [8].
Each collimator family has a dedicated jaw material, optimised for the functional scope of the family. Primary and secondary collimators, such as the one shown in fig. 1.4, have jaws made of fiber-reinforced graphite (CFC). This low-Z material limits the energy deposition in the jaws and makes the device extremely robust. Primary collimators have an active length of 60 cm as a compromise between cleaning efficiency and robustness, while secondary collimators have an active length of 1 m. The jaws of the tertiary collimators have an active length of 1 m and are made of copper with a tungsten inlay. This is a high-Z material in order to maximise the probability of absorption of the incoming particle. This makes them not as robust as the CFC collimators, which calls for particular attention when setting the BLM thresholds.

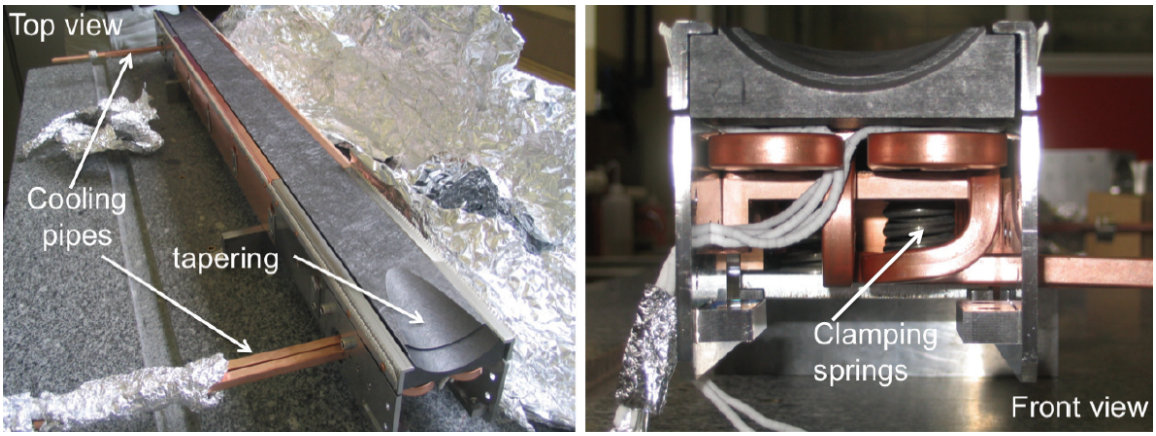

Figure 1.4: Top and front view of a secondary collimator jaw assembly [8].

Figure 1.5: The inside of an ionisation chamber. The stack of aluminium electrodes with the insulator ceramics at both ends can be seen [9].

1.3 The Beam Loss Monitors

The Beam Loss Monitoring System is composed of around 3600 monitors installed at likely or critical loss location. The standard monitors are ionisation chambers with parallel aluminium electrode plates separated by 0.5 cm (shown in fig. 1.5). The chambers are filled with N_2 at 100 mbar overpressure with respect to the atmosphere. The collection time of the electrons and ions is of the order of 300 ns and 80 μs respectively. At locations with very high potential loss rates, the ionisation chambers are complemented by secondary emission monitors, based on the same design but only holding three electrodes. This type of chamber is 10 cm long and the pressure inside has to stay below 10^{-7} bar. Both chambers operate at 1.5 kV and the combined dynamic range of the detectors is higher than 10^9. The lower limit for the ionisation chambers is given by leakage currents through the insulator ceramics, while the upper limit is due to space charge. More details can be found at [9].

1.4 BLM thresholds

The main purpose of the Beam Monitoring System is to trigger a beam abort when the measured losses exceed a certain threshold. The BLM detectors integrate the measured signals in 12 different time intervals (running from 40 μs to 83.9 s) enabling a different set of abort thresholds depending on the duration of the beam loss. Indeed, losses might occur over a broad range of time-scales, from a fraction of a single turn to tens of seconds. One could set a system that dumps the beam when a certain peak in the signal coming from a BLM is reached. However, this is useful only for short losses which cause high energy

deposition in a short time. Longer, continuous losses may never go over the chosen peak, but the damage caused by them may add up over time and result in critical failures. The signal coming from the BLM must be integrated over different time periods (called *running sums* and reported in tab. 1.1) in order to take into account the widest possible range of time scales of losses.

Signal name	**Time windows**		**Refreshing rate**	
	Number of 40 μs steps	Duration [ms]	Number of 40 μs steps	Duration [ms]
RS01	1	0.04	1	0.04
RS02	2	0.08	1	0.04
RS03	8	0.32	1	0.04
RS04	16	0.64	1	0.04
RS05	64	2.56	2	0.08
RS06	256	10.24	2	0.08
RS07	2048	81.92	64	2.56
RS08	16384	655.36	64	2.56
RS09	32768	1310.72	2048	81.92
RS10	131072	5242.88	2048	81.92
RS11	524288	20971.52	16384	655.36
RS12	2097152	83886.08	16384	655.36

Table 1.1: Running sums time windows and refresh rates [10].

32 energy levels running from 0 to over 7 TeV account for the change in energy deposition in the device and in the BLM per impacting proton as a function of beam kinetic energy. Thus, a table of thresholds gathering values per running sum as a function of beam energy must be provided to each monitor. Each BLM in a family is assigned *applied thresholds*, derived from pre-set *master thresholds* by multiplication with a *monitor factor*. Monitors which protect the same elements with same detector locations from similar scenarios are grouped into *families* that share the same master thresholds.
BLM thresholds are highly critical for the safety of the machine and depend to a large part on human judgement. In fact, not all the BLMs can be simulated in details; hence, it is crucial to model the losses and the physics of the involved processes with sound assumptions. Moreover, identifying a suitable trade off between calculated thresholds and operational experience is essential to optimise machine performance. More detailed information on the handling and optimization of the BLM thresholds can be found in [11] and [12].

1.5 Aim of the work

The first proposal of BLM thresholds at collimators was based on energy deposition simulations of regular cleaning, assuming the design maximum power loss of 100 kW and 500 kW (depending on the running sum) [2]. BLM thresholds for the TCPs in IR7 at 7 TeV were obtained via dedicated BLM signal simulation. Primary collimators were considered first as

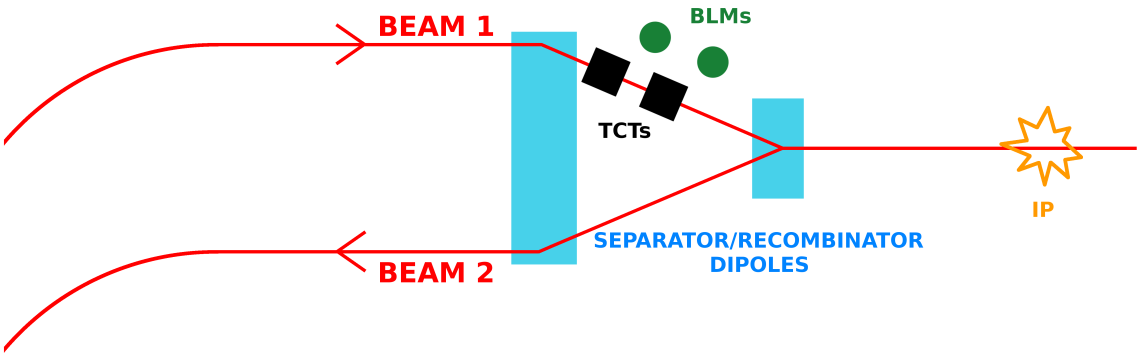

Figure 1.6: Schematics of the location of the TCTs along the beam line.

they are the primary bottleneck of the machine during regular operation and they are hit as first for most sources of operational beam losses [13]. The thresholds for the TCPs were the starting point to derive every other value:

- thresholds at different beam energies were obtained obtained assuming a linear dependence with energy;
- thresholds of all the other collimator families, characterised by different jaw materials, were obtained scaling values for the TCPs with empirical material factors.

Several adjustments to these thresholds were made based on operational needs over the years. This lead to the splitting of the families from the original ones to better take into account the different conditions of each collimator class, e.g. TCLAs are very sensitive to cross-talk effect since they are close to the TCPs of the other beam. Furthermore, flat top and injection corrections modified the original dependence with beam energy for selected values of energy and running sums, e.g. it was decided to reduce the original power loss limits at flat top by a factor 2.5.
To review the BLM thresholds, sensitivity studies of the BLM signal need to be carried out on aspect that were not fully addressed in the past, such as the dependence of the energy deposition on the jaw material and on different loss scenarios or the dependence of the BLM response on the jaw material, collimator geometry and BLM relative position. A preliminary study has been performed in the past [14–16], where the BLM response to a hitting proton was explored in regular cleaning scenarios, i.e. tertiary halo impacting onto TCTs. The study was more aimed at identifying the main parameters affecting the BLM calibration factor rather than at a review of the BLM thresholds.
Open questions still remain, such as:

- does the linear dependence of the BLM thresholds with beam energy reflect the operational limit at 40 kW and 200 kW?
- the TCTs are the collimators with the least robust jaws: is it possible to improve their protection and is leakage from IR7 the only loss scenario of concern for these collimators?
- operational corrections (e.g. to take into account damage caused by debris from collisions) lead to a proliferation of TCT families: is it possible to improve the picture?

The aim of this work is the review of the BLM thresholds at the TCTs. This family of collimators, located close to the IPs in between the separator/recombinator dipoles as shown in fig. 1.6, has been chosen as the starting point for various reasons. Being made in tungsten, the TCTs have the least robust jaws material. Due to their location, cross-talk from losses on nearby collimators is minimised, simplifying the picture. Furthermore, TCTs families have been modified and reorganised several times in the past, and therefore need some homogenisation. Leaving IR7 BLM thresholds with the role of dumping the beam in case beam power loss is at the limit (i.e. 40 kW and 200 kW), the loss scenario that could be used to define the thresholds for the TCTs is that of a collimator exposed directly to the beam, hence it becomes the primary bottleneck and beam protons directly impact onto the jaw. This situation may arise in case of local orbit distortion or accidental/wrong movement of a jaw. The review is based on numerical simulations, where two steps are carried out for the considered scenarios:

- cleaning simulations, to obtain the impact distribution at the collimator;
- energy deposition simulations, to simulate the interaction with the jaw and the BLM response.

In order to gain confidence in the simulation setup and cross-check the results, the work is complemented by a benchmark against measurements.
The following chapters give a brief introduction to the Physics concepts that constitute the background of the study, namely Accelerator Physics and Interaction of Radiation with Matter (chapter 2), as well as a description of the tools used to carry the simulations (chapter 3. Chapter 4 reports the simulation results, followed by the benchmark against measurements in chapter 5. Finally, chapter 6 reports a new proposal of BLM thresholds based on the results obtained with this work.

Chapter 2

Physics Background

This chapter gives a brief introduction to the physics of high energy accelerators, collimation theory and interaction of radiation with matter. Fundamental concepts of these subjects will be used throughout this thesis. A more extensive description of accelerator physics can be found in [17] and [18], while comprehensive summaries on the interaction of radiation with matter can be found in [19], [20] and [21].

2.1 Basics of Accelerator Physics

In this section the fundamental concepts of the physics of high energy accelerators that will be used in the thesis are briefly recalled.
The considered situation in the following is that of a particle circulating in a circular accelerator and experiencing only linear magnetic fields (i.e. only dipoles and quadrupoles). Coupling between motion on vertical, horizontal and longitudinal planes will be assumed to be negligible. In the approximation where there is no coupling between motion on vertical, horizontal and longitudinal planes, longitudinal and transverse dynamics can safely be separated. The longitudinal plane is described by the coordinates s and δ (momentum/energy offset), while the transverse coordinates will be called z and z'. The description of the motion on the transverse plane remains valid for both the horizontal and vertical case. z and z' are the *canonical coordinates* that define the transverse phase space.
The bending magnets define a nominal trajectory that is assumed as reference for the beam motion. An *ideal particle* is a beam particle that has the correct values of energy, momentum and position such that it steadily travels along the nominal orbit and it is also synchronised with the accelerating radiofrequency (RF) cavities. On the other hand, in real conditions beam particles often have a certain offset in terms of energy, momentum and position with respect to the ideal particle, resulting in a transverse displacement z_T that varies with the longitudinal position.
The total transverse displacement of a particle is the sum of two contributions:

- the betatron displacement z_β, fully independent of the energy offset with respect to the on-momentum particle;
- the transverse displacement z_s associated to the dispersion, fully dependent on the relative momentum offset with respect to the ideal particle.

The betatron displacement is a consequence of the focusing magnets that keep the beam particles on the nominal trajectory, resulting in *betatron oscillations* on the transverse plane

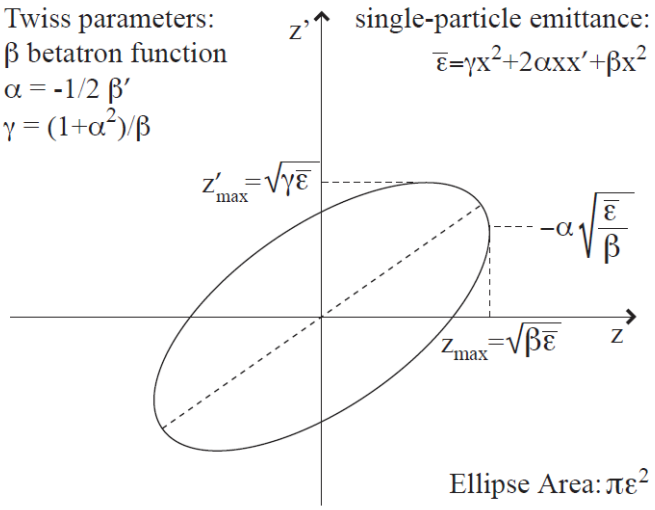

Figure 2.1: Orbit in the transverse $z - z'$ phase space for a particle with design momentum $(p_i - p_0 = 0)$ [22].

around the orbit of the ideal particle. The oscillations are described by the following equations:

$$\begin{aligned} z_\beta &= a_z \sin\phi_z \\ z'_\beta &= \tfrac{a_z}{\beta}(\cos\phi_z - \alpha\sin\phi_z) \end{aligned} \tag{2.1}$$

thus describing an ellipse in the $z - z'$ phase space, as shown in fig. 2.1. a_z is the amplitude of the betatron oscillation, while β and $\alpha = -\frac{1}{2}\frac{d\beta}{ds}$ are the Courant-Snider optical functions (also called Twiss parameters) for the z direction at the s coordinate. The phase ϕ_z itself is a function of the longitudinal coordinate and is related to the β function via the following equation:

$$\phi_z(s) = \int_0^s \frac{ds'}{\beta(s')} \tag{2.2}$$

For each particle it is possible to define a constant of motion called *single-particle emittance*, which satisfies the following equation:

$$\bar{\epsilon}_z = \gamma z^2 + 2\alpha z z' + \beta z'^2 \tag{2.3}$$

which is in fact an ellipse in the phase space. The quantity $\gamma = \frac{1+\alpha^2}{\beta}$ completes the set of the Twiss parameters. Considering the full set of particles composing the beam, the *beam emittance* ϵ_z is defined as the rms value of the single-particle emittances. Finally, the rms beam size σ_z and the rms divergence σ'_z expressed by the following equations:

$$\begin{aligned} \sigma_z &= \sqrt{\beta\epsilon_z} \\ \sigma'_z &= \sqrt{\gamma\epsilon_z} \end{aligned} \tag{2.4}$$

Quantities such as the betatron amplitude or the gap of a given collimator are usually expressed in terms of the rms beam size at the corresponding longitudinal coordinate, such as:

$$a_z = n_z \cdot \sigma_z \tag{2.5}$$

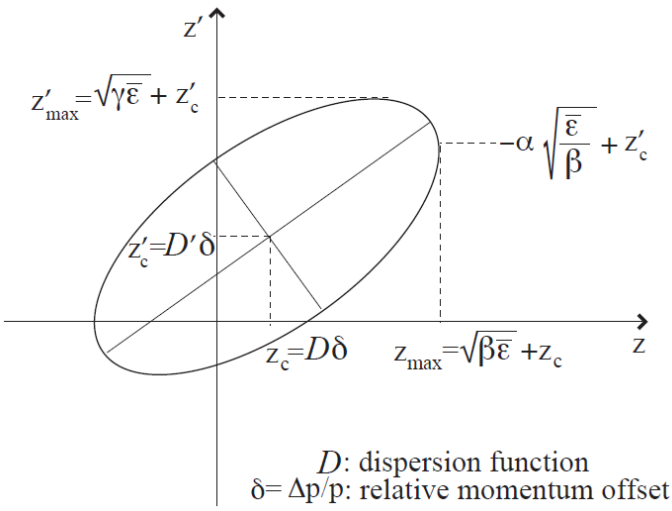

Figure 2.2: Orbit in the transverse $z - z'$ phase space for a particle with momentum offset $\delta = \frac{\Delta p}{p_0}$ [22].

where n_z is the normalised betatron amplitude.
The displacement associated to the dispersion is a consequence of the presence of RF cavities. These are set to accelerate properly only the ideal (synchronous) particle or compensate for energy losses per single turn (e.g. synchrotron radiation). Particles with slightly higher or lower momentum experience different RF kicks and this results in *synchrotron oscillations* of the relative momentum offset $\delta = \frac{\Delta p}{p}$ around the synchronous particle:

$$\delta = a_s \sin \phi_z \tag{2.6}$$

where a_s is the synchrotron amplitude. The relative momentum offset is related to the transverse displacement via the dispersion D:

$$\begin{aligned} z_s &= D\delta \\ z'_s &= D'\delta \end{aligned} \tag{2.7}$$

This displacement acts as a translation of the phase space ellipse described by the betatron motion, as shown in fig. 2.2. The rms momentum offset of the beam from the design momentum p_0 is defined as:

$$\sigma_p^2 = \frac{1}{N}\sum_{i=1}^{N}(p_i - p_0)^2 \tag{2.8}$$

Finally, the synchrotron amplitude can be expressed in terms of the rms momentum offset:

$$a_s = n_s \frac{\sigma_p}{p_0} \tag{2.9}$$

The total transverse displacement at the s position is then:

$$z_T = n_z \sqrt{\beta\epsilon} \sin \phi_z + D \cdot n_s \frac{\sigma_p}{p} \sin \phi_s \tag{2.10}$$

As described in more detail in sec. 2.2, the action of a collimator on a circulating particle can be summed up as a kick $\Delta\theta$ in the transverse phase space. The effect on the betatron motion

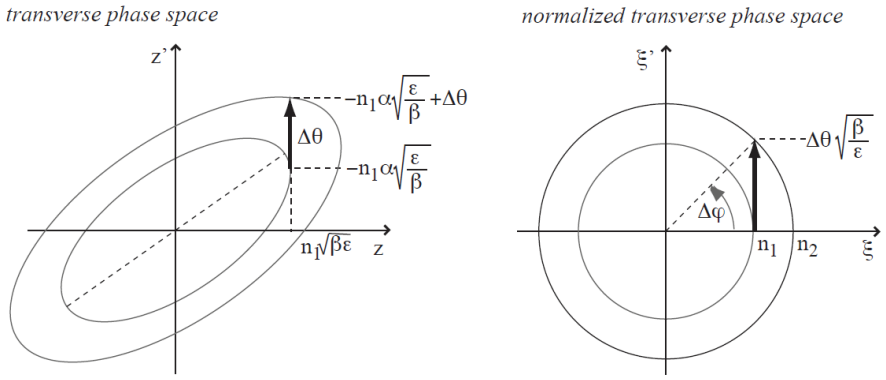

Figure 2.3: Particle receiving a kick $\Delta\theta$ at the maximum of its betatron extensions. The effect is shown in both the transverse phase space and the normalised transverse phase space [22].

becomes clearer when looking at the *normalised* phase space, where Floquet transformations are applied to the canonical coordinates:

$$\begin{array}{rcl} z & \rightarrow & \xi = \frac{z}{\sqrt{\beta\epsilon}} \\ z' & \rightarrow & \xi' = \frac{z\alpha + z'\beta}{\sqrt{\beta\epsilon}} \end{array} \tag{2.11}$$

In this coordinate system, the betatron motion does not follow an ellipse but more simply a circle with radius equal to the normalised betatron amplitude:

$$\begin{array}{rcl} \xi_\beta & = & n_z \sin\phi_z \\ \xi'_\beta & = & n_z \cos\phi_z \end{array} \tag{2.12}$$

Fig. 2.3 shows the effect of a kick $\Delta\theta$ on a particle with normalised amplitude n_1, assuming the kick is received when the particle reaches the maximum of its betatron extension. It takes the particle to a higher betatron amplitude orbit and it also generates a shift in phase. In the normalised phase space, the kick $\Delta\theta$ becomes $\Delta\theta\sqrt{\frac{\beta}{\epsilon}}$ and the expression for the new amplitude n_2 and the phase shift $\Delta\phi$ are the following:

$$\begin{array}{rcl} n_2 & = & \sqrt{n_1^2 + \Delta\theta^2 \frac{\beta}{\epsilon}} \\ \Delta\phi & = & -\mathrm{sgn}(\Delta\theta)\arccos\left(\frac{n_2}{n_1}\right) \end{array} \tag{2.13}$$

The kick $\Delta\theta$ is considered positive when directed outward with respect to the orbit and gives a negative phase shift, since the phase advance is considered here clockwise.

2.2 Application of Linear Dynamics to Multi-Staged Collimation Systems

When dealing with real machines and real beams, the fact that particles drift outwards, generating the beam halo, must be taken into account. Even though the beam emittance is generally considered to be a constant of motion, a series of processes slowly vary the amplitude of the betatronic oscillation. In addition to that, for large distances from the geometrical centre, non-linearities of the magnetic fields become more important. This means that the *dynamic aperture*, i.e. the maximum region where the particle motion is stable, is usually smaller than the *mechanical aperture* of the machine. Moreover, it is very

important to avoid large energy deposition over sensitive regions of the machine, especially when dealing with superconducting components. For all these reasons, an efficient cleaning system is required for high energy machines like LHC, in order to constantly get rid of the halo without damaging critical components at the same time. A multi-stage collimation system, consisting in a series of collimators with different apertures, was found to be the most suitable for the LHC and has been installed accordingly.
In sec. 2.1, any coupling between the motion on the transverse and longitudinal axes has been neglected. This allows to split the collimation system in two distinct sections, dedicated to the cleaning of particles with high betatron amplitude and high momentum offset respectively. These two task have conflicting requirements:

- betatron cleaning requires regions with low dispersion, so that high transverse displacement corresponds to high betatron amplitude;
- momentum cleaning requires regions with high dispersion, so that high transverse displacement is mainly caused by high momentum offset.

For this reason, the LHC collimation system includes two cleaning insertion with different features to complete both these tasks.

2.2.1 Betatron cleaning

As previously stated, betatron cleaning requires a region of zero dispersion. To assure high efficiency, more than a family of collimators is installed providing multiple cleaning steps:

- *primary collimators* are the primary machine bottleneck (i.e. are set at the smallest normalised aperture n_1), where particles in the beam tails interact for the first time with the collimation system and hopefully immediately undergo an inelastic event;
- *secondary collimators* are set to a larger normalised aperture $n_2 > n_1$ in order to intercept and possibly absorb what leaks from the primary collimators;
- higher order families are meant to intercept what leaks from secondary collimators in delicate regions where beam cleaning needs to be handled with particular care.

The system is optimised if all the particles scattered by the primary collimator are scattered by the secondary collimator. This is achieved when:

- the normalised amplitude of the scattered particle is equal or larger than n_2. The minimum kick to get the required amplitude is obtained from eq. 2.13:

$$\Delta\theta_{opt} = \pm\sqrt{\frac{\epsilon}{\beta}(n_2^2 - n_1^2)} \tag{2.14}$$

- the phase advance of the secondary collimator is such that the scattered particles are once again at their maximum excursion when they reach the collimator location. Since eq. 2.14 shows that the kick can be positive or negative, two sets of collimators are required in order to cover the phase shift corresponding to both situations (as shown in fig. 2.4):

$$\begin{array}{rcl} \Delta\phi_{opt+}^{coll} & = & \arccos\left(\frac{n_2}{n_1}\right) \\ \Delta\phi_{opt-}^{coll} & = & \pi - \arccos\left(\frac{n_2}{n_1}\right) \end{array} \tag{2.15}$$

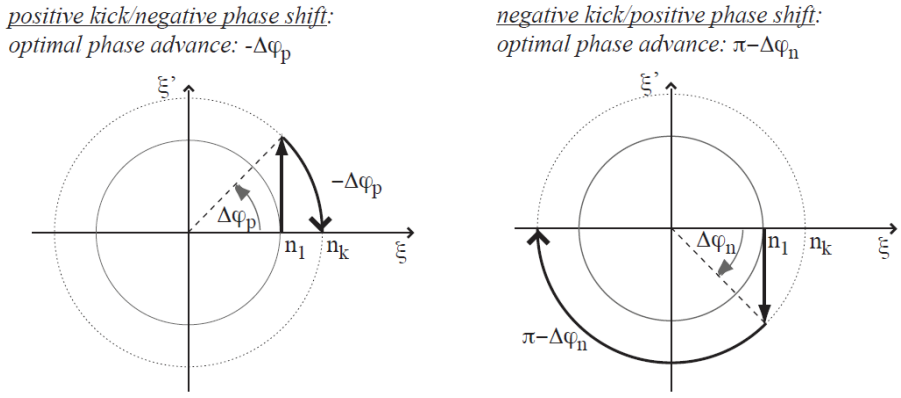

Figure 2.4: Negative and positive kick, with corresponding optimal phase advance required [22].

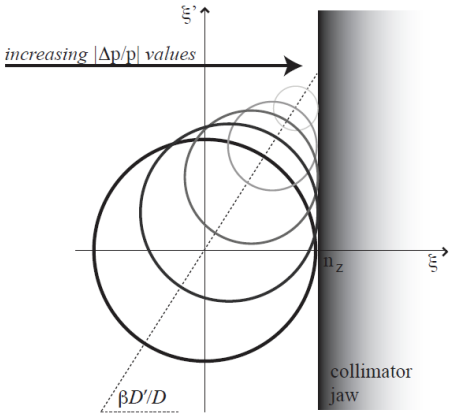

Figure 2.5: Off momentum particles grazing the collimator edge [22].

2.2.2 Momentum cleaning

While in regions with zero dispersion only pure betatron cleaning can be performed, high dispersion is required for momentum cleaning. This is very important since the RF cavities of the machine define a maximum acceptable value of relative momentum offset δ, usually referred to as *RF bucket*. Particles inside the bucket periodically oscillate around the nominal momentum, while particles outside the bucket are eventually lost and therefore must be removed. As shown in fig. 2.5, a collimator whose normalised amplitude is set to n_z cuts different off momentum particles, according to the following equation:

$$n_0\sqrt{\beta_z\epsilon_z} + \delta D_z = n_z\sqrt{\beta_z\epsilon_z} \tag{2.16}$$

This equation describes a line in the $n_0 - \delta$ plane, assuming the ideal situation where there is no dependence of the particle momentum on the optical functions. This is generally true for particles in the RF bucket. It is also important to remark that momentum cleaning necessarily implies a coupling with betatron cleaning, as there is no way to have a null β function (whereas it is possible to have a null dispersion) and as such off-momentum particles generally have a non-negligible betatron component as well.

2.2.3 Loss modelling

A collimation system is expected to comply with different mechanisms of losses. These can be divided in two main categories [23]:

- *continuous beam losses*, which are in general multi-turn losses with time constant rate. They include all the mechanisms that lead to emittance growth and to the population of the primary halo (intra-beam scattering, beam instabilities, transverse resonances, collisions at IPs...);
- *accidental beam losses*, which include single-turn losses, where a fraction of the beam is sent on abnormal orbits. They have high destructive potential and are caused by errors during injections, asynchronous beam dumps (during which the extracting magnets are not synchronised with the abort gap of the fill), dynamic changes during the transitions between different configurations of the machine (ramp, squeeze...) and wrong actions or incidents requiring a dump.

The cleaning performance of a collimation system can be quantified by the *collimation efficiency*, which expresses the fraction of halo particles caught by the system over the total lost from the beam. With this definition, a perfect beam collimation system (i.e. if collimators were of infinite absorbance) should provide 100% cleaning and no losses would leak out of the collimation system and be found at sensitive locations. On the other hand, when dealing with real systems it is more common to refer to the *local cleaning inefficiency*. This quantity is function of the longitudinal coordinate s and it is defined as the number of particles lost over the distance Δs over the number of particles absorbed by the collimators:

$$\eta_c = \frac{N(s \to s + \Delta s)}{N_{\text{abs}}} \frac{1}{\Delta s} \tag{2.17}$$

Continuous losses lead to a decrease of the beam intensity, which can, for most practical purposes, be described by an exponential decay function:

$$I(t) = I_0 \mathrm{e}^{-\frac{t}{\tau_\mathrm{b}}} \tag{2.18}$$

where the time constant τ_b defines the *beam lifetime*. This is actually a function of time in itself and is not constant through the operational cycle. A conservative value of minimum lifetime throughout the operation cycle must be assumed in order to ensure the required cleaning in any machine condition. For the LHC, this has been estimated as $\tau_{min} = 0.2$ h [24]. Knowing the quench limit of superconducting magnets R_q, it is possible to calculate the maximum circulating intensity in a superconducting machine for which safe operations are assured [25]:

$$I_{max} \leq \frac{R_q \tau_{min}}{\eta_c} \tag{2.19}$$

This equation can be used also to set the maximum acceptable local cleaning inefficiency, knowing the maximum intensity needed to achieve the required performance of the accelerator (i.e. the desired luminosity and rate and the IPs) and the quench limit. This condition should drive the design of the collimation system of a superconducting accelerator.

2.3 Interaction of Radiation with Matter

When a beam particle interacts with the active region of a collimator jaw, a wide series of events may take place. In the case of LHC beams, the spectrum of phenomena extends

from particle-nucleon interactions at hundreds of GeV in the centre-of-mass reference system down to low-energy nuclear interactions in the meV energy range. The net effects of these processes are:

- the *loss* of the particle or its *survival*, with different direction and energy: surviving particles continue their path following a different orbit and are ultimately lost downstream along the ring, determining the pattern of losses along the beam line;
- the generation of *secondary particle showers*, that propagate inducing thermal loads, mechanical stresses and radioactivity in the impacted area.

This section presents some basic concepts about the interaction of radiation with matter and describes the many different processes that can take place in the scenarios simulated in this work.

2.3.1 Ionisation

A massive charged particle, such as a proton, travelling through matter mainly loses energy through collisions with the atomic electrons of the medium, leading to the ionisation of the medium itself if the energy loss is high enough. The mean energy loss per unit path length, called *stopping power*, is described by the Bethe-Bloch equation:

$$-\left\langle \frac{dE}{dx} \right\rangle = Kz^2 \frac{Z}{A} \frac{1}{\beta^2} \left[\frac{1}{2} \ln \frac{2m_e c^2 \beta^2 \gamma^2 T_{max}}{I^2} - \beta^2 - \frac{\delta(\beta\gamma)}{2} \right] \tag{2.20}$$

This formula shows that the mean energy loss depends on:

- the following properties of the travelling particle:
  - its charge z;
  - its relativistic factors β and γ;
- the following properties of the material:
  - its atomic number Z;
  - its atomic mass A;
  - its mean ionisation potential I.

T_{max} is the maximum kinetic energy which can be transferred to a free electron in a single collision and δ represents the effect of the polarisation of the material, which becomes more and more important as the momentum of the particle rises. Finally, K is a constant defined as such:

$$K = 4\pi N_A r_e^2 m_e c^2 \tag{2.21}$$

A plot of the Bethe-Bloch is shown in left frame of fig. 2.6. Three regimes can be identified:

- at low momentum, the travelling particle interacts for a long time with the atomic electron of the material and the energy transfer is high. As the momentum increases, the energy loss becomes lower, until it reaches a minimum at $\beta\gamma \simeq 3$ (minimum ionising particle, MIP);

- at higher momentum the energy loss rises again because the medium appears to have a higher density since effects related to the relativistic length contraction become noticeable;
- at even higher momentum the field generated by the travelling particle polarises the medium, generating a screen effect that stabilises the energy loss.

It is worth noting that the Bethe-Bloch equation describes the *mean* energy loss per unit path length: the interaction is a stochastic process and the probability that the particle loses the energy Δ in the path length x is actually described by a Landau distribution (shown in the right frame of fig. 2.6).

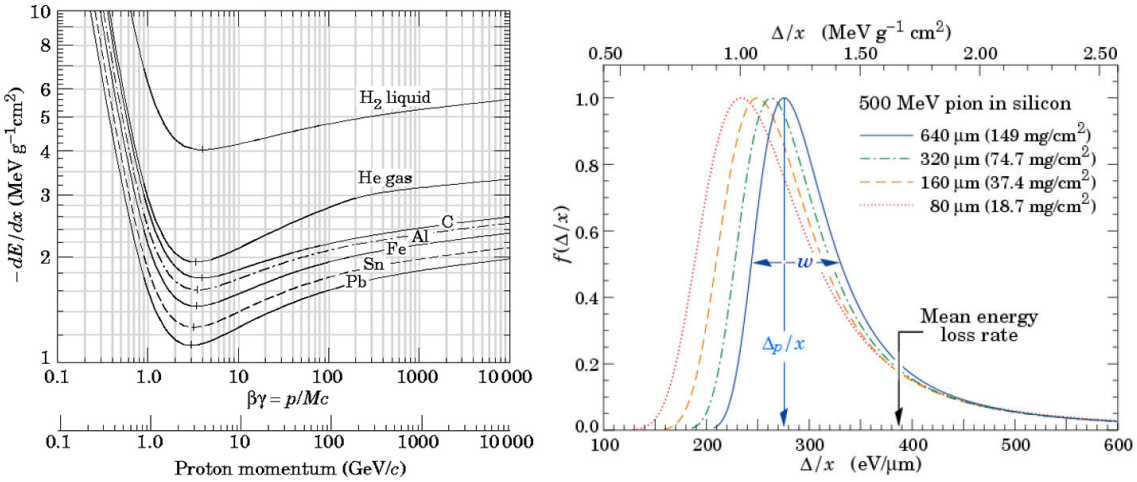

Figure 2.6: Left frame: Bethe-Bloch function in different materials with respect to the relativistic reduced momentum $\beta\gamma$ and the proton momentum [19]. Right frame: Landau distribution for the energy loss of 500 MeV pions in silicon layers [19].

2.3.2 Multiple Coulomb Scattering and Rutherford Scattering

A charged particle traversing a material experiences multiple deflections due to Coulomb scattering onto atomic nuclei, as shown in fig. 2.7. The final angular distribution of the particles exiting the medium is described by the Molière theory of Multiple Coulomb Scattering (MCS) and it has a Gaussian core with larger tails due to single Rutherford scattering events at big deflection angles.

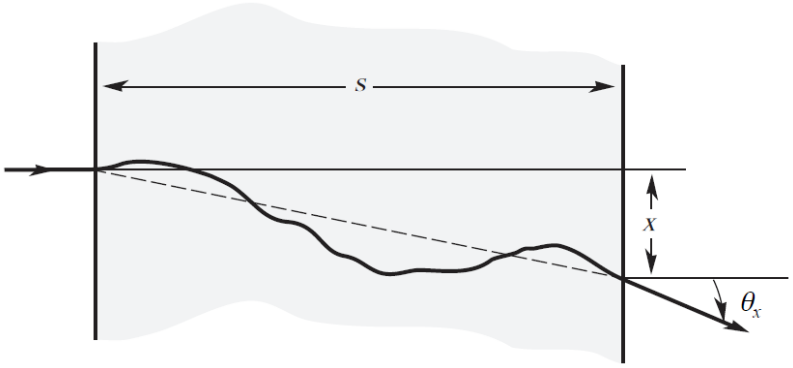

Figure 2.7: Example trajectory of a particle experiencing Multiple Coulomb Scattering while crossing a block of material. The particle exits from the block with a deflection angle θ_x.

2.3.3 Nuclear Scattering

Nuclear elastic and inelastic scattering events are responsible for the largest variations in energy and direction of the primary beam particle or for its loss to the beam ad the start of secondary particle showers.
In nuclear *elastic* scattering, the particle survives the interactions and changes its energy and direction, much like what happens in ionisation and MCS. On the contrary, in nuclear *inelastic* scattering the interacting particle is lost and new secondary particles are produced. These are therefore the main source of secondary showers, which are responsible for a significant fraction of the energy deposition in the collimator jaws and hence induce thermo-mechanical stresses.
A particular kind of inelastic nuclear reaction which is relevant at LHC beam energies is *single diffractive scattering* (SD). This is a quasi-elastic process where momentum transfer during collision implies a high mass excitation state for one of the interacting particles. Particles experiencing SD have a non-zero probability to generate a new particle of the same kind able to escape from the collimator jaw and to contribute to the population of the off momentum halo, even if particles were on-momentum originally. In a SD event, a proton undergoes an inelastic interaction with a nucleus; the interaction excites the nucleus and causes the emission of another proton with nearly the same direction as the original one, but much different energy. The new proton is inevitably lost on the machine aperture, making single diffractive scattering a concerning phenomena for collimation purposes.

2.3.4 Secondary Particle Showers

Secondary particle showers are generated when a high energy particle interacts with a piece of material, e.g. a collimator jaw or a magnet. The incoming particle interacts, producing multiple new particles with lesser energy; each of these then interacts in the same way in a sort of chain reaction. This process is terminated once the generated particles no longer have enough energy to interact inelastically with the medium with production of new particles. Secondary particle showers have two main components:

- the *hadronic shower*, which is generated when a hadron travelling through the material interacts inelastically with a nucleus and produces new hadrons at a lower energy. The average distance between two subsequent interactions of the primary particles is expressed by the inelastic interaction length λ_I, which as such gives also an indication of the extension of the hadron cascade;

- the *electromagnetic shower*, whose main events are electron-positron pair production by a photon and photon emission by an electron or positron via bremsstrahlung. The typical scale of the EM cascade is given by the radiation length X_0, i.e. the average length over which an electron, positron or photon interact. The transverse development of the shower is expressed by the Molière radius R_M:

$$R_M = X_0 \frac{21\ \text{MeV}}{E_c} \tag{2.22}$$

  where E_c is the critical energy, defined as the value at which the energy loss rate due to bremsstrahlung and ionisation are equal. The critical energy is given by the following equation:

$$\left\langle \frac{dE}{dx}(E_c) \right\rangle = \frac{E_c}{X_0} \tag{2.23}$$

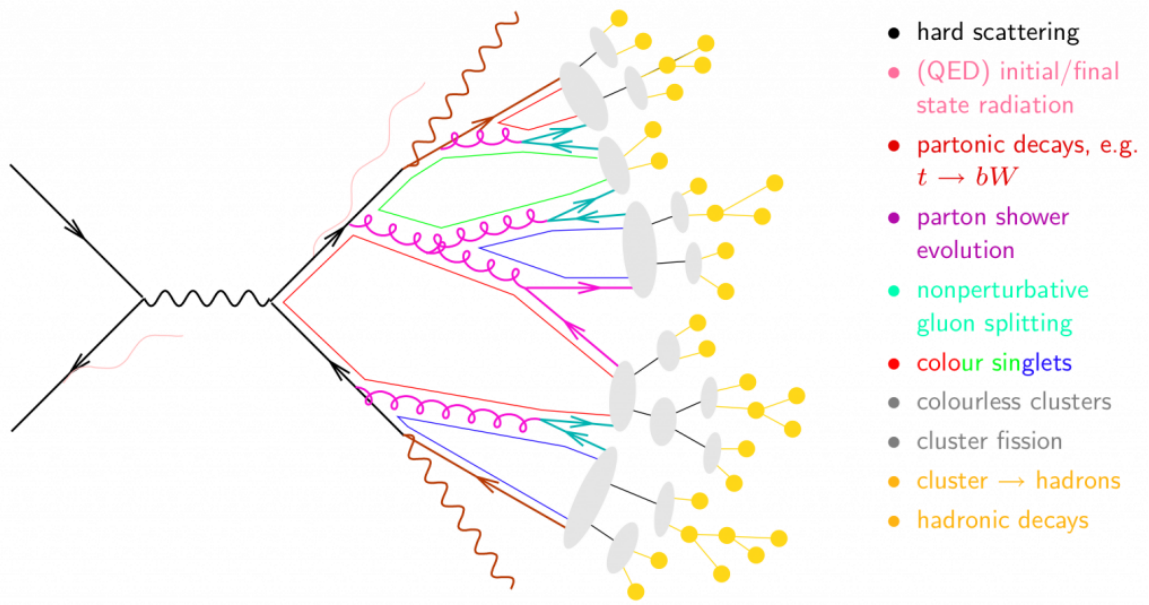

Figure 2.8: Sketch of the development of a hadronic shower.

EM cascades are always present during hadronic cascades. Whenever a π^0 is produced, its fast decay into two photons starts its own EM shower. The opposite is also true, but to an extent. Hadronic cascades are ignited during an EM cascade via photonuclear reactions, that are much less frequent due to the low values of the corresponding cross section.
EM showers are mainly responsible for high levels of energy deposition in the active region of the collimator. Hadronic showers, on the other hand, deal with nuclear inelastic events and as such leave nuclei in an excited states. The main consequences are the attenuation of the primary beam and the induction of radioactivity in the collimator jaw, depending on its material and geometry.

Chapter 3

Simulation Tools

The aim of this work is a review of the BLM thresholds at the TCT collimators of the LHC via numerical simulations. To do this, it is important to correctly estimate the loss distribution impacting on the collimator jaw and the energy deposition induced by secondary particle showers started by the impacting protons, in order to correlate it with the BLM signal in the same scenario. This chapter describes the two main simulation tools used in this work:

- **FLUKA** [26,27]: a Monte Carlo code which simulates the interaction of beam particles with the intercepting device and the secondary particle showers thus started;
- **SixTrack** [28–31]: a tracking code that simulates the single-particle beam dynamics in the accelerator.

Both codes are widely used at CERN. FLUKA is used for beam-machine interaction studies, like energy deposition in magnets, BLM signals, induced radioactivity, etc. SixTrack is used especially for collimation and dynamic aperture studies. Hence, the former is used to estimate the energy deposition in the collimator jaw and the signal in the BLMs, starting from the distribution of impacting protons generated with the latter. To be more specific, SixTrack is used coupled with FLUKA, in order to describe more accurately the scattering of protons on the jaw material.
The following sections will give an overview of the two codes, as well as a description of their coupling.

3.1 FLUKA

FLUKA is a fully integrated Monte Carlo code. It is a general purpose tool for calculations of particle transport and interactions with matter, covering an extended range of applications spanning from proton and electron accelerator shielding to target design, calorimetry, activation, dosimetry, detector design, Accelerator Driven Systems, cosmic rays, neutrino physics, radiotherapy, etc. FLUKA can simulate with high accuracy the interaction and propagation in matter of about 60 different particles, including photons and electrons from 1 keV to thousands of TeV, neutrinos, muons of any energy, hadrons of energies up to 20 TeV and all the corresponding antiparticles, neutron down to thermal energies and heavy ions.
FLUKA is maintained at CERN with the aim of including the best possible physics models in terms of completeness and precision, and it is continuously upgraded and benchmarked

against experimental data. It is widely used in particular for MC analysis concerning beam-machine interaction. For example, in this work it will be used to estimate the energy deposition in beam-intercepting devices and BLM signals.
All the necessary information in input to the code is gathered in only one text file, which contains a set of *FLUKA cards* describing each aspect of the system to simulate, including the physics and transport settings, the geometry to be used with the definition of materials and the scoring options (i.e. the quantities to be estimated). Thanks to the infrastructure for accelerator studies set up by the FLUKA team [32], most of these settings are available in the form of templates, and the users need to manually adapt the code only for specific needs. For example, the models of all the beam intercepting devices and the general geometry of the LHC is already available. Furthermore, it is possible to visualise the geometry and better manage the input file via a Graphical User Interface (GUI) named *Flair* [33], which can be used to generate/modify the input file, manage jobs and plot quantities, in particular energy deposition results.
The FLUKA simulations performed in this work receive in input the impact distribution on the collimator jaws obtained by cleaning simulations with the SixTrack-FLUKA coupling described in sec. 3.3. The protons are sampled at the coordinates given by the map and then backtracked by 100 nm to make sure their starting point is in vacuum. Then their interaction with the jaw material is simulated and the subsequent secondary particle shower is tracked through the whole geometry defined in the FLUKA input file, which includes a detailed reconstruction of the collimator and BLMs. Scoring cards define 3-dimensional grids that cover the active region of each jaw (an example is shown in fig. 3.1), in order to reconstruct the energy deposition profile by scoring the energy deposited in each cell. The BLM response is computed via an additional card that scores the energy deposition over the entirety of the active gas volume of the ionisation chamber.

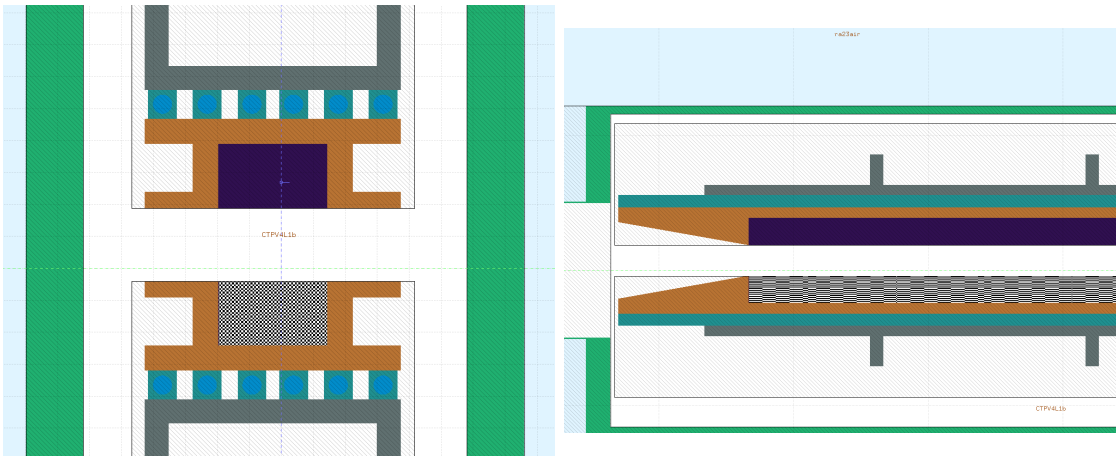

Figure 3.1: Schematics of a collimator created with Flair from the FLUKA input file, seen from the transverse (left frame) and longitudinal (right frame) plane. The 3-dimensional mesh used for the energy deposition in the negative jaw is shown as a black and white grid.

3.2 SixTrack

SixTrack is a code for simulating beam dynamics in circular accelerators. Being a single particle tracking code, each particle is treated independently, without taking into account collective effects. The machine in which the simulated beam moves is described by a lattice containing all the different elements (i.e. magnets, RF cavities, collimators, etc.) and the

coordinates of each particle in the six-dimensional phase space ($x - x'$, $y - y'$, $s - E$) are updated throughout the whole lattice element by element. Symplectic integrators are used to derive the transport maps of the modelled devices. Each device is modelled using the thin lens approximation, i.e. is identified by a marker placed in the middle of the physical extension of the device, or more than one marker in case of particularly complex elements (such as the magnets of the inner triplets). When the particles reach a marker, their coordinates are updated with the effect of the interaction with the corresponding object before continuing the tracking. SixTrack was originally designed to study the dynamic aperture (defined in sec. 2.2) in circular machines. For this reason it is optimised to track couples of particles with slightly different initial coordinates for a large number of turns, to check where their dynamics start to diverge.
SixTrack needs two input files:

- the *fort.2* file specifies the machine lattice and structure and the settings of the magnetic elements (can be automatically generated by MADX [34], a code for optics design and optimisation largely used at CERN);
- the *fort.3* provides the settings of the simulation (manually edited by the user).

There is a specific version of SixTrack dedicated for collimation studies. In this code, essential physics of proton scattering in materials is implemented, so that the interaction of the beam protons with the material is taken into account. An important feature of this version of SixTrack is the online aperture check. The code is able to check whether each tracked particle touches the mechanical aperture of the machine and is thus lost. This is useful to predict the loss position of any beam particle scattered on large amplitudes and determine loss maps. However, this version was not used for this work, as the coupling with FLUKA (described in sec. 3.3) was used instead.

3.3 Coupling between FLUKA and Sixtrack

As explained before, the studies conducted in this work require two steps: the simulation of the impact distribution on the collimator jaws and the simulation of the energy deposition corresponding to that distribution. The cleaning simulations were not performed using the built-in scattering engine of SixTrack itself, but rather as coupled simulations using both SixTrack and FLUKA. FLUKA is widely used at CERN for energy deposition simulations, so using FLUKA also to simulate the impact distribution in cleaning simulations allows to have more accurate and consistent results, since scattering models, material definition and geometry are the same in both simulation steps. Furthermore, as FLUKA is used for a wide variety of applications, its results are continuously benchmarked and its scattering models and routines are more detailed than the ones implemented in SixTrack alone.

3.3.1 Working principles of the coupling

In a SixTrack-FLUKA coupled simulations, tracking of beam particles turn by turn throughout the accelerator lattice is regularly performed by SixTrack. When a device or portion of beam line labelled as *FLUKA insertion region* is reached, particles are sent to FLUKA for tracking in its geometry. Once the tracking in FLUKA is over, surviving particles are sent back to SixTrack, to resume tracking in the accelerator lattice. With such a setup, the beam dynamics in the accelerator is computed by SixTrack, whereas the scattering processes are taken care by FLUKA. In a coupled simulation, FLUKA and SixTrack run separately at the

same time and exchange particles through a network port. The communication protocol is provided by the FLUKAIO Application Programming Interface, which manages the flow of information between the two codes.
With respect to a standard SixTrack simulation, the input file with the simulation settings must be modified, flagging the elements for tracking in FLUKA. The file describing the accelerator lattice needs to be modified as well, inserting a couple of markers for each FLUKA insertion, marking its boundaries[1]. The distance between these two markers (i.e. the *synchronous length* of the FLUKA insertion) is declared explicitly. In addition, the input files to SixTrack are also modified[2] to insert aperture markers, such that the aperture check can be performed during tracking, marking losses along the ring.

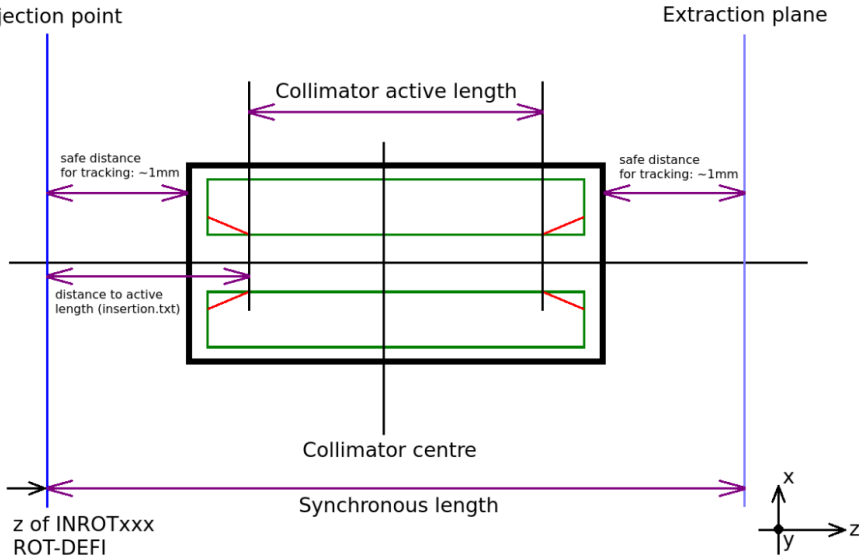

Figure 3.2: Sketch of collimator geometry and reference dimensions [35].

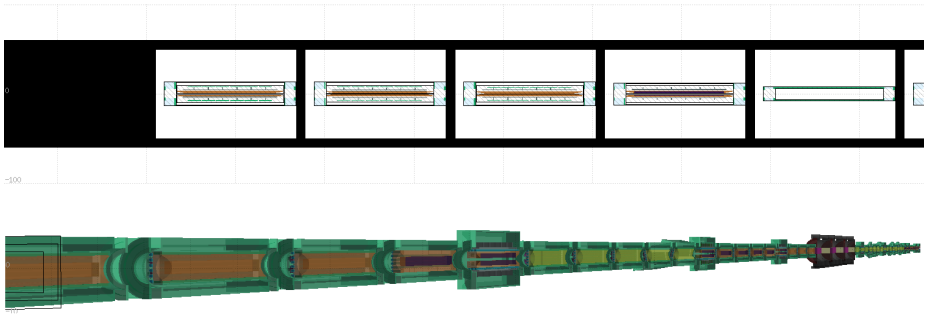

Figure 3.3: 2D and 3D view of the collimator sequence in the FLUKA geometry for a coupled simulation [36].

The FLUKA input file for a coupled simulation is made of a sequence of collimator geometries, with each collimator placed in a dedicated cell surrounded by "black hole" material in order to avoid any cross-talk effect. Collimator appear in the order given by the list of

[1]When the FLUKA geometry extends only on collimators, this is automatically done by a pre-processing script.
[2]The modifications are performed automatically by a pre-processing script.

collimators provided by the user, which reflects the sequence of collimators encountered by the beam particles during their motion along the machine ring. They are arranged longitudinally along the FLUKA z-axis, which coincides with the longitudinal axis of the local curvilinear reference system (i.e. the closed orbit). The transverse displacement is set using the provided *twiss file*. An example of the collimator sequence in the FLUKA geometry is shown in fig. 3.3.
A special set of coordinate transformation (coded via *ROT-DEFI cards*) are used to properly match the reference frame of SixTrack (local curvilinear reference system) with the one of FLUKA (global reference system). Particles coming from SixTrack are injected in the concerned collimator box in the FLUKA geometry at the *injection point* and extracted after the interaction with the jaws to be sent back to SixTrack at the *extraction plane* (both are shown in fig. 3.3. The two are placed 1 mm upstream and downstream of the collimator tank respectively, since it is not safe to start tracking in FLUKA on a surface and scoring on two overlapping surfaces. It is very important that the relative distance between the markers and the collimators and the synchronous length separating the two markers are the same as the ones set in SixTrack, in order to provide accurate and consistent tracking. Fig. 3.2 shows a sketch of the FLUKA geometry and reference dimensions.

3.3.2 Beam distribution sampling

The sampling of the initial beam distribution is done via a Fortran tool called *gpdist*, which is able to generate the most commonly used halo distributions for collimation purposes at a given point of an accelerator lattice structure. This tool requires a configuration file that specifies the following quantities at the sampling point:

- optics functions (i.e. the Twiss parameters), closed orbit and possible offsets at the point of sampling;
- beam properties (i.e. distribution on the transverse plane, normalised emittance and momentum).

The standard simulation setup used for the beam sampling in this thesis uses a Gaussian distribution over a 3 σ interval on the non-cleaning plane, and a flat distribution over a specific σ interval (i.e. in normalised coordinates, refer to sec. 2.1) in the cleaning plane. In order to optimise CPU time, the sampling point of the beam is chosen to be just upstream of the front face of the collimator and matched to the collimator aperture. However, two facts must be taken into account:

- σ depends on the β function, which varies with the longitudinal coordinate and as such does not have the same value at the centre and on the front or back face of the collimator;
- collimators have a certain alignment with respect to the closed orbit, so that one jaw corner may be closer to the beam than another.

For this reason, it is important to calculate first the distance of each jaw corner from the closed orbit in term of number of σ. The one at the smallest normalised amplitude actually performs the cut of the beam and as such is the bottleneck of the system around which the simulated beam must be sampled. An example of this is shown in fig. 3.5.

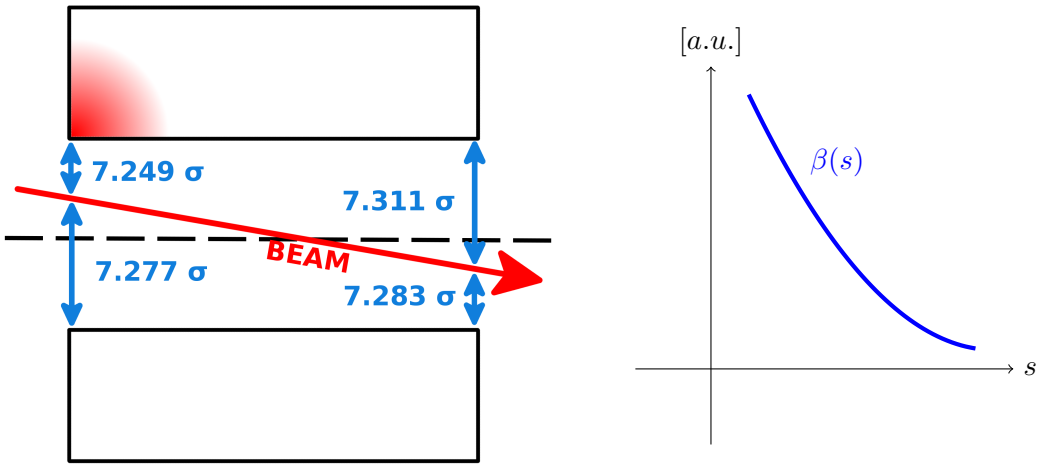

Figure 3.5: Schematics of a horizontal collimator (left frame) and example of behaviour of the β function on the cleaning plane in the collimator (right frame). In the given example, the β function decreases with the longitudinal coordinate (focused beam) and so does σ. For this reason, the front corner of the positive jaw, highlighted in red, is the closest to the beam in terms of normalised coordinates and it determines the actual collimator cut.

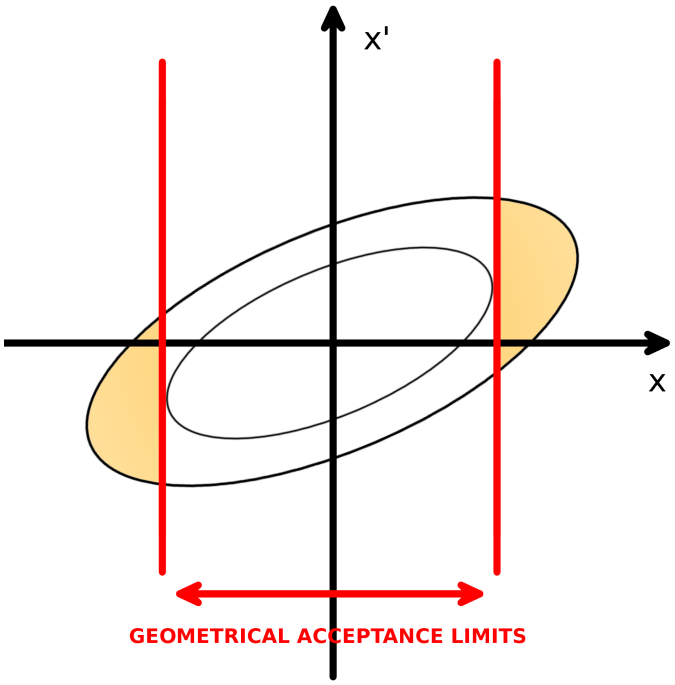

Figure 3.4: Representation of the geometrical acceptance limits on the $x - x'$ phase space. The sampling interval selects the region between the two ellipses, while the geometrical cut leaves only the area highlighted in yellow.

The engine generates particles in the chosen σ interval for all possible phase values. The sampled distribution then covers the area delimited by two ellipses, as shown in fig 3.4 for the $x-x'$ phase space. Clearly most of the particles do not have the correct phase to impact the chosen collimator at the first turn, but at the following ones. Hence, to optimise the

CPU time, a geometrical cut can be performed on the cleaning plane, forcing the sampling engine to populate only the tail of the distribution over the desired number of σ and only on the phases suitable for impacting the collimator immediately at the first turn. This allows to sample mostly particles that really interact with the collimator on the first turn, reducing the number of turns required to lose the whole sampled distribution and therefore speeding up the simulation. Since the sampling point is chosen at a certain distance from the collimator itself in order to correctly sync with the FLUKA portion of the simulation, the tiny phase advance between the sampling point and the jaw is responsible for some protons still being able to escape the collimator jaws, but they are usually lost in a few turns.

3.3.3 Output of the coupled simulation

The main output of a coupled simulation is a list of 6-D coordinates of impacts on the collimators included in the geometry, organised in three categories:

- *first impacts*, containing only the coordinates of the first time each particle interacts with any collimator. This category is important to verify that halo particles hit the collimator where expected (i.e. the settings of the simulations are correct);
- *touches*, containing the coordinates of the first time a particle impacts on a collimator in each turn;
- *inelastic interactions*, containing the coordinates of the particles that experience an inelastic interaction and are therefore lost in the jaw.

In particular, the touches map is the one that is actually loaded in FLUKA for energy deposition studies, while the others serve as cross-checks. With respect to first impacts, this map takes into account multi-turn effect (which are not present in a pure FLUKA simulation as only a single passage of the particles through the collimator is considered). On the other hand, with respect to inelastic interaction, it allows to take into account the contribution of ionisation (which is very important in the simulated scenarios) to the energy deposition in the hit collimator.

Chapter 4

Simulations for the BLM thresholds review

The TCTs are the most delicate collimators of the LHC, since they are made of a tungsten alloy to maximise absorption capability. This increases the energy depositions in the jaws compared to other materials, and hence the BLM signal. For this reason, the BLM thresholds need to be handled with particular care. The main purpose of this work is to review the BLM thresholds applied to the TCTs by means of numerical simulations, involving also the dependence on beam energy.
After choosing the collimator to be used for the study, three different configurations are simulated, namely with both jaws inserted in the beam line and with only one jaw inserted and moving towards the beam, in order to identify the worst case scenario in terms of ratio of the BLM signal over the peak energy deposition. The configuration found in this preliminary step is then used to simulated the BLM response for different beam energies, performing what is referred to as *energy sweep*. The results obtained from the simulations are used to review the current BLM thresholds. This chapter describes the steps of the procedure followed in this work and the achieved results.

4.1 Simulation setup

The simulation setup is composed of two parts:

- *cleaning simulations* using the SixTrack-FLUKA coupling described in sec. 3.3, in order to estimate the impact distribution on the collimator jaws;
- *energy deposition simulations* using FLUKA, in order to estimate at the same time the energy deposition in the collimator jaws from the impact distribution, as well as the BLM signal.

The scenario considered in the review of the BLM thresholds is the one of a jaw that accidentally moves towards the beam. The same simulation setup is also used, in a simplified approach, to represent a distortion in the closed orbit resulting in the drift of the beam towards the jaw.

4.1.1 Cleaning simulations with the SixTrack-FLUKA coupling

In the cleaning simulations, the collimator of interest is set as the primary bottleneck (i.e. the one with the smallest normalised aperture) leaving the rest of the collimation system in

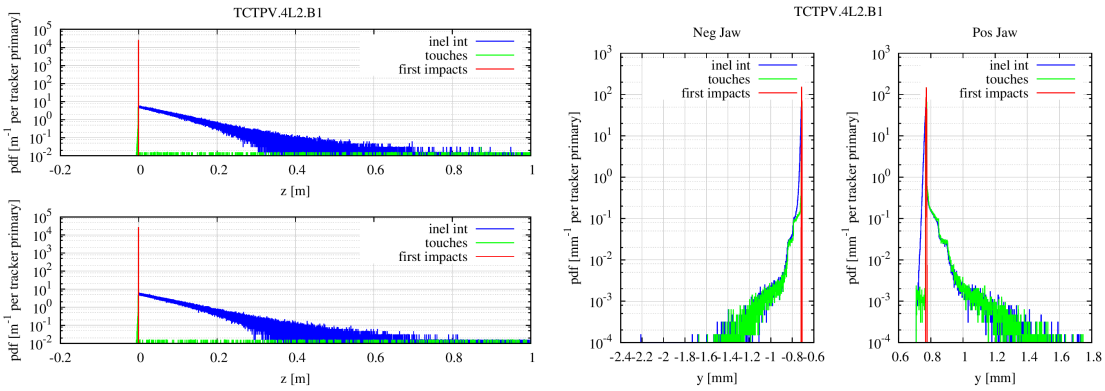

Figure 4.1: Examples of impacts distribution on TCTPV.4L2.B1 for a SixTrack-FLUKA coupled simulation at 7 TeV. The left frame shows the longitudinal distribution (positive jaw on the upper plot, negative jaw on the lower plot), while the right frame shows the distribution on the cleaning plane.

place. The included collimators and their normalised aperture are reported in tab. 4.1. The only difference from the nominal collimator settings is the aperture of the TCTPV.4L2.B1, which is the collimator chosen for this study and is set as the primary bottleneck (see sec. 4.2). The halo is sampled within the following distributions on the two planes:

- a Gaussian distribution within 3 σ on the non cleaning plane;
- a flat distribution within a certain number of σ around the collimator aperture on the cleaning plane.

Collimators		**Aperture [number of σ]**
IR7	TCP / TCSG / TCLA	5.5 / 7.5 / 11.0
IR3	TCP / TCSG / TCLA	15.0 / 18.0 / 20.0
IR6	TCSP / TCDQ	8.3 / 8.3
TCTs	IR1 / IR2 / IR5 / IR8	23.0 / 37.0 / 23.0 / 23.0
	TCTPV.4L2.B1	5.0

Table 4.1: Collimator settings for the cleaning simulation at 7 TeV.

Cleaning simulations, as described in sec. 3.3.3, return the coordinates of the interactions of the beam particles with the collimators included in the geometry, organising them in first impacts, touches and inelastic interactions. An example of these distributions in shown in fig. 4.1. Since the beam particles have been sampled in such a way that the vast majority of them interacts with the collimator on the first turn, first impacts are always located at the boundaries of the jaws both in the longitudinal and the cleaning plane. On the other hand, touches are the coordinates of the interaction of the particles with a collimator regardless of the turn it takes place in. For this reason, they are once again concentrated on the boundaries of the jaw, but they show distinct tails due to particles that are not lost after the first impact and continue their motion along the ring for more than one turn, modifying the initial beam distribution due to the change in energy and direction caused by each interaction. Inelastic interactions are the result of the different processes a particle undergoes while traversing the jaw material, and therefore the longitudinal profile show that they are distributed all over the active length of the jaw.

Each simulation samples 700 couples of beam particles and the tracking is performed for up to 2000 turns, which is enough for most of the initial halo particles to be lost on the collimators or on the machine aperture. The first simulations sample the beam at IR1, which is the default location since here the closed orbit has a small offset with respect to the machine axis, with a sampling interval of 0.2 σ around the collimator aperture. This allows to check that the settings of the collimators (i.e. aperture and eventual tilt with respect to the closed orbit) have been correctly implemented in the simulation. However, it is much more convenient to sample only particles that interact with the desired collimator in the first few turns. For this reason, the final simulation setup starts right at the front face of the collimator, adjusting the sampling interval to be 0.01 σ wide according to the value of the β function upstream of the jaw and applying a geometrical cut as described in sec. 3.3.2.

4.1.2 Energy deposition simulations with FLUKA

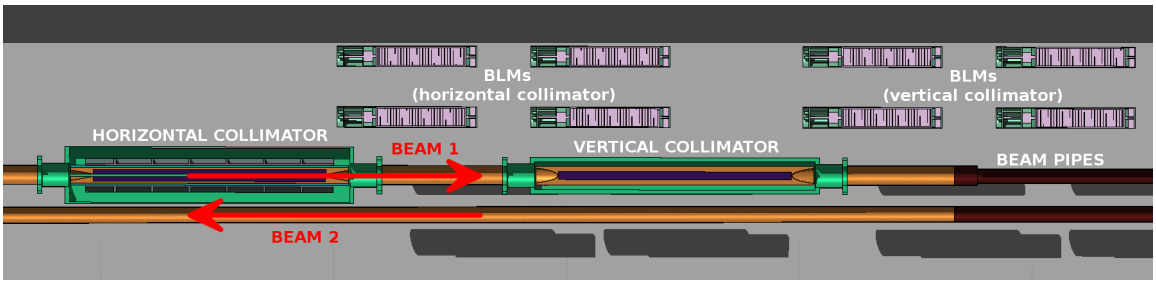

Figure 4.2: 3D representation of the FLUKA geometry left of IP2 realised with Flair. The main elements of the geometry (i.e. the collimator tank and jaws, the BLMs, the beam pipes, etc.) can be seen.

The second simulation step uses the touches distribution as an input to the FLUKA geometry, which includes only a reconstruction of the collimator of interest, the beam pipes and a set of BLMs (an example can be seen in fig. 4.2) whose orientation can be set as horizontal or vertical depending on the desired scenario. Each ionisation chamber has a volume of 1524 cm^3 and houses 1.906 g of N_2 gas. For a typical FLUKA simulation, 10^5 protons are randomly sampled out of the distribution of impacts. Each collimator jaw in the FLUKA geometry is equipped with three meshes with progressively smaller pixels in order to score the energy deposition in of GeV/cm^3 per primary and reconstruct the profile along the jaw. Examples of these profiles are shown in fig. 4.3. Since they are extremely concentrated and show high gradients in small distances, only the finest of the three meshes, consisting of 5 μm x 5 μm pixels on the transverse plane with 1 cm steps on the longitudinal axis, has been used to best resolve the distributions. An additional scoring card allows to compute the total energy deposition in the region of the BLMs housing the N_2 gas in order to calculate the signal response to the beam impact on the jaws. The output coming from the BLMs is then processed with a Python script that returns the BLM response factor (also called *calibration factor* in this work), that is to say the conversion factor from protons lost on the collimator to the signal read by the BLM (in pGy per lost proton). It is important to pay attention to the fact that FLUKA results need to be re-normalised, as they are expressed per FLUKA primary (i.e. per touch) and not per proton lost. The results must then be multiplied by the ration of the total number of touches over the total number of lost protons (i.e. the total number of sampled particles in the cleaning simulation minus the ones that are still not lost after the last simulated turn).

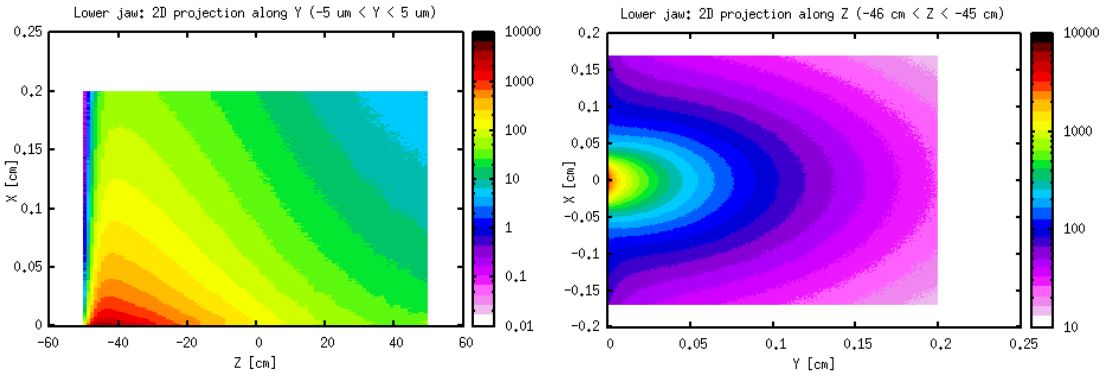

Figure 4.3: Examples of energy deposition profiles on the lower jaw of TCTPV.4L2.B1 aligned with the closed orbit, obtained with FLUKA and plotted with Flair. The left frame shows a 2D projection on the longitudinal plane, the right frame shows a 2D projection on the transverse plane.

4.2 Choice of the configuration

The LHC collimation system includes a total of 16 TCTs (i.e. a pair of collimators upstream of each experiment for each beam), each of them has its dedicated BLM: since the relative position of BLM and collimator is not always the same, different signals for each collimator can be expected assuming the same impact distribution. Simulating all of these different situations would require a lot of time. Therefore, it has been decided to consider only the worst scenario, i.e. the one that shows the smallest ratio between the BLM response and the peak of the energy deposition profile (i.e. the smallest signal corresponding to the highest energy deposition). The thresholds need to be conservative enough to assure protection of the collimators under the most unfavourable situation. For this reason, a first selection has been applied between the TCTs, choosing the one at which the beam distribution on the non-cleaning axis (i.e. the axis perpendicular to the alignment of the jaws) is the most narrow: this means that the impacts on the jaws are distributed over a smaller area on this axis, leading to a higher energy deposition. The choice is based only on the non-cleaning plane, since on the cleaning plane the distribution is dominated by multi-turn effects, such that the pattern of the energy deposition does not reflect the original shape of the beam distribution on that plane or its dimension. The selection is made on the value of the β function, the Twiss parameter which is directly linked to the rms spread of the beam on the corresponding axis via eq. 2.4. This has been done using the machine optics for operations at 6.5 TeV, leading to the choice of TCTPV.4L2.B1 as the reference collimator (the values of the 2016 injection optics functions at this collimator used for the simulations are reported in tab. 4.2). This particular TCT is located in IP2 (where the ALICE experiment is) on the pipe housing Beam 1.
On the one hand the relative position of the BLM with respect to the jaw significantly affects the BLM signal. On the other hand, the impact distribution can affect the BLM signal, especially if important asymmetries come into play; but most importantly, the impact distribution affects the energy deposition in the jaw. For this reason, the same conservative arguments must be repeated for the impact distribution, choosing the one leading to the highest energy deposition with the smallest BLM signal. Three scenarios have been proposed and discussed:

- Both jaws are inserted in the beam line with 5 σ aperture and the collimator is tilted by 59.4 μrad on the cleaning plane in order to follow the closed orbit of the beam;

	x **(non-cleaning plane)**	y **(cleaning plane)**
β **[m]**	48.156	46.504
α	-0.415	0.513
D **[m]**	-0.105	-0.078
D'	$1.546 \cdot 10^{-3}$	$0.302 \cdot 10^{-3}$
z_{CO} **[mm]**	$0.0627 \cdot 10^{-3}$	$-1.220 \cdot 10^{-3}$
z'_{CO} **[μrad]**	49	-59

Table 4.2: Values of the β function, dispersion D, offset of the closed orbit z and their derivatives at TCTPV.4L2.B1 for both planes as read from the *twiss file* for the 2016 injection optics.

- The upper jaw is set 20 mm out of the beam line, while the lower jaw is initially set at 5.4 σ and moves towards the beam during the simulation;
- The lower jaw is set 20 mm out of the beam line, while the upper jaw is initially set at 5.4 σ and moves towards the beam during the simulation.

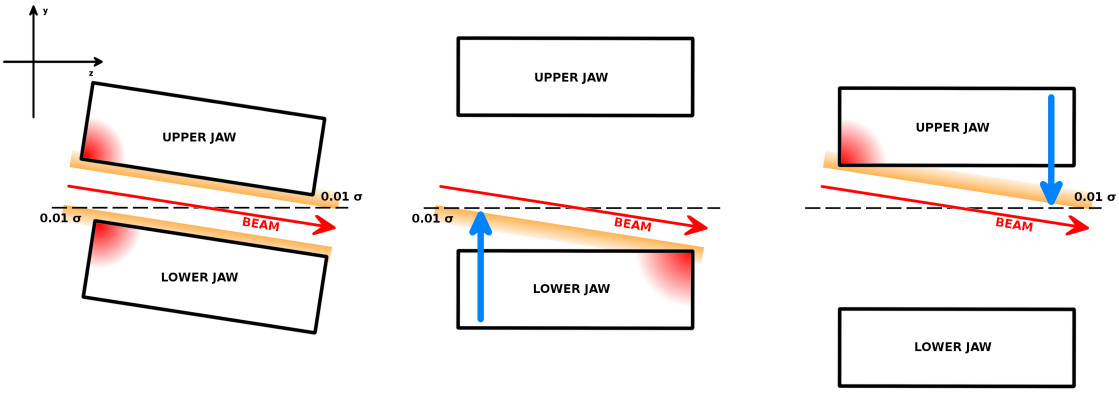

Figure 4.4: Schematic representation of the three simulation scenarios: fixed jaws with tilt angle (left frame), lower jaw moving (middle frame) and upper jaw moving (right frame). The impact area for each configuration is highlighted in red.

Neglecting orbit/optics distortions along the ring, the last two simulation setup (and results) can be used when the orbit drifts towards one of the jaws. The speed of the jaw is set at 2 mm/s [37]. To be even more conservative, the beam distribution has been chosen as flat over a 0.01 σ interval around the collimator aperture on the cleaning plane. Larger intervals correspond to less conservative situations, with lower energy deposition and higher BLM signal. Such a narrow interval also means that the impacts distribution on the jaws vary a lot between the different configurations. The three situations summarised above are represented in fig. 4.4.
SixTrack-FLUKA coupled simulations (as described in sec. 3.3) are set for these three different configurations in order to obtain the touches distribution on the collimator. These distributions are then loaded into FLUKA, in order to properly evaluate the energy deposition on the jaws. The geometry of these simulations [38] includes both the vertical TCT (i.e. the TCTPV.4L2.B1) and the horizontal TCT (i.e. the TCTPH.4L2.B1), though only

the case of the vertical TCT will be treated in this thesis, as well as a set of twelve BLMs at different coordinates. Even though a specific collimator was selected for the study, it has been decided to insert in the FLUKA geometry a series of BLMs with different longitudinal and transverse positions with a regular pattern, in order to cover as many TCTs as possible with only one simulation. The BLMs are organised on three layers, one at beam height and the other two 35 cm above or below. The same transverse and longitudinal positions are used for all the layers (see tab. 4.3). In this way, depending on which collimator is considered during the analysis, the BLM signal can be estimated by looking at the simulated BLM that most closely represents the real BLM installed at that collimator location (see tab. 4.4). Fig. 4.5 shows the mesh corresponding to the vertical TCT in the FLUKA geometry, along with the approximate position of the real BLMs installed in the LHC. A similar mesh is set up also for the horizontal collimator included in the geometry. The 12 BLMs of each meshes are identified by their label, reported in fig. 4.6.

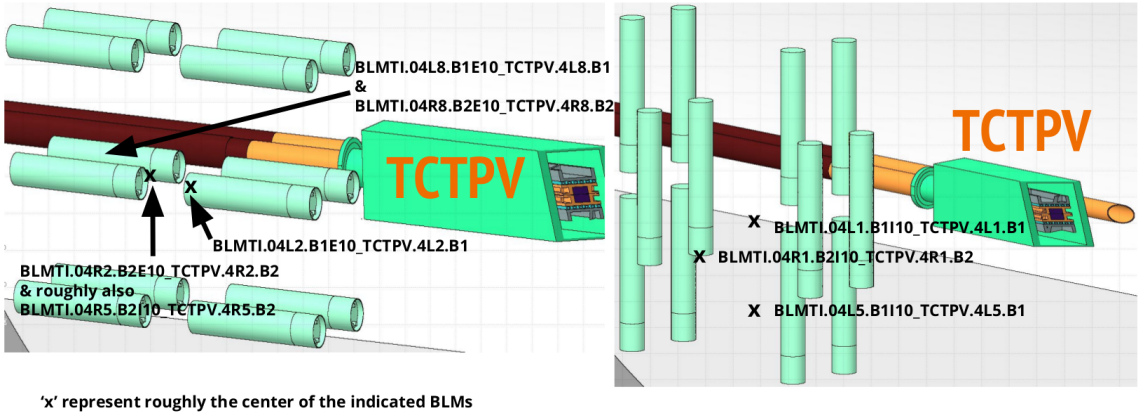

Figure 4.5: 3D representation of the FLUKA geometry for a TCT and the mesh of BLMs. The black crosses approximately show the relative position of each real BLM installed in the machine with respect to the corresponding collimator, allowing to choose the simulated BLM that best reproduces the real situation for each case [39].

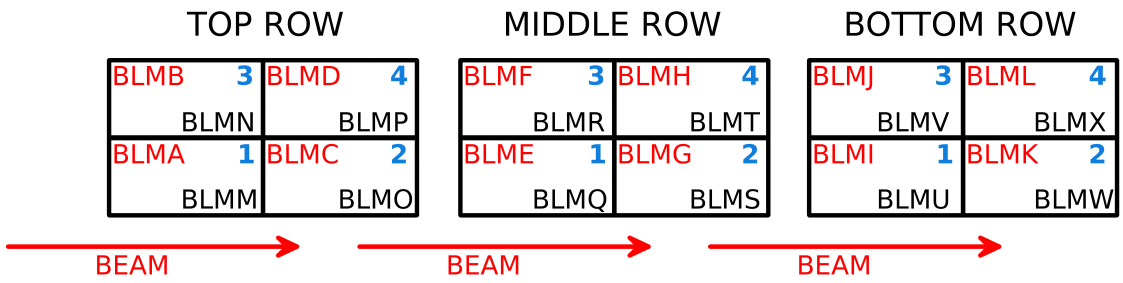

Figure 4.6: Schematic representation of the three layers of the BLM mesh. The BLM labels are reported for both the horizontal (in black) and vertical collimator (in red). In this work a specific position will be referenced independently of the row using the numbers shown in blue.

Simulations are run for all three cases initially considering a 7 TeV beam; each is executed twice, one with horizontal BLMs and one with vertical BLMs. Depending on the BLM signal of interest and on the relative orientation of BLM and collimator, the results describe different TCTs. As shown by the ratio of the BLM response and the maximum energy

deposition reported in tab. 4.5, the configuration yielding to the most conservative results is the one with the lower jaw moving towards the beam. Therefore, this is the configuration that has been chosen to study the dependence with beam energy.

BLM label		**Distance from collimator**		
TCTPV	**TCTPH**	**s [m]**	**x [m]**	**y [m]**
BLMA	BLMM	0.91	0.25	0.35
BLMB	BLMN	0.91	0.51	0.35
BLMC	BLMO	1.74	0.25	0.35
BLMD	BLMP	1.74	0.51	0.35
BLME	BLMQ	0.91	0.25	0.00
BLMF	BLMR	0.91	0.51	0.00
BLMG	BLMS	1.74	0.25	0.00
BLMH	BLMT	1.74	0.51	0.00
BLMI	BLMU	0.91	0.25	-0.35
BLMJ	BLMV	0.91	0.51	-0.35
BLMK	BLMW	1.74	0.25	-0.35
BLML	BLMX	1.74	0.51	-0.35

Table 4.3: Coordinates of the simulated BLMs in the FLUKA geometry with respect to the centre of the collimator.

Collimator	**BLM coordinates**			**Orientation**	**Closest simulated BLM**
	s [m]	**x [m]**	**y [m]**		
TCTPH.4L1.B1	0.7318	0.25	-0.2	vertical	BLMW
TCTPH.4R1.B2	-1.265	0.28	-0.14	vertical	BLMQ
TCTPV.4L1.B1	1.3218	0.25	-0.19	vertical	BLMI
TCTPV.4R1.B2	-1.385	0.24	-0.2	vertical	BLML
TCTPH.4L2.B1	0.9996	-0.51	0.0	vertical	BLMR
TCTPH.4R1.B2	-1.0404	-0.45	-0.35	horizontal	BLMV
TCTPV.4L2.B1	0.9996	-0.45	0.0	horizontal	BLMF
TCTPV.4R2.B2	-1.48	-0.37	0.0	horizontal	BLMG
TCTPH.4L5.B1	0.7534	0.3105	0.0	vertical	BLMQ
TCTPH.4R5.B2	-1.18	0.2705	-0.31	vertical	BLMU
TCTPV.4L5.B1	1.246	0.3101	-0.39	vertical	BLMI
TCTPV.4R5.B2	-1.246	0.3602	-0.36	horizontal	BLMI
TCTPH.4L8.B1	0.9092	-0.48	0.0	horizontal	BLMR
TCTPH.4R8.B2	-1.0458	-0.51	0.0	horizontal	BLMR
TCTPV.4L8.B1	1.74	-0.25	0.0	horizontal	BLMG
TCTPV.4R8.B2	-1.74	-0.27	0.0	horizontal	BLMG

Table 4.4: Coordinates of the simulated BLMs in the FLUKA geometry with respect to the centre of the collimator.

Collimator name	Simulated BLM label	Fixed Jaws		Lower Jaw Moving		Upper Jaw Moving	
		Ratio $[\frac{pGy}{GeV/cm^3}]$	% Error	Ratio $[\frac{pGy}{GeV/cm^3}]$	% Error	Ratio $[\frac{pGy}{GeV/cm^3}]$	% Error
TCTPV.4L2.B1	BLMF H	$4.12 \cdot 10^{-3}$	3.86	$0.88 \cdot 10^{-3}$	3.64	$1.75 \cdot 10^{-3}$	3.61
TCTPV.4R2.B2	BLMG H	$3.35 \cdot 10^{-3}$	3.87	$8.20 \cdot 10^{-3}$	3.56	$5.13 \cdot 10^{-3}$	3.59
TCTPV.4R5.B2	BLMI H	$2.62 \cdot 10^{-3}$	3.86	$1.11 \cdot 10^{-3}$	3.59	$1.72 \cdot 10^{-3}$	3.64
TCTPV.4L8.B1	BLMG H	$3.35 \cdot 10^{-3}$	3.87	$8.20 \cdot 10^{-3}$	3.56	$5.13 \cdot 10^{-3}$	3.59
TCTPV.4R8.B2	BLMG H	$3.35 \cdot 10^{-3}$	3.87	$8.20 \cdot 10^{-3}$	3.56	$5.13 \cdot 10^{-3}$	3.59
TCTPV.4L1.B1	BLMI V	$2.78 \cdot 10^{-3}$	7.01	$1.06 \cdot 10^{-3}$	2.43	$1.94 \cdot 10^{-3}$	2.74
TCTPV.4R1.B2	BLML V	$1.22 \cdot 10^{-3}$	7.11	$1.23 \cdot 10^{-3}$	2.39	$1.60 \cdot 10^{-3}$	2.74
TCTPV.4L5.B1	BLMI V	$2.78 \cdot 10^{-3}$	7.01	$1.06 \cdot 10^{-3}$	2.43	$1.94 \cdot 10^{-3}$	2.74

Table 4.5: Ratio between the BLM response and the maximum energy deposition on the collimator jaw obtained from FLUKA simulations in different configurations. The worst case scenario (highlighted in red) corresponds to the collimator labelled as TCTPV.4L2.B1 with the lower jaw moving towards the beam centre.

Simulations are run for all three cases initially considering a 7 TeV beam; each is executed twice, one with horizontal BLMs and one with vertical BLMs. Depending on the BLM signal of interest and on the relative orientation of BLM and collimator, the results describe different TCTs. As shown by the ratio of the BLM response and the maximum energy deposition reported in tab. 4.5, the configuration yielding to the most conservative results is the one with the lower jaw moving towards the beam. Therefore, this is the configuration that has been chosen to study the dependence with beam energy.

4.3 Energy sweep

As described in sec. 1.4, BLMs have 32 different sets of thresholds corresponding to 32 different values of beam energy: in order to review these thresholds the dependence of the BLM response on beam energy needs to be reconstructed. For this purpose, it was decided to run 5 sets of simulations, corresponding to five different values of beam energy: 450 GeV, 3.5 TeV, 5 TeV, 6.5 TeV and 7 TeV. The first and last but one values correspond to the flat bottom and flat top values at the time of writing respectively. 7 TeV is the flat top energy of the Nominal LHC, and it is the value used to select the most conservative configuration. The other values have been chosen as middle points.
The 2016 injection optics functions have been used for the simulations at all the selected beam energies. Being the first point of the ramp and squeeze phase of the LHC cycle, the $\beta^\star$ has its maximum value with its optics. Hence, β function and the beam spot size at the TCTs are minimised, i.e. the concentration of deposited energy by the impact of the beam with the jaws is maximised. In order for the study to be as independent from the optics as possible, the simulations for all the selected beam energies use the 2016 optics at injection.

4.3.1 Simulation results

The simulation setup is the same as the one described in sec. 4.2, i.e. the positive jaw is set at 20 mm, while the negative jaw is moved towards the beam at a speed of 2 mm/s starting from an opening of 5.4 σ. The only exception is the case at 450 GeV, since at this low energy the beam σ is quite large (about 1.45 mm) and starting the simulation at 5.4 σ would require too many turns before the jaw actually starts intercepting the beam. For this reason, in this particular case the initial position of the jaw is set at 5.2 σ instead.
A post-processing script rearranges the touches maps obtained with cleaning simulations, fixing the jaw aperture at 5 σ and changing the touches coordinate on the cleaning plane in order to conserve the relative distance with respect to the jaw edge. This is done in order to

have a simple setup for the simulations of energy deposition, where the jaw is kept at a fixed opening. The post-processed distributions for different beam energies are shown in fig. 4.7. On the longitudinal plane, touches concentrated towards the end of the jaw are dominated by first impacts, i.e. protons hit the jaw for the first time in this area, whereas the rest is due to protons hitting the jaw in subsequent turns. The high peak at the beginning of the distribution represents impacts on the front face. The peak on the cleaning plane is due to protons hitting the jaw on the first turn, hence touches are concentrated on the jaw surface; all the rest of the distribution is due to multi-turn effects.

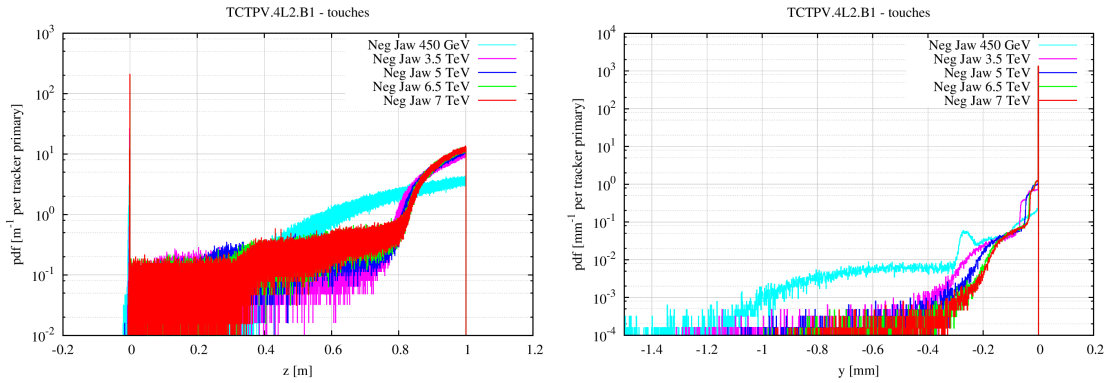

Figure 4.7: Touches distribution on the negative jaw for different beam energy values on the longitudinal axis (left frame) and on the cleaning plane (right frame).

The corresponding FLUKA simulations follow the same procedure previously described. As shown in fig. 4.4, in this configuration the beam impacts on the lower jaw only and the angle of the closed orbit is such that the touches are concentrated towards the end of the jaw. Fig. 4.8 shows the longitudinal profile of the peak energy deposition for the different beam energies. The energy deposition is concentrated mainly towards the end of the jaw, reflecting the way protons hit the collimator jaw, and it increases with beam energy. The reported results are the data collected using the finest of the meshes prepared in the FLUKA input file (see sec. 4.1.2), as it is the best one to resolve the peak.

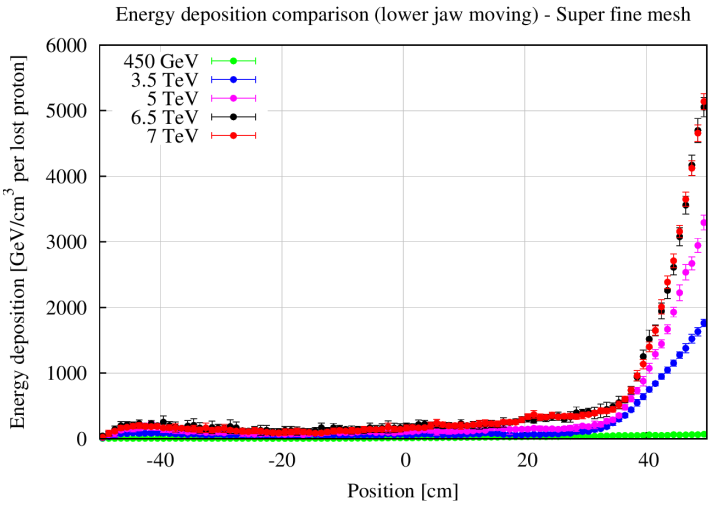

Figure 4.8: Longitudinal profile of the peak energy deposition on the lower jaws obtained with FLUKA simulations for different beam energies.

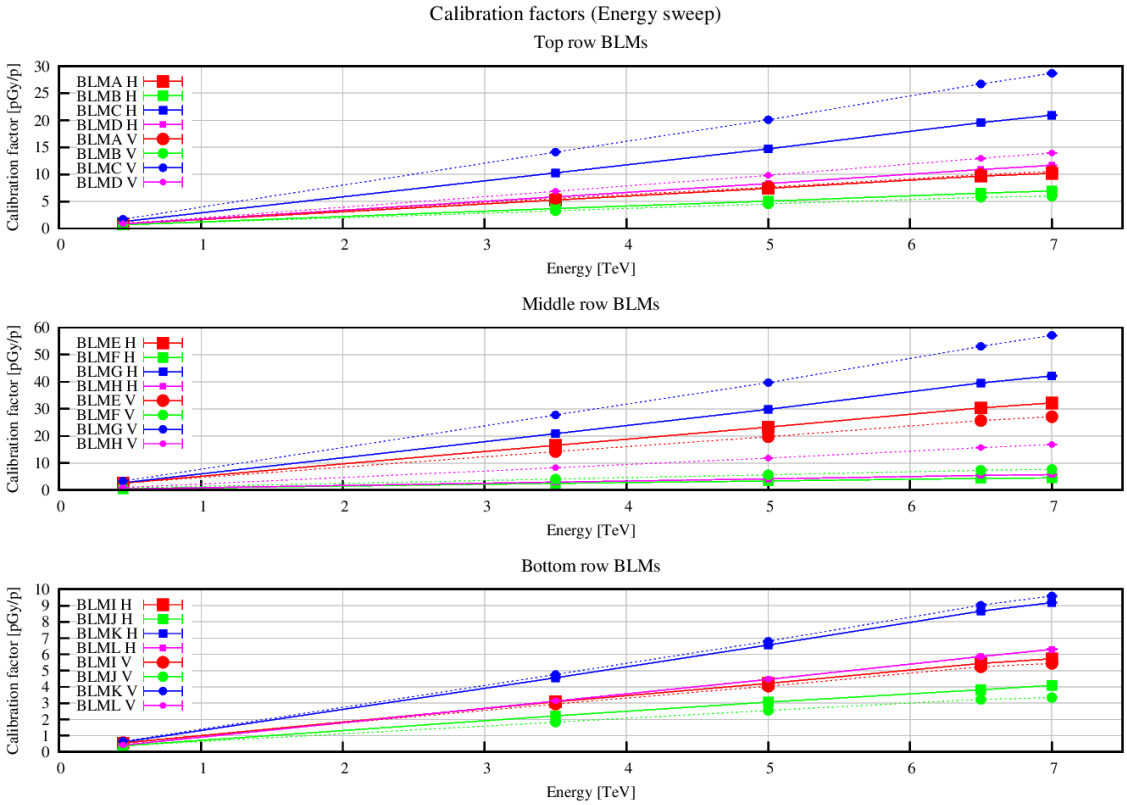

Figure 4.9: Simulated signal for each BLM in the vertical collimator mesh as function of the beam energy. The values for BLMs in vertical (dashed line) and horizontal (solid line) orientation are reported.

Fig. 4.9 reports the simulated signal for each BLM in the mesh, both in vertical and horizontal orientation, as function of beam energy. The following remarks can be made:

- the BLMs on the bottom row show the lowest values, whereas those in the middle register the highest values;
- for most of the positions in the mesh, the vertical BLMs show a higher response than that at the horizontal BLMs;
- all BLMs show a linear dependence of the calibration factor on beam energy.

The closest BLM to the one installed near the TCTPV.4L2.B1 is the one labelled as BLMF horizontally oriented. This BLM, located in the middle row of the mesh, is in the farthest position from the pipe on the transverse plane and in the closest position with respect to the collimator on the longitudinal direction (see fig. 4.6 and tab. 4.3). The calibration factor for the different energy values are reported in tab. 4.6 and plotted in fig. 4.10.

4.3.2 Benchmark against measurements

Due to constraints in the schedule of the LHC operation in 2017, it has not been possible to measure the BLM response of the collimator chosen for the simulations. However, during the period of the initial commissioning of the LHC with beam in spring 2017 (namely during the morning of 24$^{\text{th}}$ May 2017), qualification loss maps were taken during the ramp; these were a good opportunity to collect and analyse measurements of the BLM response at the TCPs as

Beam energy [TeV]	Simulated CF [pGy per lost proton]	% Error
0.45	0.5101	1.55
3.5	2.513	0.99
5	3.420	0.78
6.5	4.379	1.03
7	4.533	0.92

Table 4.6: BLM calibration factors obtained with FLUKA simulations for TCTPV.4L2.B1 at different beam energy values.

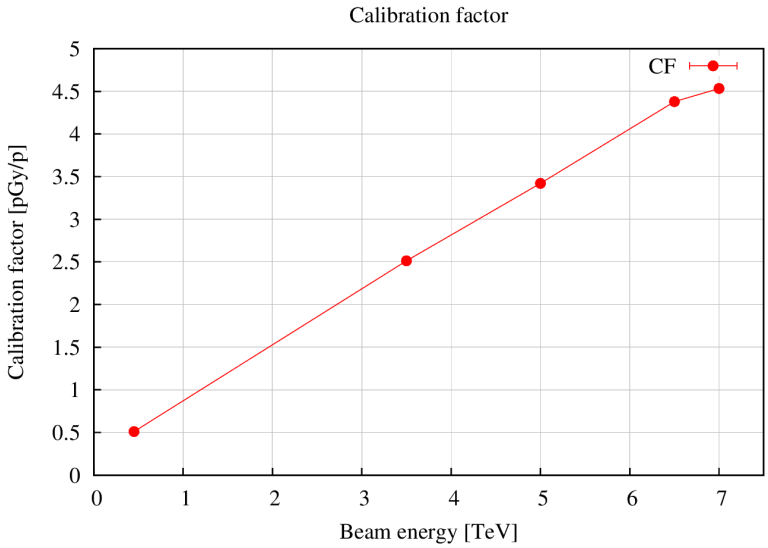

Figure 4.10: BLM calibration factors obtained with FLUKA simulations for TCTPV.4L2.B1 at different beam energy values.

a function of the beam energy. A qualification loss map is a procedure during which a bunch is artificially excited to increase the betatron amplitude of the beam particles along a certain axis, creating abnormal loss rates in order to measure their pattern and verify the efficiency of the collimation system. These measurements can be used for a qualitative benchmark (i.e. for checking the goodness of the functional dependence rather than of the absolute values) of the BLM response as computed from simulations. In a loss map, the collimation system is set at its nominal opening, with the TCPs being the aperture bottleneck, as the TCT in the considered cases. Coupled with other loss maps at injection (performed on 22nd May 2017), it was possible to reconstruct the energy dependence of the calibration factor for these collimators, on both horizontal and vertical planes and for both Beam 1 and Beam 2. These measurements cannot be quantitatively compared to the simulations discussed so far, since they refer to collimators placed in different locations along the ring with different settings and, most importantly, made of different materials. This substantially impacts the development of secondary particle showers, and hence the BLM signal, since the tungsten TCTs absorb much more than the carbon fibre TCPs). However, normalising the results to the value at 6.5 TeV (which is the present flat top energy for LHC) it is possible to compare the behaviour of the BLM response and have an idea of the accuracy and reliability of the simulation results.
In order to measure the BLM response to losses on a collimator, the collimator of interest

must be set as the primary bottleneck (i.e. it is set at the smallest normalised aperture in the machine). A blow up of the beam (usually to a pilot bunch) is performed. In this way, the emittance of the bunch is increased, since the oscillation of the particles on the cleaning plane becomes larger, and the bunch is lost on the desired collimator. The bunch loss is shown by the decrease of the beam intensity measured with the Beam Current Transformer (BCT) in "number of charges" (i.e. number of protons, since the beam particles of the LHC beams considered for the measurements are protons and they have unitary charge).
Losses on the collimator generate secondary particle showers that ionise the N_2 gas contained in the BLM ionisation chambers. Electrons and ions are collected, generating a signal that is then integrated over the various time windows presented in tab. 1.1, allowing to estimate the dose deposited in the gas active region of the detector in Gy/s for each running sum. These signals, proportional to the amount of beam loss, can be correlated with the variation registered by the BCT in the corresponding time window. The BLM response factor is obtained via the following equation:

$$\mathrm{CF} = \frac{S_{\mathrm{BLM}}}{\Delta S_{\mathrm{BCT}}} \cdot \Delta T_{\mathrm{RS}} \tag{4.1}$$

where S_{BLM} is the BLM readout for a given RS at a given time, ΔS_{BCT} is the variation of the BCT readout in the time window corresponding to the considered running sum and ending at the time of the BLM readout and ΔT_{RS} is the duration of the time window corresponding to the running sum. This returns a quantity measured in Gy per lost proton as expected. Since the collimator of interest has been set as primary bottleneck, the measured calibration factor represents the BLM response to a direct loss on the collimator.

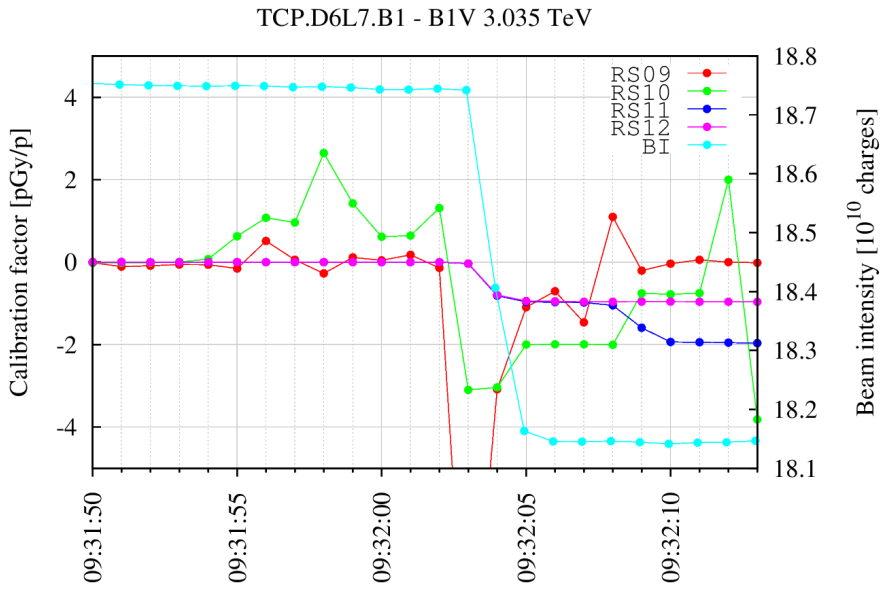

Figure 4.11: Example calibration factor calculated with different running sums for TCP.D6L7.B1 (measurements taken on the 24$^{\mathrm{th}}$ May 2017) during a beam excitation along the cleaning plane at $E_{beam} = 3$ TeV. The beam intensity detected by the BCT (in light blue, right vertical axis) is also shown.

The longer the integration time, the more accurate is the estimation. Indeed, the main cause of uncertainty in the calculation of the calibration factor is the BCT signal. The

value of ΔS_{BCT} calculated between two points in time close to each other is not large, and it is susceptible to oscillations on the signal. On the contrary, the drop down in beam current seen between two points far away from each other in time is way larger for a long excitation, and oscillations of the BCT signal tend to even out, producing more stable results for the calibration factor. Hence, long running sums are more suitable for this kind of analysis. Fig. 4.11 shows an example of the calibration factor of the BLM at TCP.D6L7.B1 reconstructed from running sums from RS09 to RS12. Results coming from shorter running sums show considerable variations depending on the considered timestamp, while as the time window become larger the calibration factor seems to become more stable. For this reason, the analysis performed in this work will make use only of the longest possible running sum, that is to say RS12 (83.8 s).
Before the calculation of the calibration factor, BLM readouts are corrected by subtracting a background value. If the beam excitations are well separated in time between each other, the background is estimated as the mean signal in a time window where the blow up has yet to be applied to the beam. This can be done if the time separation between two subsequent excitation is of the order of RS12 or larger, so that the integration window does not contain signals from the first blow up when the second one starts. On the other hand, if the time separation is shorter, the first excitation has not completely exited the integration window yet when the second one starts. This means that the BLM readouts in this situation contains contributions from two different blow ups. To avoid this pile-up and correctly estimate the BLM response, in this case the background is estimated as the mean signal produced by the previous excitation.

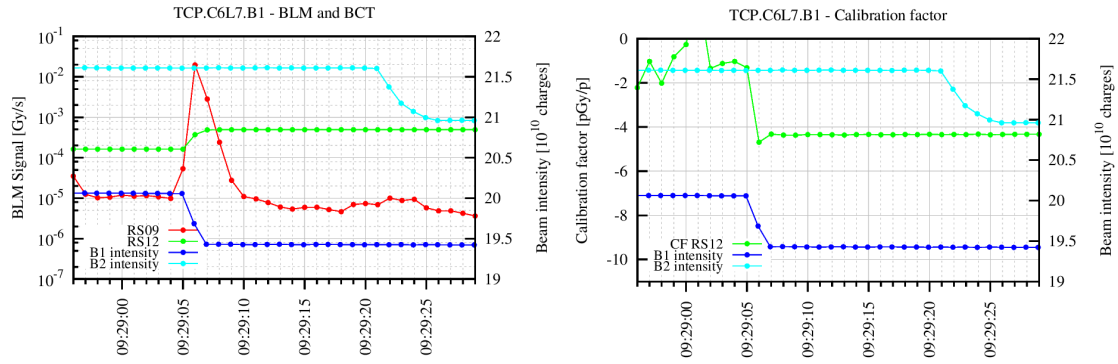

Figure 4.12: Example of data analysis for the BLM signals at the TCP.C6L7.B1 with a beam energy of 2 TeV. The plot on the left frame shows the raw data coming from RS09 (normally used for qualification loss maps), RS12 and BCT. The plot on the right frame shows the measured calibration factor.

An example of the analysis performed on the measurements at the TCPs can be seen in fig. 4.12.
The energy dependence of the BLM response has been measured for the TCP.C6L7.B1, TCP.C6R7.B2, TCP.D6L7.B1 and TCP.D6R7.B2, the first two being the horizontal primary collimators, hence they are the ones that perform cleaning on the horizontal planes, while the last two are the primary collimators on the vertical plane, and perform cleaning accordingly. The results for the two couples of collimators are shown in fig. 4.13. It can be seen that in most cases the energy dependence shows a somewhat logarithmic behaviour, except for the measurements of Beam 2 on the horizontal plane. In this case the BLM response shows a peak at $E_{beam} \simeq 4$ TeV and then becomes smaller again at higher energy. This odd behaviour does not have a clear explanation, but it can be due to changes in the angle

between the closed orbit and the primary collimators, with a possible interplay between the horizontal and the skew collimator, immediately downstream. Moreover, normally when the beam is excited on a certain plane for loss maps, the BCT signal shows a steep decrease in intensity due to the fact that the beam particles are rapidly lost in the machine aperture. However, this is not the case for excitations of Beam 2 on the horizontal axis during the aforementioned measurements. Instead, the intensity decrease is slower and less regular, meaning that something in the beam condition could have been deviating from normal.

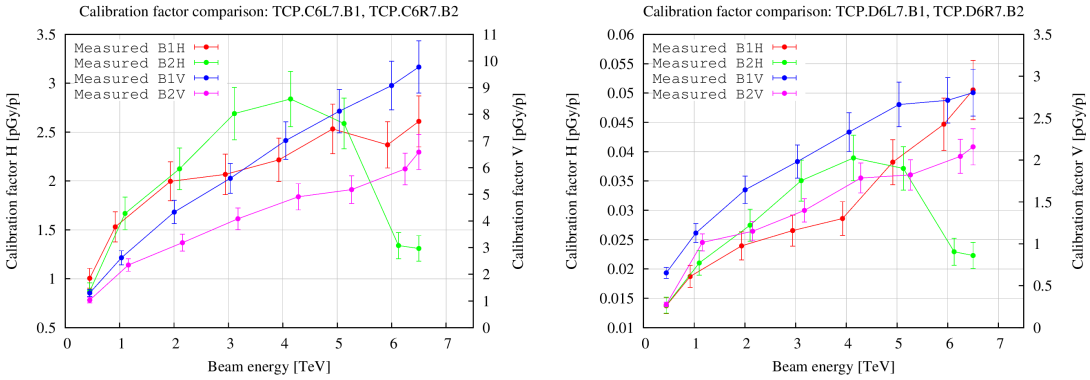

Figure 4.13: BLM response at horizontal (left frame) and vertical (right frame) TCPs obtained during qualification loss maps.

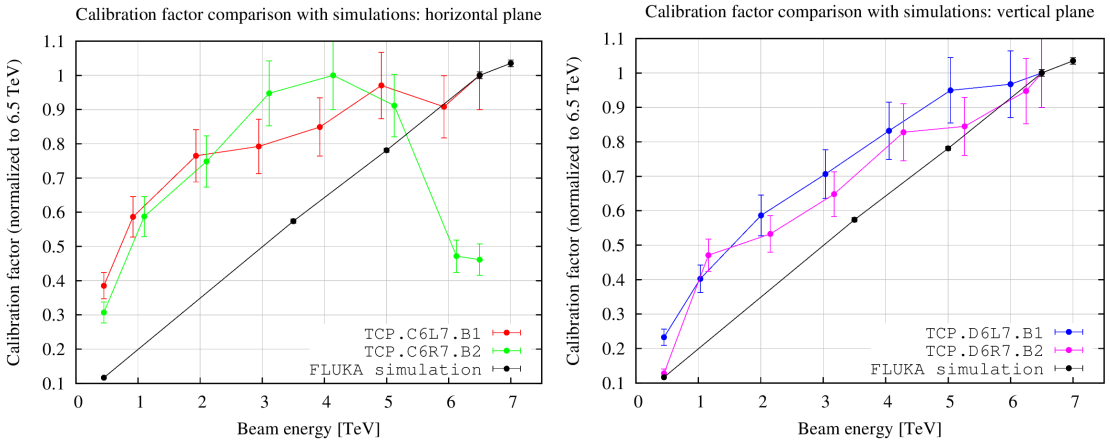

Figure 4.14: Comparison between the BLM response obtained with simulations and one obtained at horizontal (left frame) and vertical (right frame) TCPs during qualification loss maps. The results are normalised to the values corresponding to $E_{beam} = 6.5$ TeV.

A comparison between the BLM response as from simulations and the measured ones is shown in fig. 4.14. An overall good agreement is visible, even though the simulation results show a behaviour closer to a linear dependence on beam energy rather than to a logarithmic one like the measurements show. However, given the different composition of the TCTs and TCPs and since discrepancies of the order of 30% are acceptable for this kind of benchmarks [40, 41], this comparison gives a good indication of the reliability of the simulations.

4.4 BLM thresholds review

Simulation results presented in this thesis can be used to determine which are the levels of energy and power deposition in the jaws of the TCTs collimators allowed by the BLM thresholds presently deployed, in case of an accidental movement of a jaw towards the beam or a distortion in the closed orbit resulting in a drift of the beam towards the jaw. In fact, knowing the response of a BLM of interest to an impacting proton, it is possible to reconstruct the number of impacting protons allowed by that thresholds, and, thanks to the energy deposition map estimated with FLUKA, reconstruct the actual energy deposition.
As described in sec. 1.4, BLMs are grouped into four families, each with the same master table, i.e. the tabulation of BLM thresholds corresponding to the condition of highest allowed stresses on the collimator jaws for 32 energy levels running from 0 to over 7 TeV. In particular, 450 GeV corresponds to EL2, 3.5 TeV to EL15, 5 TeV to EL21, 6.5 TeV to EL27 and 7 TeV to EL29 [42]. Fig. 4.15 reports the present master thresholds for each BLM family and each of the simulated energy levels. During operation, the *applied thresholds* are actually used by the BLM system; these are obtained by multiplying the master thresholds to a *monitor factor*, which in principle can be different for each BLM.
Tab. 4.7 shows the monitor factors for each BLM. The BLM for the collimator used in the simulations is part of the THRI_TCTVA. However, since the configuration simulated for the study presented in this work is conservative in terms of impacts distribution and energy deposition, it is possible to use the same results to review the thresholds for all the different BLM families.
Knowing the BLM response factor at different energy levels (see fig. 4.9), the number of protons lost on the collimator jaw can be reconstructed via the following formula:

$$\mathrm{N}_p = \frac{D^{Th}_{\mathrm{BLM}} \cdot \Delta T_{\mathrm{RS}}}{\mathrm{CF}} \tag{4.2}$$

where D^{Th}_{BLM} is the BLM thresholds expressed in Gy/s at the chosen energy level, ΔT_{RS} is the time width of the corresponding running sum and CF is the simulated calibration factor at that energy level. The amount of allowed lost protons is the most significant quantity only for short time intervals, hence running sums, since in such a time domain the thermo-mechanical response of the material is energy-driven, and not power-driven. However, for longer running sums the loss rate becomes important since the thermo-mechanical behaviour of the material is power-driven, hence, the proton loss rate is the relevant observable, and it can be calculated in terms of p/s via the following formula:

$$\mathrm{R}_p = \frac{D^{Th}_{\mathrm{BLM}}}{\mathrm{CF}} \tag{4.3}$$

which is basically the same as eq. 4.2 but without the multiplication by the time width of the running sum. Using the master table, the values obtained with eq. 4.2 and 4.3 must be multiplied by the monitor factor of each specific BLM. In order to get the highest energy deposition allowed by the present BLM thresholds, the BLM with the lowest response among the simulated BLMs that best describe the real ones installed at the location of collimators sharing the same family, monitor factor and cleaning plane is used to calculate the maximum number of protons and the proton loss rate allowed by the thresholds, $N_{p,max}$ and $R_{p,max}$.
Finally, the energy deposition and power loss per cm^3 along the jaw can be obtained by multiplying the profile obtained with the simulations by $\mathrm{N}_{p,max}$ and $\mathrm{R}_{p,max}$ respectively. As already discussed, the energy deposition per unit volume is the most significant quantity when defining thresholds for short time scales, and hence running sums up to approximately RS09 (i.e. $\sim$ 1 s). For these time windows it is safe to assume that a given number of

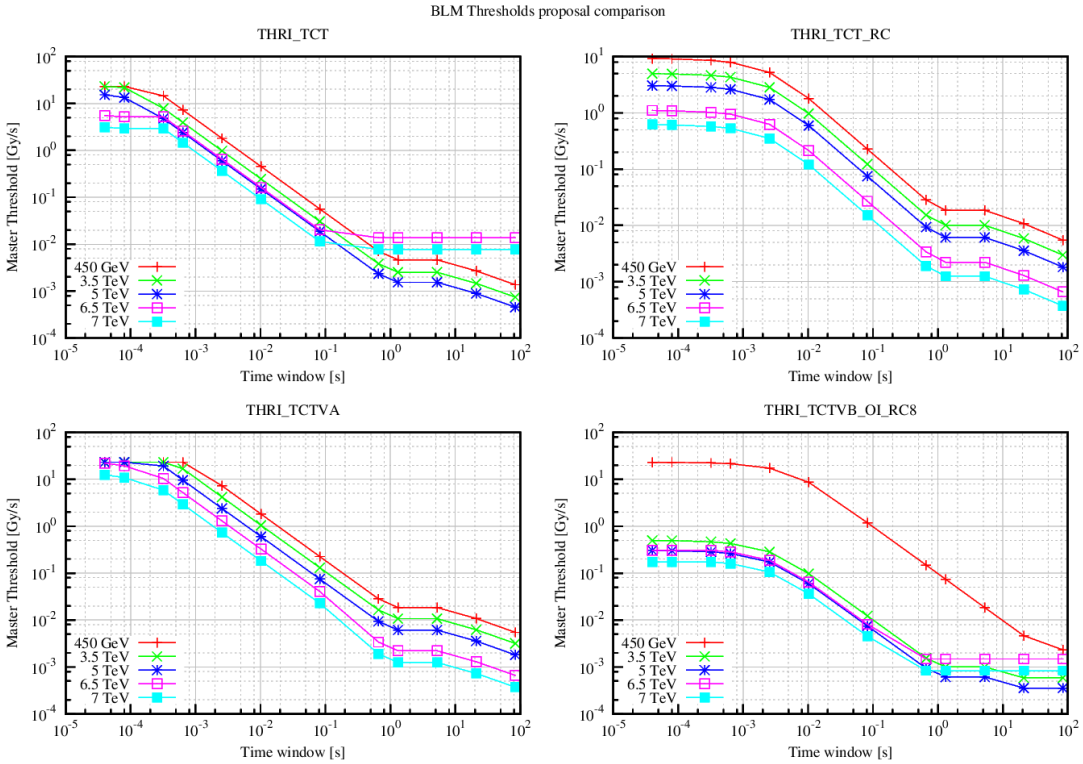

Figure 4.15: Present master thresholds for each running sum for the four TCT families. The values for the simulated energy levels are reported. The thresholds were provided by the BLM Threshold Working Group.

Family name	BLM name	Monitor factor
THRI_TCT	BLMTI.04L1.B1I10_TCTPH.4L1.B1	0.4
	BLMTI.04L1.B1I10_TCTPV.4L1.B1	0.4
	BLMTI.04L5.B1I10_TCTPH.4L5.B1	0.4
	BLMTI.04L5.B1I10_TCTPV.4L5.B1	0.4
	BLMTI.04L8.B1E10_TCTPH.4L8.B1	0.8
	BLMTI.04L8.B1E10_TCTPV.4L8.B1	0.8
	BLMTI.04R1.B2I10_TCTPH.4R1.B2	0.4
	BLMTI.04R1.B2I10_TCTPV.4R1.B2	0.4
	BLMTI.04R5.B2I10_TCTPH.4R5.B2	0.4
	BLMTI.04R5.B2I10_TCTPV.4R5.B2	0.4
THRI_TCTVA	BLMTI.04L2.B1E10_TCTPH.4L2.B1	0.5
	BLMTI.04L2.B1E10_TCTPV.4L2.B1	0.5
	BLMTI.04R2.B2E10_TCTPH.4R2.B2	0.3
	BLMTI.04R2.B2E10_TCTPV.4R2.B2	0.2
THRI_TCT_RC	BLMTI.04R8.B2E10_TCTPH.4R8.B2	0.5
THRI_TCTVB_OI_RC8	BLMTI.04R8.B2E10_TCTPV.4R8.B2	1.0

Table 4.7: Monitor factors for each BLM.

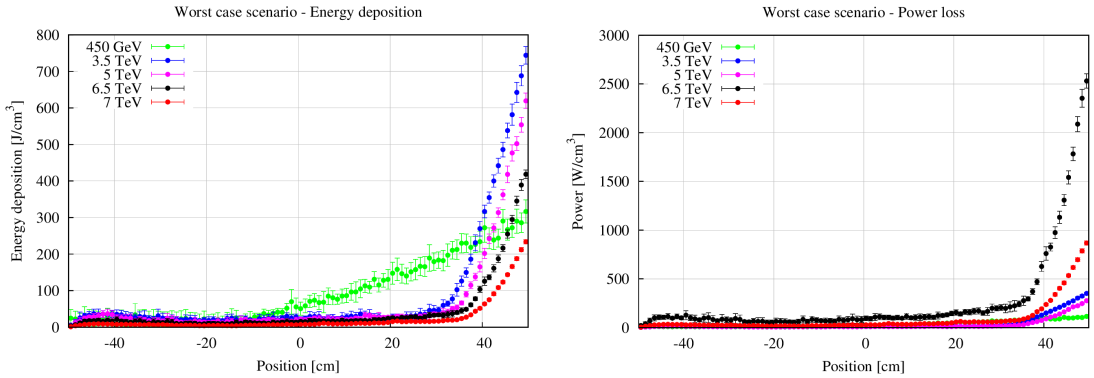

Figure 4.16: Highest energy deposition (left frame) and power loss (right frame) profiles allowed by the present BLM thresholds for the simulated scenario for each beam energy value.

impacting protons causes the same damage regardless of the duration of the loss. From RS10 onwards the time windows are long enough for energy transfer mechanisms in the impacted material to become dominant, and what matters is the rate of energy deposition. For this reason, thresholds for longer running sums rely on power loss instead. Fig. 4.16 reports the energy deposition profile obtained with FLUKA simulations in J/cm^3 and W/cm^3. For each energy, the highest number of protons and loss rate among all BLM families at each energy has been used for the conversion, in a conservative approach.

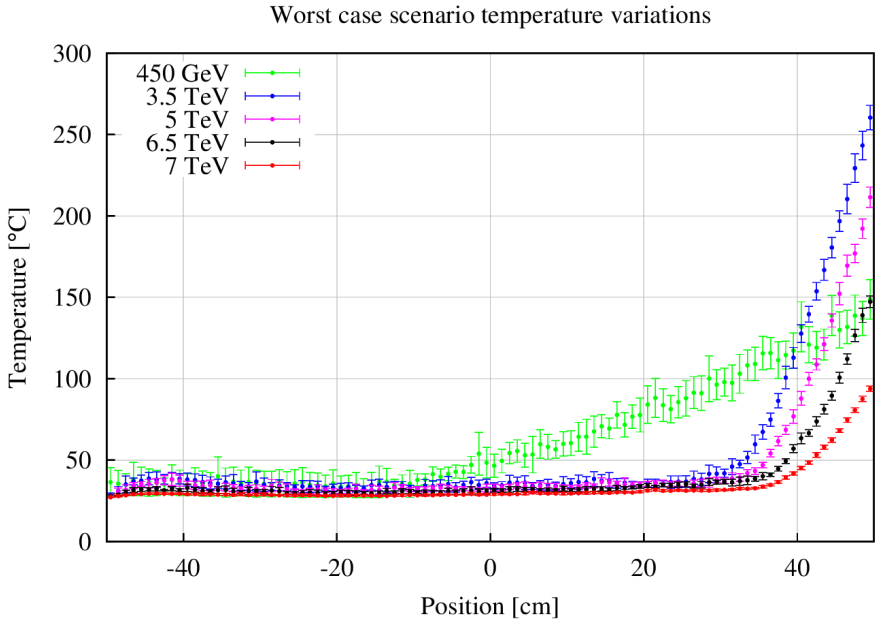

Figure 4.17: Maximum temperature variation in the collimator jaw allowed by the present BLM thresholds for each beam energy value.

The energy deposition per unit volume can be converted into a temperature increase from room temperature using the tungsten specific heat [43] and the maximum number of impacting protons allowed by the current thresholds. The results are shown in fig. 4.17. This is done under the assumption that the energy deposition caused by the impact of the protons on the collimator jaw is so fast that energy transfer mechanisms inside the jaw material can

be neglected. For longer time windows energy transfer mechanisms are not longer negligible. Their effect reduces the effective temperature reached by the jaw. For this reason the temperatures shown in fig. 4.17 can be considered as an overestimation, which is coherent with the conservative approach carried out in this work. These temperatures are not worrying since they are comparable to the temperature of bake-out, though gradients are higher than during the bake-out process [44], leaving room for an improvement of the BLM thresholds for running sums up to RS09.
On the other hand, the power loss is the most important quantity of longer time windows (i.e. from RS10 onwards), where the actual damage caused to the jaw depends on the balance between the rate of energy deposition and the energy transfer processes inside the material. For this reason, the conversion to a temperature variation is not as immediate as in the previous case. Power losses of a few kW/cm^3 like the ones shown in fig. 4.17 for high beam energies could potentially bring the jaw material close to the plastic deformation regime [44], depending on the duration of the losses, which permanently changes the shape of the jaw and therefore has to be avoided. More accurate thermo-mechanical studies, which are beyond the scope of this work, are required in order to have a more precise estimation of the thermo-mechanical response of the material to such levels of power deposition. Hence, present values of BLM thresholds are in the no-stay region, representing an upper limit, from which it is safer to take a margin.

Chapter 5

Benchmark against measurements

A complementary part of this work is to benchmark simulation results against measurements, to gain confidence. In section 4.3.2 a benchmark of the BLM response as a function of beam energy was shown. The benchmark was only qualitative, since the only measurements with beam energy available at the time of writing were for TCPs, which have jaws in graphite instead of tungsten; hence, only the functional shape could be verified, using normalised values. In this chapter, quantitative comparisons will be performed instead using dedicated measurements from 2016, obtained with a TCT as primary bottleneck.
Two separate series of benchmarks have been performed using different TCTs, depending on the operational conditions: one at 6.5 TeV (flat top energy), at the end of squeeze (see sec. 1.1.2) and one at 450 GeV (injection energy). In the following sections data analysis, simulation results and comparisons for both cases will be presented.

5.1 Benchmark at 6.5 TeV

The benchmark at 6.5 TeV has been performed using measurements taken on 10^{th} June 2016, during aperture measurements at flat top energy, at the end of squeeze [45]. The collimator used for the measurements was the TCTPH.4L5.B1, located upstream of IP5 (where collisions detected by CMS take place, see fig. 1.2).

5.1.1 Data analysis

As described in 4.3.2, the TCTPH.4L5.B1 has been set as the primary bottleneck on the cleaning plane, i.e. the horizontal one, while the beam underwent a continuous blow up in order to generate controlled losses on the concerned plane. In particular, a pilot bunch was lost on the collimator jaws during two consecutive blow ups.
The two excitations (the first one lasting between 13:59:50 and 14:01:40 and the second one between 14:01:40 and 14:04:20) have been treated independently to obtain two measurements of the calibration factor. The background value, estimated as the mean signal in the time window going from 13:50:00 to 13:54:50 (where no excitations are applied to the beam) has been subtracted to the BLM readouts. The first excitation, shown in left frame of fig. 5.1, is not extremely strong and lasts for a shorter time than the integration window of RS12, which makes the results less stable. In fact, the value of the calibration factor gets reasonably stable only after the end of the first excitation, since the intensity loss is high enough to guarantee a reliable signal only when the integration window contains the whole excitation ($\Delta S_{\text{BCT}} \sim 3 \cdot 10^8$ charges). The point immediately after the end of the excitation was taken to estimate the calibration factor. A 10% relative error, which is way larger than

the fluctuations of the signal and is typical of BLM signals [46], was arbitrarily assigned. On the other hand, the second excitation, shown in right frame of 5.1, lasts for a longer time and the beam intensity loss rate is higher, reaching several 10^8 protons lost and leading to more stable results. In this case it was decided to average the values of calibration factor obtained during the whole excitation time, in order to further stabilise the final result.

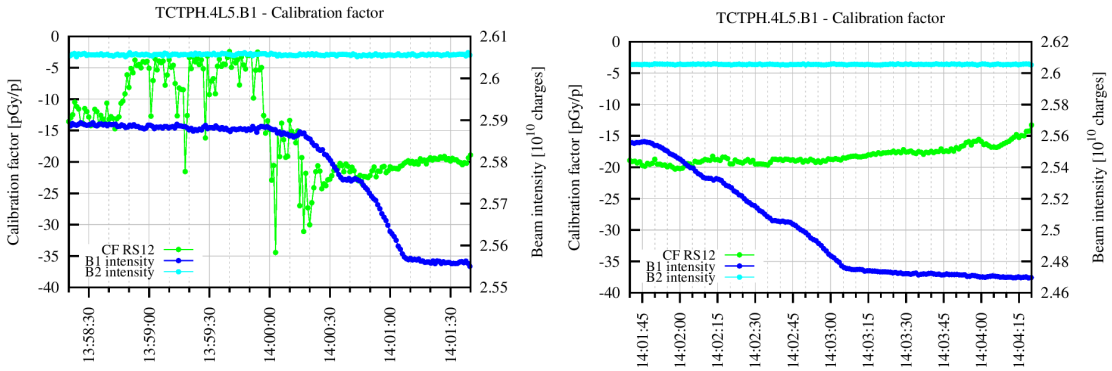

Figure 5.1: Calibration factor measurements for the TCTPH.4L5.B1 at 6.5 TeV. The BCT signal for both beams is also shown.

Timestamps	Method	Calibration Factor [pGy/p]	% Error
14:01:20.0	single value	19.32	10.0
14:01:40-14:03:00.0	mean	19.17	2.3

Table 5.1: BLM calibration factors obtained from measurements for TCTPH.4L5.B1 at 6.5 TeV.

Tab. 5.1 shows the results of the two measurements, which are compatible among each other.

5.1.2 Simulations settings

The simulation setup is basically the same as that used in chap. 4 for the energy sweep. Most of the collimators were set at very large gaps (i.e. 50 mm) during the measurements, so the FLUKA-SixTrack simulation has been set up in order to include only those with more regular gaps, reported in tab. 5.2 (note that the collimator of interest is the one with the smallest aperture on the horizontal plane, which is the cleaning plane).

Collimator	Aperture [number of σ]
TCTPH.4L5.B1	11.14
TCTPV.4L1.B1	9.95
TCP.C6L7.B1	12.74
TCP.D6L7.B1	15.41

Table 5.2: Collimator settings for the cleaning simulation at 6.5 TeV.

The simulated configuration is quite similar to the one of the simulations for the energy sweep described in chapter 4, with the closed orbit tilted towards the negative jaw and the β function making it the most impacted. The beam distributions are the same as the ones

	x **(cleaning plane)**	y **(non-cleaning plane)**
β **[m]**	2151.936	813.995
α	-2.567	-13.475
D **[m]**	-0.215	-1.071
D'	$-0.767 \cdot 10^{-3}$	$-18.044 \cdot 10^{-3}$
z_{CO} **[mm]**	-1.705	-0.123
z'_{CO} **[μrad**	-43	5

Table 5.3: Values of the β function, dispersion D, offset of the closed orbit z and their derivatives at TCTPH.4L5.B1 for both planes as read from the *twiss file* for the 2016 40 cm squeeze optics.

used in chapter 4 (i.e. Gaussian distribution on the non-cleaning plane, flat tail distribution on the cleaning plane). Tab. 5.3 reports the optics functions at the TCTPH.4L5.B1 as read from the *twiss file* (2016 squeezed optics with $\beta^\star = 40$ cm). In order to find the best fit to the data, three different simulation setups are used:

- 0.01 σ sampling on the cleaning plane, horizontal BLMs, no tilt of the collimator jaw;
- 0.01 σ sampling on the cleaning plane, vertical BLMs, no tilt of the collimator jaw;
- 0.01 σ sampling on the cleaning plane, vertical BLMs, 102.5 μrad tilt of the collimator jaw.

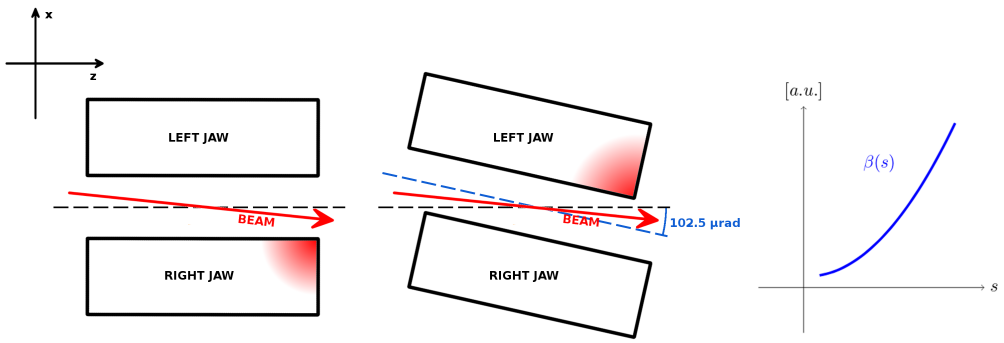

Figure 5.2: Schematic representation of the simulated configurations: with no tilt (left frame) and with a 102.5 μrad tilt (middle frame) of the collimator jaw. The right frame shows a sketch of the β function behaviour on the cleaning plane. The impacted corner for each configuration is highlighted in red.

These configurations are shown in fig. 5.2. The tails were sampled starting from the actual cut set by the jaw opening; the β function at the collimator is increasing (defocused beam), hence the far-end corner of the jaw determines the actual collimator cut. In order to be more accurate on the estimation of the BLM response, the third scenario considers the relative angle between the jaws and the closed orbit, which is generally not taken into account in cleaning simulations[1]. The angle was estimated retrieving the Beam Position Monitor

[1]In fact, in simulations for cleaning studies, all collimators are always centred around the closed orbit and tilted to follow it; hence, the relative angle is zero.

(BPM) readouts at the collimator, which give the position of the beam at the beginning and end of the collimator. The readouts revealed a 60 μrad angle, to be added to the 42.5 μrad of the closed orbit.
Regarding the FLUKA simulation, the same FLUKA geometry as the one used for the energy sweep (see sec. 4.1) was deployed, which contained also the horizontal tertiary collimator with its own mesh of BLMs. In fact, the same design of TCT is installed in the four interaction regions, and even though the portion of machine between the separation/recombination dipoles (where TCTs are located, see sec. 1.5) is different between IR2 and IR5, the relative mesh was determined looking at all the relative positions between collimator and monitor. Among the BLMs in the mesh, the one that best describes the monitor corresponding to the TCTPH.4L5.B1 is the one labelled as BLMQ in a vertical position (see tab. 4.4). This BLM, located in the middle row of the mesh (i.e. vertically aligned with the beam) is the closest to the beam on the horizontal axis and the farthest from the collimator on the longitudinal axis (see fig. 4.6 and tab. 4.3).

5.1.3 Results

Tab. 5.4 shows the simulated BLM response for the different configurations. No matter the configuration, the simulation results agree within 20-30% to measurements, a figure typical for this kind of benchmarks [40, 41], which makes the benchmark satisfactory enough. As it can be seen, there is a relevant change in the response function of the BLM when it is changed of orientation, reflecting different solid angles illuminated by the secondary particle shower. Anyway, it should be kept in mind that the BLM actually at the collimator is vertical. Taking into account the misalignment angle between closed orbit and jaws further decreases the simulated calibration factor. The BLMs located in the top and bottom rows have extremely similar response, which is consistent with the simulated scenario of losses on the cleaning plane of a horizontal collimator. The BLMs in the middle row have the highest calibration factor in all simulated configurations. Tab. 5.5 shows the ratio between the simulated BLM response and the simulated peak energy deposition. This gives an indication that the most favourable position for a BLM is the one labelled in fig. 4.6 as 2.

5.2 Benchmark at 450 GeV

For the benchmark at 450 GeV, measurements taken on 11$^{\text{th}}$ November 2016 in parallel to an MD activity about collimation with crystals[2] [48] have been used. The collimator used was the TCTPH.4R5.B2, located as the one used for the benchmark at 6.5 TeV but on Beam 2. It should be noted that the crystal collimation studies were being carried out on Beam 1; hence, these measurements had to be performed on the other beam.

5.2.1 Data analysis

The data collection was performed following the same procedure as the one used for the benchmark at 6.5 TeV, i.e. setting the collimator as primary bottleneck and blowing up the beam to induce losses. For this benchmark a wider set of measurements is available, as the excitation was applied with different collimator configurations:

[2]Crystal collimation [47] is currently under study in order to improve cleaning efficiency for future upgrades of the LHC. Bent silicon crystals are used as collimators and the potential well between the crystal planes is exploited to channel beam halo particles, bending their trajectory towards a single absorber.

	Horizontal BLMs	**Vertical BLMs**
	0.01 σ	**0.01 σ**
0 μrad	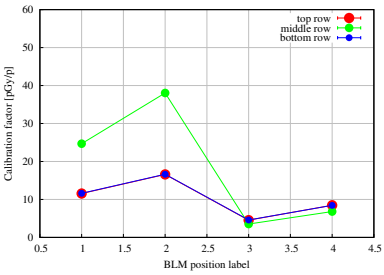	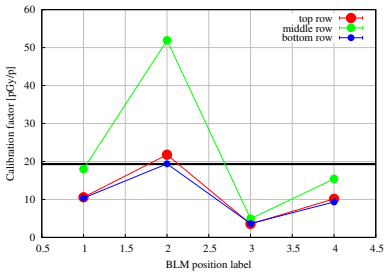
102.5 μrad		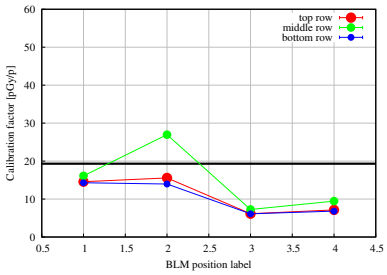

Table 5.4: Simulated signals for the three layers of the BLM mesh set up for the TCTPH.4R5.B2 at 450 GeV. The various configurations in terms of orientation of the BLMs and tilt applied to the jaws are reported. The black line represents the measured value. BLMQ is the middle row BLM with label 1.

	Horizontal BLMs	**Vertical BLMs**
	0.01 σ	**0.01 σ**
0 μrad	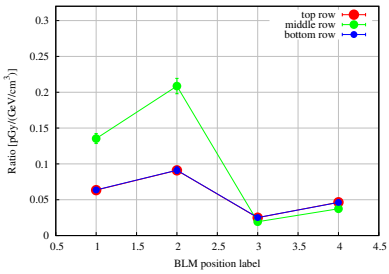	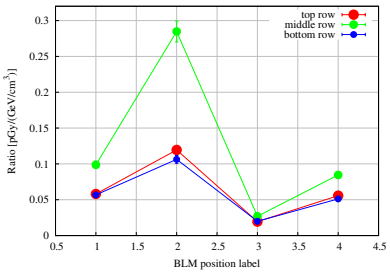
102.5 μrad		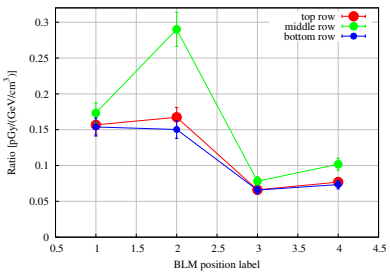

Table 5.5: Ratio between the simulated BLM response and the simulated peak energy deposition for the three layers of the BLM mesh set up for the TCTPH.4L5.B1 at 6.5 TeV. The various configurations in terms of orientation of the BLMs and tilt applied to the jaws are reported. BLMQ is the middle row BLM with label 1.

- both jaws inserted on the beam line with no tilt angle, i.e. parallel to the machine axis (13:30-13:50);
- only left jaw inserted, with right jaw retracted by 2 σ with no tilt angle (14:20-14:40);
- only right jaw inserted, with left jaw retracted by 2 σ with no tilt angle (14:45-14:52);
- both jaws inserted on the beam line with a -211 μrad tilt angle as from BPM-based alignment (14:55-15:05).

In all cases, the collimator was set at a 7.3 σ aperture. This set of configurations allow to study the BLM response with different distributions of losses on the collimator jaw.
The analysis follows the same procedure described in 5.1.1. Depending on the duration of the excitations and on the loss rate, the final calibration factors are obtained as a single value after the end of the blow up or as a mean of the measurements during the whole excitation (see fig. 5.3). The results are reported in tab. 5.6. As it can be seen, the cases with no tilt show a larger contribution from one jaw over the other one; moreover, the case with both jaws in is in-between the other two, giving a hint of a somehow equally distributed contribution to the BLM signal from the two jaws. The configuration with only the left jaw inserted is the one that gives the highest result. The calibration factor with both jaws in and parallel to the closed orbit shows the lowest value, since the self-absorption by the collimator jaw is maximised.

Configuration	**Timestamps**	**Method**	**Calibration Factor [pGy/p]**	**% Error**
Both jaws in no tilt	14:36:30.0-13:42:30.0	mean	2.44	2.5
Only left jaw in no tilt	14:39:30	single value	2.63	10.0
Only right jaw in no tilt	14:47:20.0-14:50:00.0	mean	2.25	2.5
Both jaws in tilt from BPM	14:59:30	single value	1.96	10.0

Table 5.6: BLM calibration factors obtained from measurements for TCTPH.4R5.B2 at 450 GeV in different configurations.

5.2.2 Simulation settings

The simulation setup is very similar to those used earlier in this work. Most of the collimators were set at 50 mm aperture during the measurements, so they are not included in the SixTrack-FLUKA simulations. All the collimators left in during the measurements were taken into account with the deployed settings reported in tab. 5.8.
The simulations make use use of the 2016 injection optics. The optics functions read from the *twiss file* are reported in tab. 5.7. The configuration with both jaws inserted in the beam line was analysed with three different angles, since in measurements this is the only one where the tilt angle of the jaws was varied:

- with no tilt applied to the jaws. This configuration corresponds to having the jaws perfectly parallel to the machine axis;

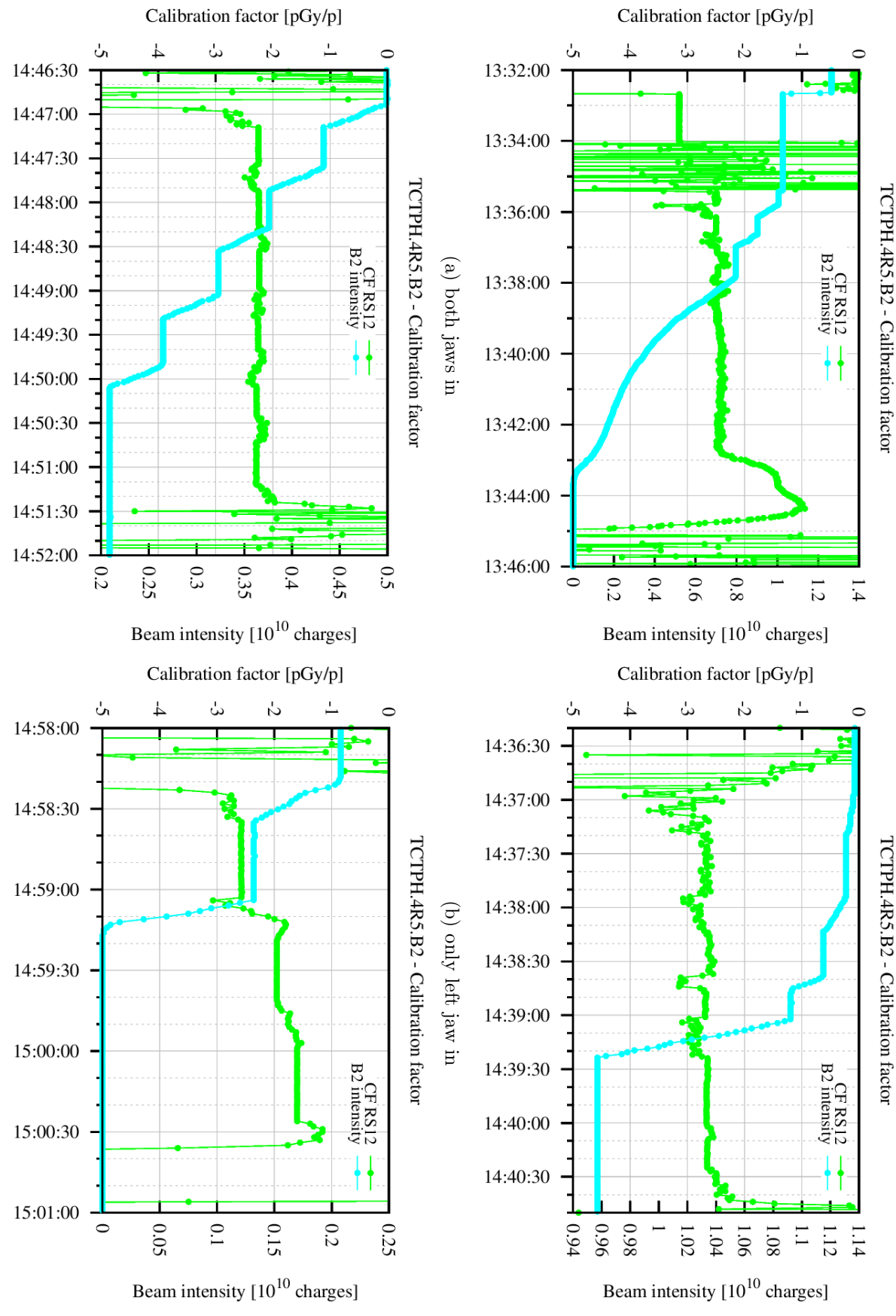

Figure 5.3: Calibration factor of the BLM at the TCTPH.4R5.B2 at 450 GeV as measured in different configurations. The BCT signal for Beam 2 is also shown.

	x **(cleaning plane)**	y **(non-cleaning plane)**
β **[m]**	159.451	78.725
α	0.747	-0.023
D **[m]**	0.016	-0.035
D'	$0.005 \cdot 10^{-3}$	$-0.030 \cdot 10^{-3}$
z_{CO} **[mm]**	2.439	0.350
z'_{CO} **[μrad]**	31	-17

Table 5.7: Values of the β function, dispersion D, offset of the closed orbit z and their derivatives at TCTPH.4R5.B2 for both planes as read from the *twiss file* for the 2016 injection optics.

Collimator	**Aperture [number of σ]**
TCTPH.4R5.B2	7.28
TCTPV.4R5.B2	32.87
TCP.D6R7.B2	5.69 (both jaws in) 6.27 (only one jaw in)
TCP.C6R7.B2	23.83
TDI.4R8	6.21
TCDQA.A4L6.B2	10.36
TCDQA.C4L6.B2	10.25
TCDQA.B4L6.B2	10.14
TCLIA.4L8	6.96
TCLIB.6L8.B2	7.18

Table 5.8: Collimator settings of the cleaning simulation at 450 GeV.

- with a 30 μrad applied to the jaws. This scenario corresponds to having the jaws parallel to the closed orbit (see tab. 5.7);
- with a 241 μrad applied to the jaws. This configuration corresponds to the actual jaw positioning with no tilt applied, as reconstructed from BPMs.

In fact, in 5.2.1 it is reported that the BPM-based alignment set the jaws parallel to the beam only when an angle of -211 μrad was deployed. This is due to an offset in the orientation of the collimator, as briefly explained in 5.1.2. The 0 μrad orientation displayed on the CCC monitoring software (first three measurements in tab. 5.6) does not correspond to the 0 μrad of the simulations. That is why the alignment to the closed orbit is achieved with a rotation of -211 μrad by the CCC monitoring software and 30 μrad in the simulation setup. Comparing these two angles it is possible to derive that the 0 μrad orientation shown by the CCC monitoring software actually corresponds to a 241 μrad rotation in the simulation, explaining the choice of the third setup. These three configurations have different loss patterns due to the different orientations, leading to a different BLM response.
The configurations with one jaw inserted in the beam line and the other jaw retracted were also simulated. In this situation only the beam halo on the side of the inserted jaw is sampled in order to optimise computation time. A 241 μrad tilt angle is applied in these

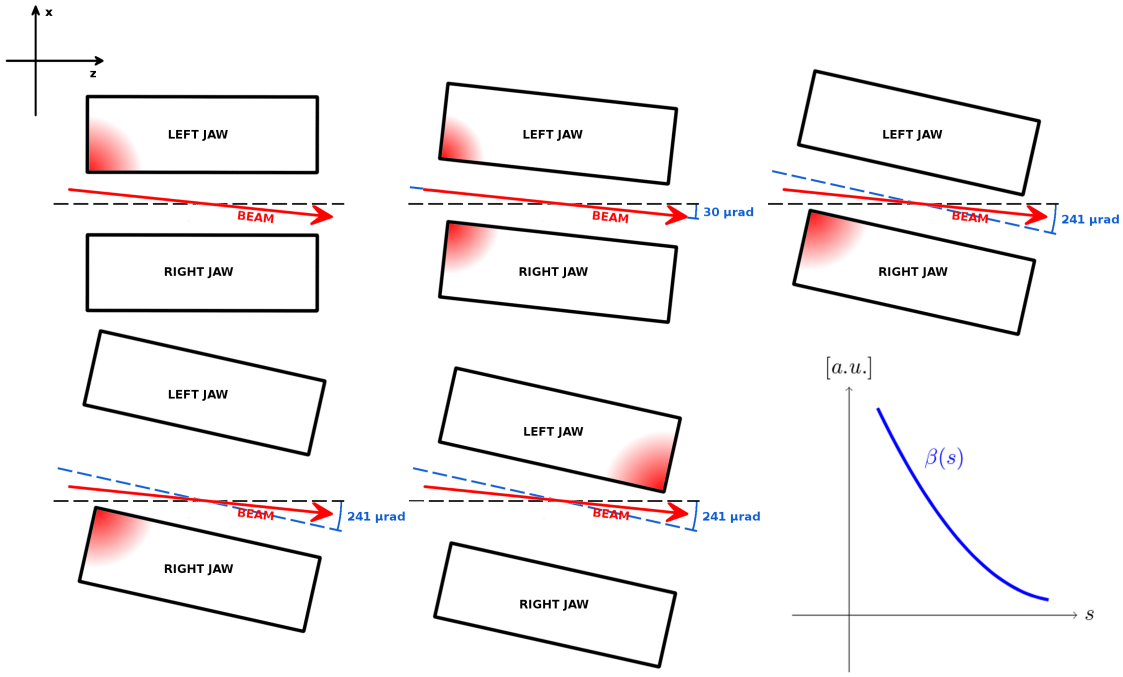

Figure 5.4: Schematic representation of the simulated configurations: with no tilt of the collimator jaws (top left frame), with a 30 μrad tilt (top middle frame), with a 241 μrad tilt (top right frame), with only the right jaw inserted (bottom left frame) and with only the left jaw inserted (bottom middle frame). The bottom right frame shows a sketch of the β function behaviour on the cleaning plane. The impacted corner for each configuration with a 0.01 σ wide beam sampling is highlighted in red. Note that the angle of the closed orbit is reversed in order to reconstruct the correct geometry for Beam 2 while keeping the Beam 1 reference system in FLUKA. With 0.25 σ both jaws are impacted.

configurations, since the measurements were done with 0 μrad shown by the CCC monitoring software. All the simulated configurations are shown in fig. 5.4.

The FLUKA simulation setup is the same as the one used in 5.1.2. The simulated BLM that best reproduces the one installed at the TCTPH.4R5.B2 is the one labelled as BLMU in a vertical position (see tab. 4.4). This BLM is located in the bottom row of the mesh, in the closest position with respect to both the pipe and the collimator (see fig. 4.6 and tab. 4.3). Different configurations are explored with simulations:

- both 0.01 and 0.25 σ sampling on the cleaning plane;
- both vertical and horizontal BLMs.

As discussed in chapter 4, simulations with 0.01 σ sampling represent a conservative simulation setup, whereas the setup with a larger sampling interval on the cleaning plane should better reproduce what actually happens in the machine. The BLMs have been simulated with both orientation to potentially extend the analysis to other collimators. In addition to that, a set of simulations was run with the map of the touches loaded with a rotation of 180° around the longitudinal axis of the collimator. This was the strategy implemented to take into account the different local reference system of Beam 1 and Beam 2 at the collimators without re-building the entire FLUKA geometry, taking advantage from the fact that the simulated scenario is symmetric on the vertical plane, i.e. the one of non-cleaning. In fact,

in the tracking simulations, the reference system has the longitudinal coordinate oriented parallel to the direction of the beam, i.e. clockwise for Beam 1 and anti-clockwise for Beam 2. In order to keep the y axis vertical and a right-handed system, the x axis points outwards of the ring for Beam 1 and inwards of the ring for Beam 2. Since the BLMs at the TCTs are always on the outside of the ring, the rotation of the map of touches was necessary. The results of this last simulation will be the ones to compare with the measurements, but the other simulations are still useful for sensitivity analyses.

5.2.3 Results

The simulated BLM signal for all the different setups with both jaws inserted on the beam line are reported in tab. 5.9. As it can be seen, the BLMs at beam height are in general in a more favourable position, leading to higher calibration factors; moreover, BLMs closer to the beam pipe (i.e. positions 1 and 2) show higher calibration factors than the others. The most favourable position of all is 2, i.e. the farthest from the collimator along the longitudinal axis. Signals coming from the top and bottom rows are extremely similar; this symmetry is consistent with the simulated scenario, i.e. losses on the cleaning plane of a horizontal collimator, with almost no asymmetries on the vertical plane. Regarding the orientation, vertical BLMs have slightly higher response functions than the horizontal ones, making them the most suitable for monitoring purposes. Finally, the beam sampling affects the calibration factor as well, with a 0.25 σ wide halo implying a higher BLM response than 0.01 σ. The simulated signal response of BLMU, which is the closest to the real position of the BLM installed at the TCTPH.4R5.B2, is higher than the measured one for the configuration with a 30 μrad tilt, while the simulation underestimates the calibration factor for the configuration with a 241 μrad tilt. However, the two values agree within 20-30%.
The simulations with only one jaw in view of the beam have been carried out in the same way, but introducing only the tilt by 241 μrad. The results are reported in tab. 5.10. The same remarks as for the previous table apply, with simulated signals from the bottom and top rows being extremely close and the one from the middle row being the highest, while vertical oriented BLMs give higher signals than horizontal oriented ones. The behaviour of the calibration factor with respect to which jaws are inserted is correctly reproduced, with the configuration with impacts on both jaws having a response that is in-between the cases with only the left jaw (i.e. the highest) and only the right jaw. Once again, all results agree with measurements within 20-30%.
Tab. 5.11 and 5.12 show the ratio between the simulated BLM response and the simulated peak energy deposition in the impacted jaw. Configurations with 0.25 σ interval shows noticeably higher value, as they correspond to higher BLM response and lower energy peak, since the impact distribution is less concentrated. The highest values for each configuration correspond to BLMs belonging to the middle row, which have the highest response. This confirms that, as observed in sec. 5.1, the most favourable position for a BLM is the one labelled in fig. 4.6 as 2.

	Horizontal BLMs	Vertical BLMs		
	0.01 σ	**0.01 σ**	**0.25 σ**	**0.25 σ reversed**
0 μrad	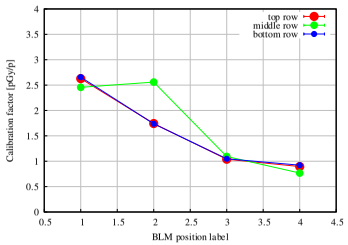	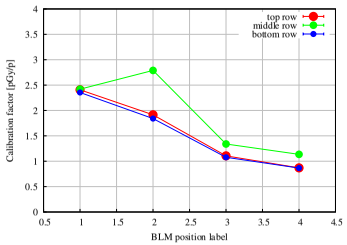	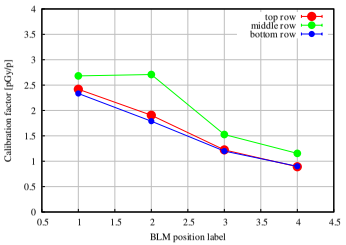	
30 μrad	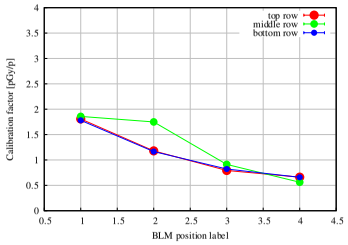	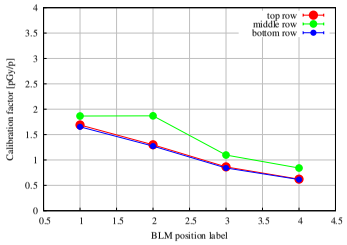	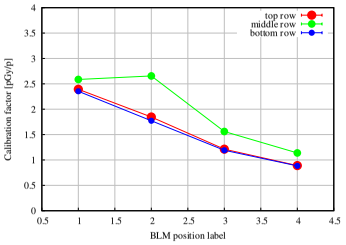	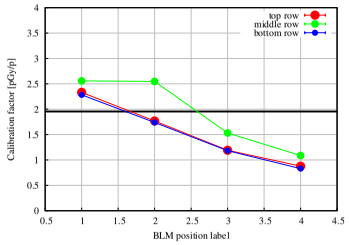
241 μrad	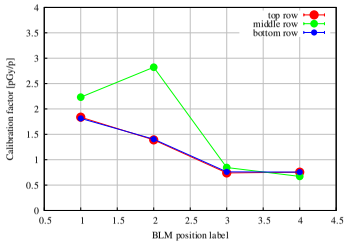	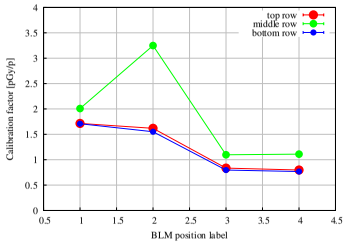	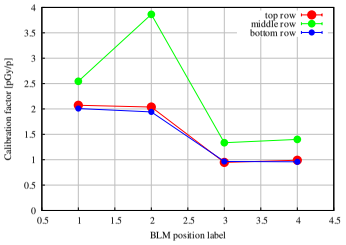	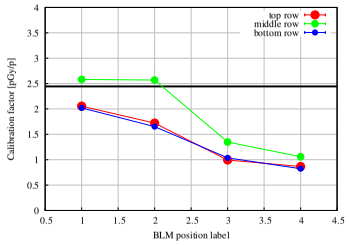

Table 5.9: Simulated signals for the three layers of the BLM mesh set up for the TCTPH.4R5.B2 at 450 GeV. The various configurations in terms of orientation of the BLMs, sampling interval and tilt applied to the jaws are reported. The last column reports the simulation where the map of touches is rotated by 180° around the longitudinal axis to reflect the actual Beam 2 geometry. The black line in these plots represents the measured value. BLMU is the bottom row BLM with label 1.

	Horizontal BLMs	Vertical BLMs		
	0.01 σ	**0.01 σ**	**0.25 σ**	**0.25 σ reversed**
241 μrad	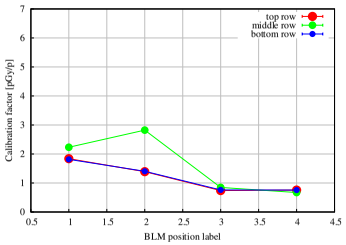	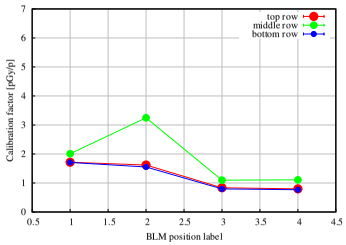	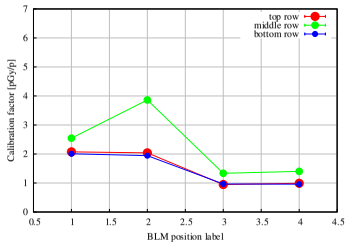	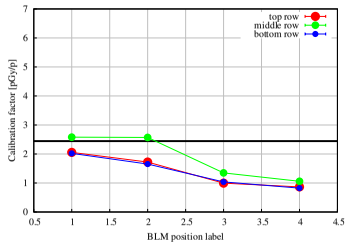
241 μrad left jaw in	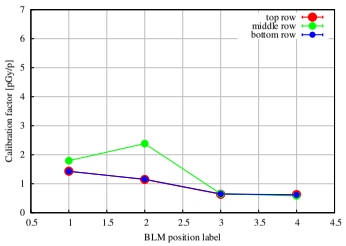	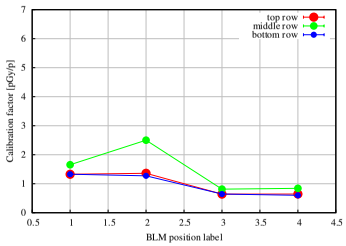	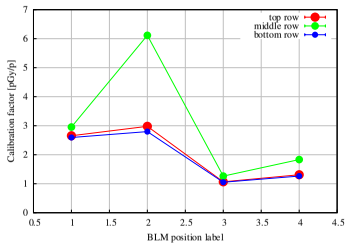	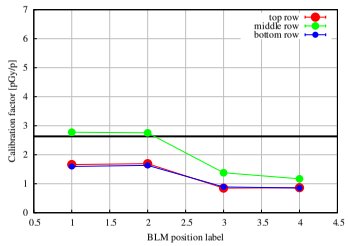
241 μrad right jaw in	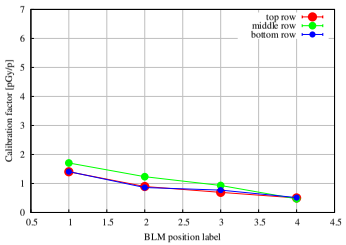	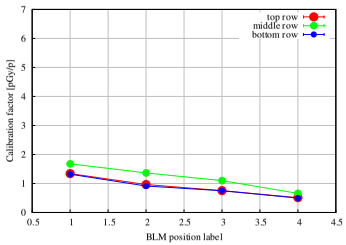	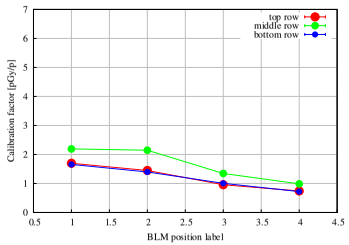	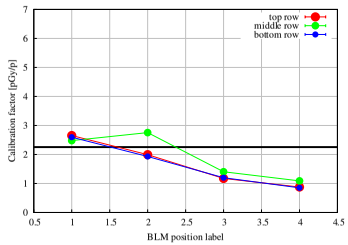

Table 5.10: Simulated signals for the three layers of the BLM mesh set up for the TCTPH.4R5.B2 at 450 GeV. The various configurations in terms of orientation of the BLMs, inserted jaws and tilt applied to the jaws are reported. The last column reports the simulation where the map of touches is rotated by 180° around the longitudinal axis to reflect the actual Beam 2 geometry. The black line in these plots represents the measured value. BLMU is the bottom row BLM with label 1.

	Horizontal BLMs	Vertical BLMs		
	0.01 σ	**0.01 σ**	**0.25 σ**	**0.25 σ reversed**
0 μrad	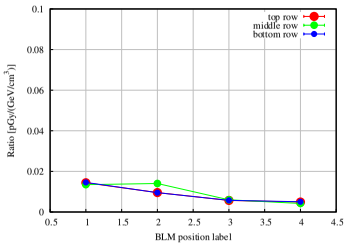	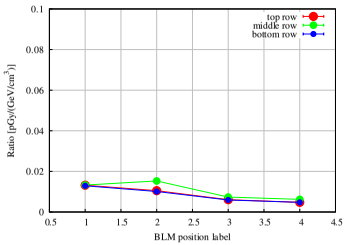	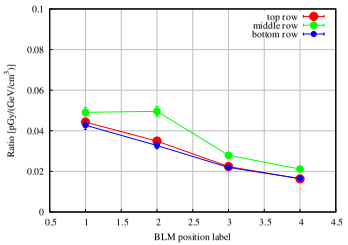	
30 μrad	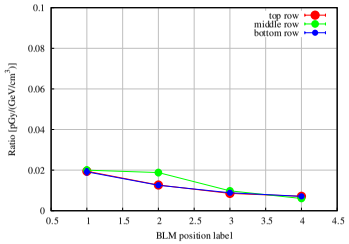	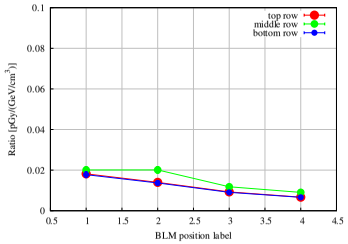	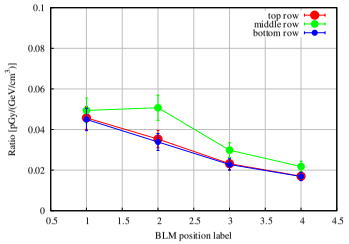	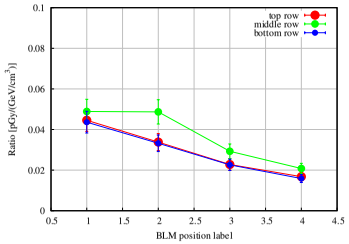
241 μrad	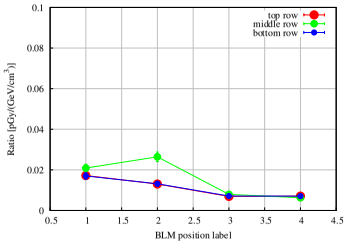	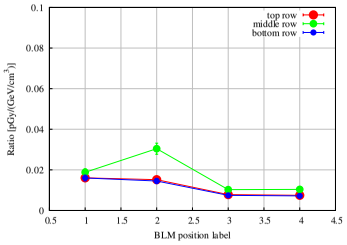	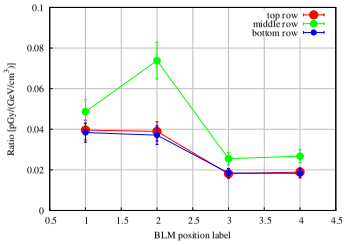	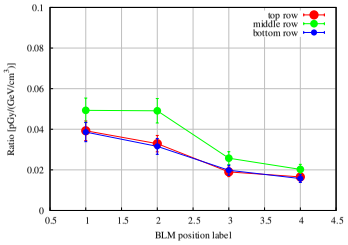

Table 5.11: Ratio between the simulated BLM response and the simulated peak energy deposition for the three layers of the BLM mesh set up for the TCTPH.4R5.B2 at 450 GeV. The various configurations in terms of orientation of the BLMs, sampling interval and tilt applied to the jaws are reported. The last column reports the simulation where the map of touches is rotated by 180° around the longitudinal axis to reflect the actual Beam 2 geometry. BLMU is the bottom row BLM with label 1.

	Horizontal BLMs	Vertical BLMs		
	0.01 σ	**0.01 σ**	**0.25 σ**	**0.25 σ reversed**
241 μrad	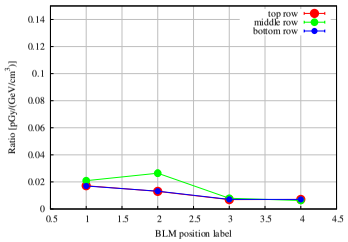	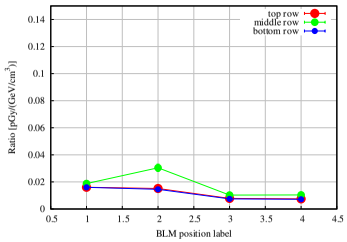	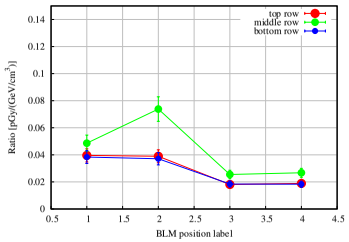	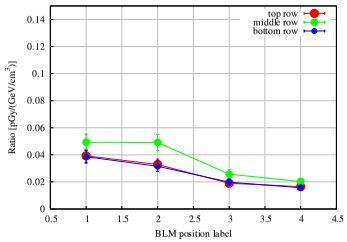
241 μrad left jaw in	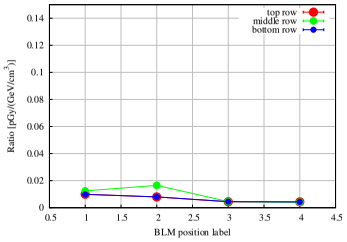	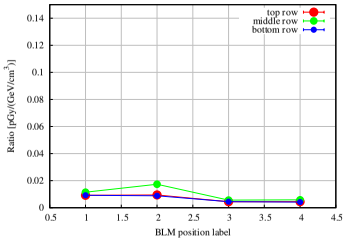	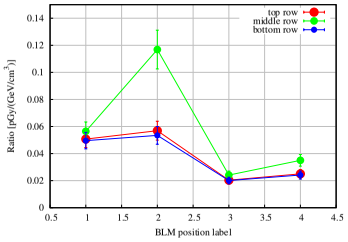	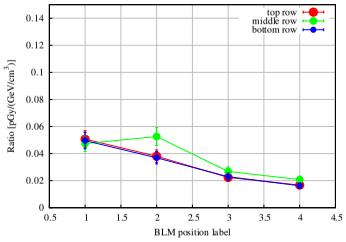
241 μrad right jaw in	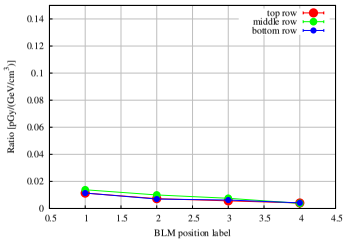	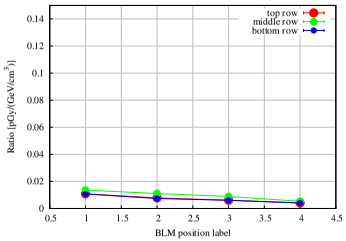	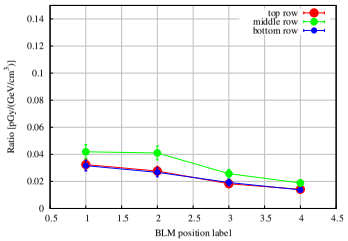	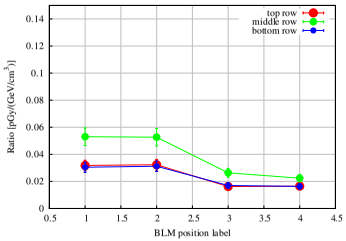

Table 5.12: Ratio between the simulated BLM response and the simulated peak energy deposition for the three layers of the BLM mesh set up for the TCTPH.4R5.B2 at 450 GeV. The various configurations in terms of orientation of the BLMs, inserted jaws and tilt applied to the jaws are reported. The last column reports the simulation where the map of touches is rotated by 180° around the longitudinal axis to reflect the actual Beam 2 geometry. BLMU is the bottom row BLM with label 1.

Chapter 6

BLM thresholds proposal

Chapter 4 concluded that the maximum energy deposition per unit volume allowed by the current BLM thresholds for the considered scenario is not worrying for short time-scales, hence running sums up to RS09, whereas it reaches a range where plastic deformation of the jaw can take place for longer time-scales, i.e. RS10 and longer. The energy deposition has been calculated adiabatically, i.e. assuming that energy transfer mechanisms inside the jaw material can be neglected. Together with chapter 4, the benchmark of the simulation tools reported in chapter 5 also showed how the BLM response is strongly dependent on the relative position and orientation of the BLMs with respect to the corresponding collimator, leading to the identification of an ideal position that maximises the BLM response. The following sections combine these results to propose new BLM thresholds at the TCTs.

6.1 Calculation of the new BLM thresholds

While all the TCTs in all interaction points have the same role and design, even though they are operated with different settings, operational corrections cumulated over the years and resulted in a proliferation of families - presently, a total of four. Since all the TCTs have the same structure and role, in principle they could also be exposed to the same loss scenario and damage; therefore, it should be possible to set the same BLM thresholds for all the TCTs and hence have only one family. Key to the unification of TCT families is to assure that all the BLMs at the TCTs have the same response. Consequently, the first step towards the homogenisation of the BLM thresholds would be moving all the BLMs at the TCTs in the same relative position. The most suitable position as identified thanks to this work is the one in position 2 in the middle row vertically oriented (see fig. 4.6 and tab. 4.3), since it has the highest response for the largest fraction of simulated scenarios, maximising sensitivity to losses. Beam energy would then be the only variable when calculating new BLM thresholds.
The BLM thresholds are computed in order to trigger a beam dump once a certain regime of energy/power deposition is reached. For a given loss scenario, the energy/power deposition and the BLM signal scale linearly with the number/rate of impacting protons respectively, as discussed in sec. 4.4. The simulations performed in this work allowed to correlate the energy deposition on the collimator jaw to the BLM signal per impacting proton for the same scenario. Hence, the maximum number/rate of protons impacting the jaws allowed by the BLM thresholds presently deployed were reconstructed, checking that the induced levels of energy/power deposition could be used as limits. The results are reported in tab. 6.1 for each beam energy value. Having identified the BLM with the largest response by exploring the dependence of the BLM signal on orientation and relative position with respect to the

collimator, it is then possible to propose a unique set of new thresholds for all TCT BLMs. The new thresholds are set based on the number/rate of protons allowed by the present thresholds at 7 TeV, and the dependence of peak energy deposition and BLM response on beam energy as from the simulations. The point at 7 TeV is chosen since it maximises the energy deposition per impacting proton (see fig. 4.8).

Beam energy [TeV]	**Maximum allowed number of protons**	**Maximum allowed proton rate [p/s]**
0.45	$2.863{\cdot}10^{10}$	$1.058{\cdot}10^{10}$
3.5	$2.131{\cdot}10^{9}$	$1.240{\cdot}10^{9}$
5	$8.972{\cdot}10^{8}$	$5.224{\cdot}10^{8}$
6.5	$3.793{\cdot}10^{8}$	$3.126{\cdot}10^{9}$
7	$2.059{\cdot}10^{8}$	$1.055{\cdot}10^{9}$

Table 6.1: Maximum number and rate of impacting protons allowed by the current BLM thresholds for each beam energy value.

For running sums up to RS09, BLM thresholds can be derived by the maximum allowed number of protons impacting the jaws. In fact, for short time-scales, the thermo-mechanical response is driven only by the amount of energy deposited (see sec. 4.4). Given the fact that values of peak energy deposition are not worrying for the considered scenario (i.e. moving jaw or closed orbit), the maximum number of impacting protons allowed by the current BLM thresholds can be considered. This number scales with beam energy, as shown in fig. 4.16; as previously stated, the value of $N_{p,max}$ at 7 TeV is chosen to re-set the BLM thresholds at flat top. The values for the other energies are obtained by scaling with the peak energy deposition:

$$N_{p,max}|_{E_b} = \frac{E_{peak}|_{7\text{TeV}} \cdot N_{p,max}|_{7\text{TeV}}}{E_{peak}|_{E_b}} \equiv \frac{K_N}{E_{peak}|_{E_b}} \tag{6.1}$$

The thresholds in Gy/s are calculated via the following formula:

$$D_{\text{BLM}} = \frac{\text{CF}|_{E_b} \cdot N_{p,max}|_{E_b}}{\Delta T_{\text{RS}}} = \frac{\text{CF}|_{E_b}}{E_{peak}|_{E_b}} \cdot \frac{K_N}{\Delta T_{\text{RS}}} \tag{6.2}$$

where ΔT_{RS} is the time window of the considered running sum.
In principle, similar arguments can be made for longer running sums (i.e. from RS10 onwards) considering the proton loss rate instead:

$$R_{p,max}|_{E_b} = \frac{E_{peak}|_{7\text{TeV}} \cdot R_{p,max}|_{7\text{TeV}}}{E_{peak}|_{E_b}} \equiv \frac{K_R}{E_{peak}|_{E_b}} \tag{6.3}$$

In this case the thresholds are calculated via the following equation:

$$D_{\text{BLM}} = \text{CF}|_{E_b} \cdot N_{p,max}|_{E_b} = \frac{\text{CF}|_{E_b}}{E_{peak}|_{E_b}} \cdot K_R \tag{6.4}$$

Contrary to what happens for short time-scales, the maximum power loss values allowed by the present BLM thresholds for the considered scenario as found in chapter 4 could potentially bring the jaw material close to the plastic deformation regime and therefore have

to be handled more carefully. Hence, as it will be shown later, the option of introducing a safety margin can be considered.
The above equations show that the BLM thresholds scale by the ratio between the calibration factor and the peak energy deposition at the considered beam energy. Both the simulated calibration factor and the simulated peak energy deposition show a fairly linear dependence on beam energy. A linear fit, shown in fig. 6.1, is applied to both in order to calculate the ratio at any energy level of the BLM thresholds, including those that were not simulated. Fig. 6.2 shows the ratio between the two fitting functions. The value at 450 GeV is the one that stands out the most, due to the significantly wider spread of the beam shown in fig. 4.7 that reduces the peak energy deposition with respect to the other energies.

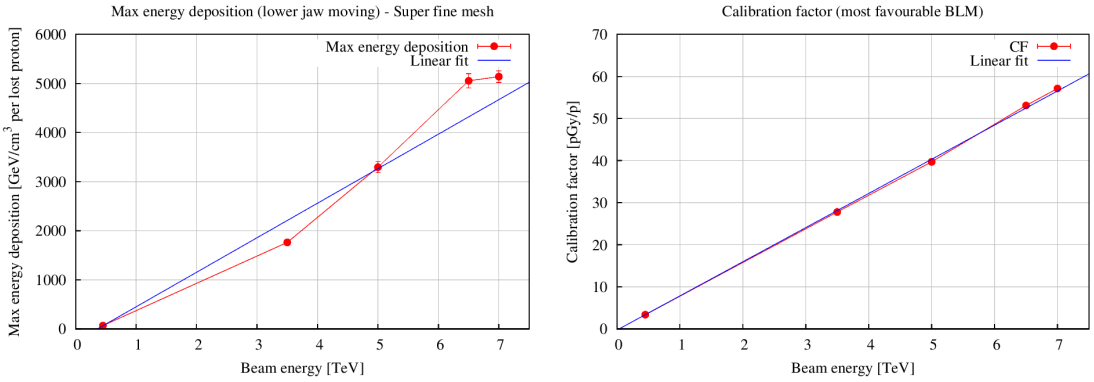

Figure 6.1: Linear fit through the simulated peak energy deposition (left frame) and the simulated BLM calibration factor for the most favourable configuration (right frame), both as function of beam energy.

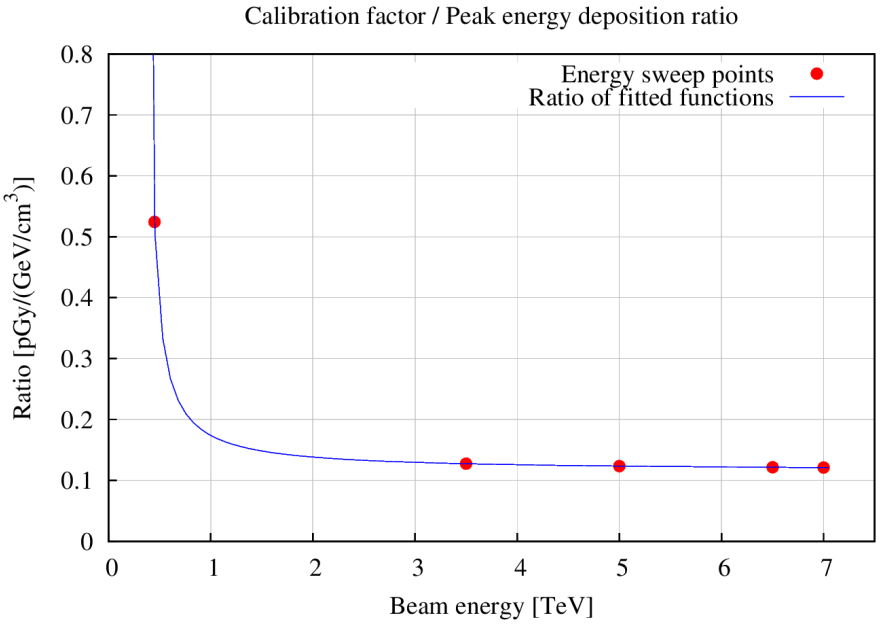

Figure 6.2: Ratio between the simulated BLM response and the simulated peak energy deposition as calculated with the fitting curves in fig. 6.1 as function of beam energy.

6.2 Proposal

Two sets of thresholds are proposed, differing on the limits for long running sums. In particular, one set is more aggressive and sets thresholds at the power loss allowed by the present BLM thresholds, which has been found to bring the jaw close to the plastic deformation regime, while the other set is more conservative. A safety factor 2 has been introduced in both options, in order to take into account the different response function that the same BLM has to losses on horizontal or vertical jaws. This can be derived by a comparison of the results obtained in chapter 5 using horizontal collimators in similar conditions to the one simulated in chapter 4 (i.e. at 450 GeV and 6.5 TeV with only one jaw inserted and protons impacting on the end of the collimator jaw), showing that BLMs at horizontal collimators have a lower calibration factor than the ones at vertical collimators.
The first set of BLM thresholds is calculated using directly the equations presented in sec. 6.1. Since the value obtained with eq. 6.2 for RS09 is actually lower than the one obtained with eq. 6.4 for RS10, the calculation based on the proton loss rate has been extended to RS09 since longer running sums would never be triggered otherwise. The results are shown in the left frame of fig. 6.3.
The other proposal is more cautious. Eq. 6.2 is used to calculate the thresholds up to RS09 and then the value corresponding to RS09 is kept constant up to RS12. This approach leads to lower thresholds for longer running sums, in order keep the power loss lower than the limit situation described above. The results are shown in the right frame of fig. 6.3.

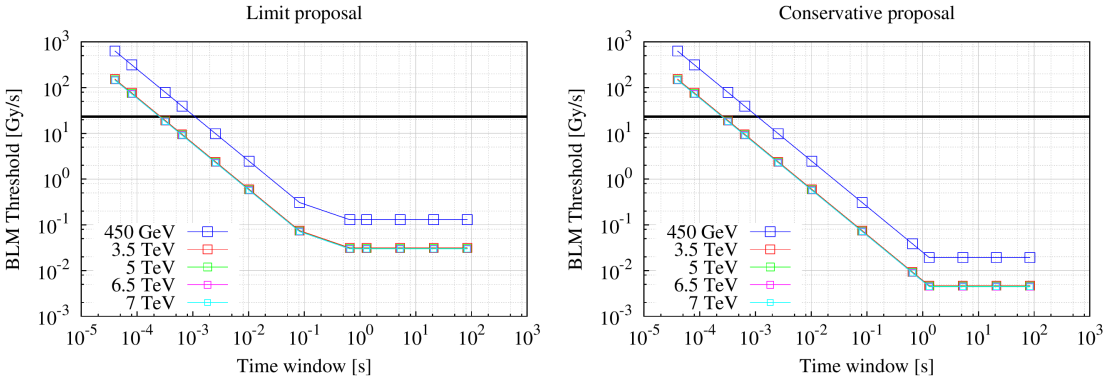

Figure 6.3: Proposed BLM thresholds using the calculated power loss for running sums from RS09 up to RS12 (left frame) and using the more conservative approach of extending the RS09 value up to RS12 (right frame). The black line corresponds to the 23.16 Gy/s limit value due to saturation of the electronics.

The black line in fig. 6.3 represents the 23.16 Gy/ps limit value due to saturation of the electronics; no threshold is allowed above this value, so all thresholds that are calculated to be higher than that must be lowered to 23.16 Gy/s. Fig. 6.4 shows the number and rate of impacting protons allowed by the two proposed sets of BLM thresholds. The scaling of the proposed BLM thresholds with beam energy reflects the behaviour of the ration between the calibration factor and the peak energy deposition shown in fig. 6.1.
While being self-consistent, the present proposal should be verified against other loss scenarios, e.g. leakage from IR7 to the TCTs in case of low beam lifetimes or spurious signals from collision debris. These verifications are done every year, during the very first stages of data taking, to align the BLM thresholds to the operational configuration of the machine. Hence, they are beyond the scope of this work.

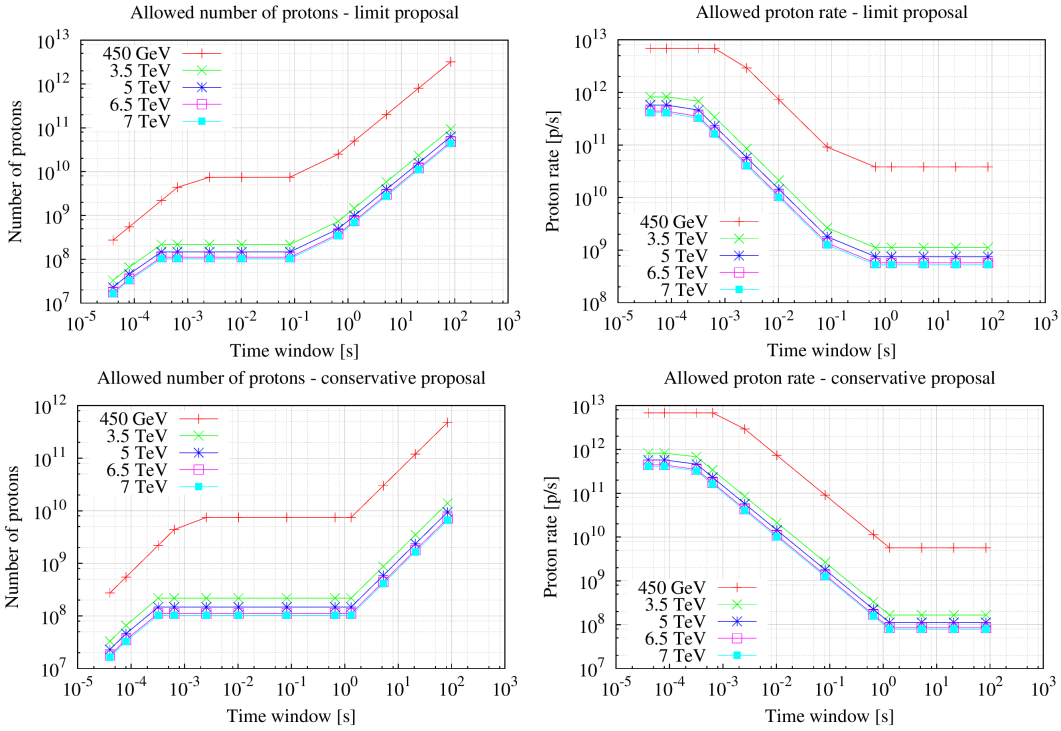

Figure 6.4: Number and rate of impacting protons allowed by the proposed BLM thresholds for the limit (top row) and conservative (bottom row) proposal.

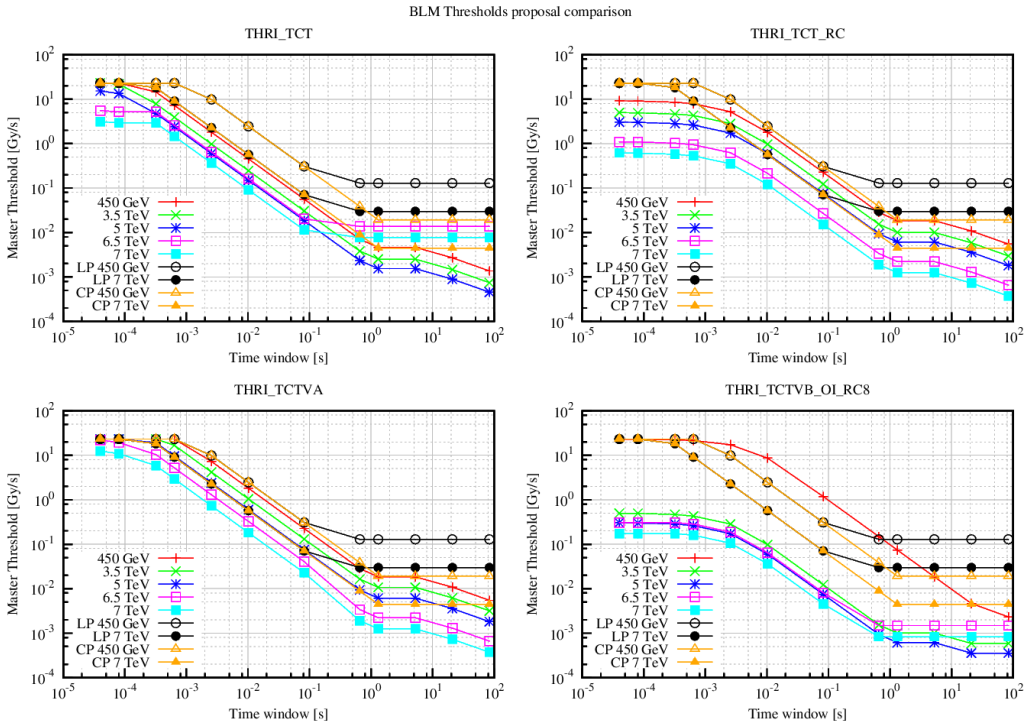

Figure 6.5: Comparison between the proposed BLM thresholds and the current master thresholds, both for the limit proposal (LP) and conservative proposal (CP). Only the proposed thresholds at 450 GeV and 7 TeV are shown, as the other beam energies have nearly identical values to 7 TeV.

Fig. 6.5 compares the proposed set of BLM thresholds with the presently deployed master thresholds. Even though the relative positions between collimators and BLMs are not the same, the new thresholds are in general not too far away from the present ones, and they allow to have a more precise and uniform response to the same energy deposition.

Chapter 7

Conclusions and outlook

The aim of this work is to review and propose further optimisation of the current thresholds of the BLMs at the TCTs, as part of a more extended review of the thresholds at all collimators. TCTs were chosen as the starting point for this review since their jaws are made of tungsten (i.e. the least robust material among those used for the jaws) and their locations offer a rather simple picture, minimising the cross-talk from losses on nearby collimators. In particular, the review of BLMs at the TCTs has become important since BLM thresholds for this family of collimators were never studied in detailed, and a simplified approach was taken to set the thresholds at the LHC start-up; moreover, several adjustments were applied during the years of operation to accommodate operational needs, moving the thresholds away from their original values. Furthermore, TCT families have been reorganised in the past and need some homogenisation.

The review of the BLM thresholds at the TCTs is based on numerical simulations. The scenario of a jaw moving towards the beam has been considered; this can be used also for the similar case of the beam closed orbit drifting towards the jaw (without taking into account the causes of the orbit distortion and the consequences on the closed orbit elsewhere). Therefore, the considered scenario is of direct beam impact, with the collimator resulting as the primary bottleneck of the machine (instead of IR7). Simulations have been carried out in two steps: cleaning simulations, to obtain the impact distribution at the collimator, and energy deposition simulations, to simulate the interaction with the jaw and the BLM signal. The second step allows to have with one simulation at the same time both the energy deposition in the jaw and the BLM signal. The dependence of the BLM response and of the energy deposition on beam energy has been explored by performing simulations at selected energy values.

An extensive benchmark has been conducted, both qualitatively by comparison with the energy dependence of the BLM response at the TCPs measured in 2017, and quantitatively, by reconstructing the BLM response of the horizontal TCTs in IR5 measured in 2016. The simulations also allowed to study the behaviour of the BLM response with respect to the BLM orientation and relative position between BLM and collimator. This lead to the identification of the configuration that maximises the BLM response. Moreover, the sensitivity to the thickness of the sampled halo distribution has been explored, confirming that more spread distributions lead to more relaxed scenarios, due to lower peak energy deposition values and higher BLM signals.

The results of the simulations have been used to calculate the maximum energy deposition and power loss allowed by the current BLM thresholds. While values for short running sums have been found not to be worrying in terms of temperature variation, power loss for long running sums may bring the jaw close to plastic deformation regime, requiring detailed

thermo-mechanical studies (beyond the scope of this work) to reach a conclusive statement. These values have been used to propose new sets of BLM thresholds, unifying the TCT families by assuming the BLMs to be in the same relative position for all the collimators, i.e. the one that maximises the BLM response.
The proposed thresholds, while being derived in a consistent way, need to be cross-checked against other aspects related to machine operation that have not been taken into account during this work (e.g. the spurious signals due to collision debris coming from the IP and hitting the TCTs).
This work is only the starting point for the more extensive review of the BLM thresholds at collimators. The focus should be moved on to different collimator families. For example, TCL6 has jaws made of tungsten like the TCTs, but the β function on the cleaning plane is smaller; this means that a movement of the jaw may lead to a significant change in the cut performed by the collimator on the beam. From the present study, this scenario is not expected to be worrying; nevertheless, cross-checks via simulations should be done. Furthermore, TCL4 and TCL5 have jaws made of copper, requiring a detailed study of the dependence of the BLM response on the jaw material. Finally, the BLM thresholds review should be also extended to collimators with jaws in graphite. These are mainly concentrated in IR7 and IR3, and a large cross-talk is found.

Bibliography

[1] O. S. Brüning et al. *LHC Design Report*. CERN, 2004.

[2] M. Sapinski et al. Initial settings of Beam Loss Monitors thresholds on LHC collimators. Internal CERN publication, 2008.

[3] BLM thresholds modifications EMDS documents. `https://edms.cern.ch/ui/#!master/navigator/project?P:1167856483:1167856483:subDocs`.

[4] E. Skordis. Simulation comparisons to BLM data. Technical report, Tracking for Collimation Workshop, 2015.

[5] S. Redaelli. Beam Cleaning and Collimation Systems. In *CERN Yellow Report*, volume 2, 2016.

[6] G. Valentino et al. A systematic measurement analyzer for LHC operational data. In *Proceedings of ICALEPCS2015*, 2015.

[7] M. N. Wilson. *Superconducting Magnets*. Oxford University Press, 1987.

[8] C. Bracco. *Commissioning Scenarios and Tests for the LHC Collimation System*. PhD thesis, EPFL Lausanne, 2008.

[9] B. Dehning et al. The LHC beam loss measurement system. In *Proceedings of PAC07*, 2007.

[10] BLM integration time windows. `https://ab-div-bdi-bl-blm.web.cern.ch/ab-div-bdi-bl-blm/Acquisition_system/Data_acquisition_integration_durations_20100313.htm`.

[11] E. B. Holzer et al. Commissioning and optimization of the LHC BLM system. In *Proceedings of HB2010*, 2010.

[12] E. Nebot et al. Handling of BLM abort thresholds in the LHC. In *Proceedings of IPAC2011*, 2011.

[13] S. Redaelli et al. Collimator BLM thresholds strategy. In *Workshop on Beam-Induced Quenches*, 2014.

[14] F. Cerutti et al. Collimator load and BLM response. In *LHC Collimation Working Group #179*, 2014.

[15] E. Skordis. Status of FLUKA Simulations for Collimation BLM Thresholds. In *BLM Thresholds Working Group Meeting #6*, 2015.

[16] E. Skordis. TCT BLM response from tertiary halo at 6.5 TeV. In *LHC Collimation Working Group #206*, 2016.

[17] K. Wille. *The physics of particle accelerators: an introduction*. Oxford University Press, 2000.

[18] D. A. Edwards and M. J. Syphers. *An introduction to the physics of high-energy accelerators*. Wiley, 1993.

[19] J. Beringer et al. Review of Particle Physics. In *Phys. Rev. D*, 2012.

[20] K. S. Krane. *Introductory Nuclear Physics*. J. Wiley and Sons, 1987.

[21] A. Ferrari and P. R. Sala. The Physics of High Energy Reactions. Technical report, CERN, 1997.

[22] V. Previtali. *Performance evaluation of a crystal-enhanced collimation system for the LHC*. PhD thesis, EPFL Lausanne, 2010.

[23] S. Redaelli. Beam cleaning and collimation system. Technical report, CERN Beams Department, 2014.

[24] Recommendation from the external review panel of the 2013 collimation review. `https://indico.cern.ch/event/251588/material/2/0`.

[25] R. Assman et al. The final collimation system for the LHC. Technical report, CERN, 2006.

[26] The official FLUKA site. `http://www.fluka.org/fluka.php`.

[27] G. Battistoni et al. Overview of the FLUKA code. In *Annals of Nuclear Energy 82*, 2015.

[28] SixTrack website. `http://sixtrack.web.cern.ch/SixTrack/`.

[29] F. Schmidt. SixTrack version 4.2.16 single particle tracking code treating transverse motion with synchrotron oscillations in a symplectic manner. Technical report, CERN, 2012.

[30] G. Ripken and F. Schmidt. A symplectic six-dimensional thin-lens formalism for tracking. Technical report, CERN, 1995.

[31] R. De Maria et al. Recent developments and future plans for SixTrack. In *Proceedings of IPAC2013*, 2013.

[32] A. Mereghetti et al. The FLUKA linebuilder and element database: tools for building complex models of accelerator beam lines. In *Proceedings of IPAC2012*, 2012.

[33] V. Vlachoudis. FLAIR: a powerful but user friendly graphical interface for FLUKA. In *Proceedings of the International Conference on Mathematics, Computational Methods & Reactor Physics*, 2009.

[34] MADX website. `http://mad.web.cern.ch/mad/`.

[35] P. G. Ortega and A. Mereghetti. *FLUKA-SixTrack Coupling: Hands-on Guide*, 2017.

[36] Coupling SVN Repositories. `https://twiki.cern.ch/twiki/bin/view/FlukaTeam/CouplingSVNRepositories`.

[37] G. Valentino. Private communication with BE-ABP-HSS section at CERN.

[38] A. Lechner and C. Bahamonde Castro. Private communication with EN-STI-FDA section at CERN.

[39] C. Bahamonde. BLM threshold assessment with FLUKA. In *BLM Thresholds Working Group meeting*, 2017.

[40] B. Auchmann et al. Testing beam-induced quench levels of LHC superconducting magnets. In *Physical Review Special Topics - Accelerators and Beams*, volume 18, 2015.

[41] V. Boccone et al. Beam-machine Interaction at the CERN LHC. In *Nuclear Data Sheets*, volume 120, 2014.

[42] LHC BLM threshold modification reports. `https://ab-div-bdi-bl-blm.web.cern.ch/ab-div-bdi-bl-blm/Acquisition_system/Energy_Conversion.htm`.

[43] NIST website, Heat Capacity of Reference Materials: Cu and W. `https://srd.nist.gov/JPCRD/jpcrd263.pdf`.

[44] F. Carra. Private communication with EN-MME-EDS section at CERN.

[45] LHC OP eLogbook, 10-06-2016. `https://ab-dep-op-elogbook.web.cern.ch/ab-dep-op-elogbook/elogbook/secure/eLogbook.php?shiftId=1075821`.

[46] E. B. Holzer. Private communication with BE-BI-BL section at CERN.

[47] D. Mirarchi. *Crystal collimation for LHC*. PhD thesis, Imperial College, London, 2015.

[48] LHC OP eLogbook, 29-11-2016. `https://ab-dep-op-elogbook.web.cern.ch/ab-dep-op-elogbook/elogbook/secure/eLogbook.php?lgbk=60&date=20161129&shift=1`.